Quantitative Characterization of Fracture Surfaces of Engineering Materials with Scanning Electron Microscopy

Seyed Mahmoud Bayazid

Department of Mining and Materials Engineering
McGill University, Montreal
January 2023



A thesis submitted to McGill University in partial fulfillment of the requirements of the degree of Doctor of Philosophy

> © Mahmoud Bayazid 2023 All rights reserved.

Abstract

Quantitative microanalysis of rough surfaces is a big challenge in electron microscopy field. Although X-Ray microanalysis can be a useful tool for preliminary characterization, it is not quantitative because the geometry of rough surfaces introduces problems that are not present in the microanalysis of a bulk sample. The problem with the quantitative microanalysis of rough surfaces is that electrons can be scattered from all sides due to different slopes on the surface. Therefore, the geometry of rough surfaces impacts the generated, emitted, or measured x-ray intensities and thereby the quantitative analysis of the surface.

The present Ph.D. study will focus on fabricating 3D reconstruction technique for fracture surfaces and producing a quantitative method to characterize the non-flat surfaces with electron microscopy.

At first, a set of experiments, imaging, and modeling techniques were designed to get the 3D digital images of fracture surfaces. Using the backscattered signals, a 3D digital reconstruction was obtained. The effects of Scanning Electron Microscopy (SEM) parameters on the accuracy of the 3D reconstruction model which are taken via Backscattered Electron (BSE) images were studied. The results showed the best range of the working distance for our system is 9 to 10 mm. It was shown that by increasing the magnification to 1000X, the 3D digital reconstruction results improved. However, there was no significant improvement by increasing the magnification beyond 1000X. In addition, results demonstrated that the lower the accelerating voltage, the higher precision of the 3D reconstruction technique, as long as there are clean backscattered signals.

Moreover, the behavior of the Peak to Background (P/B) as one of the quantitative candidate methods for characterization of rough surfaces was analyzed while the take-off angle, tilt angle, particle size, and beam energy were altered. It was observed that P/B highly depends on the beam energy, particle size, and the composition of the substrates. Results indicated that the P/B increases at high tilt angles. Results showed that by increasing the take-off angle, the P/B initially reduces and then reaches a plateau. Data showed that the P/B increases when the electron beam is moved from the center to the side of a particle. Additionally, the P/B is mover sensitive to the beam movement for the spherical particles than the cubical particles.

In the next step, a geometrical correction factor (G) was introduced for the quantitative characterization of particles. Using the new ZAFG method (Z, atomic correction, A, absorption correction, F, florescence correction, and G, geometrical correction) makes it possible to quantify particles without using Monte Carlo simulation. Adding a geometrical factor to the convention ZAF method creates a very easy and simple way to quantify particles. Analyses showed that the G factor is a function of $\frac{D}{X_e}$, (where D is the diameter of particles, and X_e is the depth of emitted x-rays in a bulk sample with the same chemical composition). It was shown that when X_e becomes greater than D, the G factor decomposes exponentially as the incident electron energy rises. Data showed that when $\frac{D}{X_e} > 1$ for a particle, then G = 1. In this situation, the particle works almost as a bulk sample. It was shown that the G factor only depends on $\frac{D}{X_e}$, neither the chemical composition nor the beam energy.

Finally, in this work, preliminary results were presented using a real fracture surface. The existing Monte Carlo software (MC X-ray) was incorporated into the image processing software Dragonfly developed by Object Research Systems (ORS) Inc. The incorporation of the MC X-ray in Dragonfly allows users to do Monte Carlo simulation for any complicated geometry. An excellent agreement was observed between experimental data and Monte Carlo simulation.

Résumé

La micro-analyse quantitative des surfaces rugueuses est un grand défi dans le domaine de la microscopie. Bien que la micro-analyse par rayons X puisse être un outil utile pour la caractérisation préliminaire, elle n'est pas quantitative car la géométrie des surfaces rugueuses introduit des problèmes qui ne sont pas présents dans la micro-analyse d'un échantillon massif. Le problème de la micro-analyse quantitative des surfaces rugueuses est que les électrons peuvent être diffusés de tous les côtés en raison des différentes pentes de la surface. Par conséquent, la géométrie des surfaces rugueuses a un impact sur les intensités de rayons X générées, émises ou mesurées et donc sur l'analyse quantitative de la surface. La présente étude de doctorat se concentre sur la fabrication d'une technique de reconstruction 3D pour les surfaces de fracture et sur la production d'une méthode quantitative pour caractériser les surfaces non planes par microscopie électronique. Dans un premier temps, un ensemble d'expériences, de techniques d'imagerie et de modélisation a été conçu pour obtenir des images numériques 3D des surfaces de fracture. En utilisant les signaux rétrodiffusés, une reconstruction numérique 3D a été obtenue. Les effets des paramètres du SEM sur la précision du modèle de reconstruction 3D qui sont pris via les images BSE ont été étudiés. Les résultats ont montré que la meilleure gamme de la distance de travail pour notre système est de 9 à 10 mm. Il a été démontré qu'en augmentant le grossissement à 1000X, les résultats de la reconstruction numérique 3D se sont améliorés. Cependant, il n'y a pas eu d'amélioration significative en augmentant le grossissement au-delà de 1000X. En outre, les résultats ont montré que plus la tension d'accélération est faible, plus la technique de reconstruction 3D est précise, à condition que les signaux rétrodiffusés soient propres. En outre, le comportement du rapport pic/bruit de fond (P/B), l'une des méthodes quantitatives candidates pour la caractérisation des surfaces rugueuses, a été analysé en modifiant l'angle de décollage, l'angle d'inclinaison, la taille des particules et l'énergie du faisceau. Il a été observé que le P/B dépend fortement de l'énergie du faisceau, de la taille des particules et de la composition des substrats. Les résultats indiquent que le P/B augmente à des angles d'inclinaison élevés. Les résultats ont montré qu'en augmentant l'angle de décollage, le P/B diminue initialement puis atteint un plateau. Les données ont montré que le P/B augmente lorsque le faisceau d'électrons est déplacé du centre vers

le côté d'une particule. De plus, le P/B est plus sensible au mouvement du faisceau pour les particules sphériques que pour les particules cubiques. Dans l'étape suivante, un facteur de correction géométrique (G) a été introduit pour la caractérisation quantitative des particules. L'utilisation de la nouvelle méthode ZAFG permet de quantifier les particules sans utiliser la simulation de Monte Carlo. L'ajout d'un facteur géométrique à la méthode ZAF conventionnelle crée un moyen très facile et simple de quantifier les particules. Les analyses ont montré que le facteur G est fonction de D/X_e, où D est le diamètre des particules, et X_e est la gamme des rayons X émis dans un échantillon global de même composition chimique. Il a été démontré que lorsque X_e devient supérieur à D, le facteur G se décompose exponentiellement à mesure que l'énergie des électrons incidents augmente. Les données ont montré que lorsque D/X_e > 1 pour une particule, alors G = 1. Dans cette situation, la particule fonctionne presque comme un échantillon global. Il a été démontré que le facteur G ne dépend que de D/X_e, ni de la composition chimique, ni de l'énergie du faisceau. Enfin, dans ce travail, des résultats préliminaires ont été présentés en utilisant une surface de fracture réelle. Le logiciel de Monte Carlo existant MC Xray a été incorporé dans le logiciel de traitement d'images Dragonfly développé par Object Research Systems (ORS) Inc. L'incorporation de MC X-ray dans Dragonfly permet aux utilisateurs d'effectuer des simulations de Monte Carlo pour toute géométrie complexe. Un excellent accord a été observé entre les données expérimentales et la simulation Monte Carlo.

Acknowledgments

Throughout the writing of this dissertation, I have received a great deal of support and assistance. I would first like to thank my supervisor, Prof. Raynald Gauvin, whose expertise was invaluable in formulating the research questions and methodology. Your insightful feedback pushed me to sharpen my thinking and brought my work to a higher level.

My appreciation also goes to Mr. Nicolas Brodusch, for helping me in the experimental part of the study. Dear Nicolas, you provided me with the tools that I needed to choose the right direction and successfully complete my dissertation.

I would like to acknowledge my colleagues in McGill Electron Microscopy Research Group:

Dr. Yu Yuan, Dr. Samantha Rudinsky, Ms. Sabrina Clusiau, Mr. Frédéric Voisard, Ms. Stéphanie Bessette, Mr. Ali Jaberi, Mr. Nicolas Dumaresq, Mr. Meysam Naghizadeh for their supports.

I would particularly like to single out my supportive at ORS. Co, Dr. Nicolas Piché. Nicolas, I want to thank you for your patient support.

I could not have completed this dissertation without the support of my dear friend, Mr. Giacomo Daniel Di Silvestro, who provided comments on the papers and thesis.

I would like to thank my funding agencies without which the project would not have been possible. Acknowledgment is due to Natural Sciences and Engineering Research Council (NSERC) of Canada, McGill Engineering Doctoral Award (MEDA), and Graduate Excellence Fellowships in Engineering for the financial assistance on my research.

In addition, I would like to thank my parents for their wise counsel and sympathetic ear. You are always there for me.

Finally, I could not have completed this dissertation without the support of my love, Lida Radan, and Jana Radan, my lovely daughter, who provided love and accompany during the whole journey.

Contribution of authors

This thesis was prepared using a manuscript-based format according to the guidelines published by the Graduate and Postdoctoral Studies office of McGill University. The following four manuscripts are included in the present thesis. The fourth manuscript is a short abstract that was accepted at the microscopy and microanalysis (M&M) conference and was published in the M&M journal; however, research still undergoing for this chapter and will publish as a full article soon.

- 1. S. M. Bayazid, N. Brodusch, R. Gauvin, Investigation of the Effect of Magnification, Accelerating Voltage, and Working Distance on the 3D Digital Reconstruction Techniques, Scanning 2020, (2020) 3743267 (Chapter 3).
- 2. S. M. Bayazid, Y. Yuan, R. Gauvin, Study of the Peak to Background (P/B) Method Behavior as a Function of Take-Off Angle, Tilt Angle, Particle Size, and Beam Energy, Scanning 2021, (2021) 8070721 (Chapter 4).
- 3. S. M. Bayazid, N. Brodusch, N. Dumaresq, R. Gauvin, A Universal Equation of Geometrical Correction Factor for Quantitative Characterization of Particles, ZAF(G) method, Microchemica Acta 2022, (to be submitted 2022) (Chapter 5).
- 4. S. M. Bayazid, R. Gauvin, Using 3D Reconstruction Technique Along with Monte Carlo Modelling for Quantitative Characterizations of Fracture Surface of Monel Alloy, Microscopy and Microanalysis (Chapter 6).

Mr. SeyedMahmoud Bayazid developed all the models, conducted all the simulations, analyzed the results, and wrote the manuscripts. All the manuscripts were supervised by Prof. Raynald Gauvin, who provided guidance and supplied scientific advice throughout the whole project. Mr. Nicolas Brodusch helped in the revision of the manuscript for Chapter 3 and 5. Dr. Yu Yuan involved in the discussion of the results and the manuscript revision for Chapter 4.

Table of Contents

Abstract	I
Résumé	III
Acknowledgments	V
Contribution of authors	VI
Table of Contents	VII
Abbreviations	XI
Lists of tables	XII
Lists of figures	XIII
Chapter 1. Introduction	1
References	4
Chapter 2. Literature review	1
2. 1. Fractography	1
2. 1. 1 Quantitative Fractography	2
2. 2. Interaction of Electron with Samples	5
2. 3. Secondary Electron	8
2. 4. Backscattered Electron	9
2. 5. Characteristic X-Rays	9
2. 5. 1 X-ray absorption	11
2. 5. 2 φ (ρz) curve	13
2. 6. Quantitative x-ray microanalysis of flat samples	14
2. 6. 1 X-ray detection	14
2. 6. 2 Traditional quantification approaches	16
2. 7. Monte Carlo Modeling	18

2. 7. 1 Monte Carlo method	18
2. 7. 2 Monte Carlo program	22
2. 8. 3D Reconstruction methods	23
2. 8. 1 3D reconstruction from multiple images	23
2. 8. 2 Secondary electron (SE) or backscattered electron (BSE) signals for 3D	
reconstruction	26
2. 8. 3 3D rebuilding of fracture surfaces	27
2. 9. Quantitative x-ray microanalysis of rough surfaces	33
2. 9. 1 Peak to Background method	33
2. 9. 2 Armstrong model	37
2. 10. References	42
Chapter 3. Investigation of the Effect of Magnification, Accelerating Voltage, and Working	
Distance on the 3D Digital Reconstruction Techniques	51
3. 1. Abstract	52
3. 2. Introduction	53
3. 3. Method	54
3. 4. Results	55
3. 5. Discussion	61
3. 6. Conclusion	62
3. 7. Acknowledgments	63
3. 8. References	63
Chapter 4. Study of the Peak to Background (P/B) Method Behavior as a Function of Take-O	ff
Angle, Tilt Angle, Particle Size, and Beam Energy	66
4. 1. Abstract	67
4. 2. Introduction	68
4 3 Method	69

4. 4. Results	70
4. 4. 1 Beam energy	70
4. 4. 2 Tilt angle	72
4. 4. 3 Take-off angle	73
4. 4. 4 Particle size	75
4. 5. Discussion	77
4. 6. Conclusion.	78
4. 7. Acknowledgments	79
4. 8. References	79
Chapter 5. A Universal Equation of Geometrical Correction Factor for Quantitative	
Characterization of Spherical Particles	81
5. 1. Abstract	82
5. 2. Introduction	83
5. 3. Description of the geometrical correction factor (G)	84
5. 4. Materials and Method	87
5. 5. Results and discussion	87
5. 5. 1 Validation of the ZAF(G) Model	91
5. 6. Conclusion.	94
5. 7. Acknowledgment	94
5. 8. Declarations	94
5. 9. Reference	94
Chapter 6. Using 3D Reconstruction Technique along with Monte Carlo Modelling for	
Quantitative Characterizations of Fracture Surface of Monel Alloy	97
6. 1. Introduction	98
6. 2. Materials and Method	98
6.3 Results and discussion	99

6. 4. References	102
Chapter 7. Concluding remarks	103
7. 1. Conclusion	103
7. 2. Contributions to original knowledge	

Abbreviations

AFM atomic force microscopy

BSE backscattered electron

CAGD computer aided geometric design

EDS energy-dispersive spectrometry

EPMA electron probe microanalysis

MVS multi view stereo

P/B peak to background

PCL point cloud library

PPT python photogrammetry toolbox

SE secondary electron

SE-IL secondary electron In lens detector

SEM scanning electron microscopy

SFM structure from motion

TEM transmission electron microscopy

2D two-dimensional

3D three-dimensional

4Q-BSE four-quadrant detector

Lists of tables

Table 2-1 Comparison between SE and BSE in imaging [1]	26
Table 2-2 K411 fragments [1]	34
Table 5-1 Weight fractions of Ca, Mg, Fe, Si, and O in the NIST- K411 standard particles	
measured with EDS standard quantitative analysis, and the ZAF(G) method	93
Table 6-1 Comparison of the ratio of the net X-Ray intensity (Ifracture surfaceIflat surface	e) for
experimental EDS map and Monte Carlo Simulation	. 101

Lists of figures

Figure 2-1 a) Surface of a fatigue fracture [4]; b) Classification of fracture features [5]	2
Figure 2-2 Geometry of image formation in the SEM [5]	3
Figure 2-3 Estimation of the parallax Δx for a tilt angle 2α [8].	Ļ
Figure 2-4 Signals emitted from different parts of the interaction volume [37]	5
Figure 2-5 a) an energetic electron is deflected by the electrical field of an atom at location P1	
through an angle φ elastic; b) The energetic electron scatters elastically at point P1 and can land	
at any location on the circumference of the base of the cone with equal probability; and c)	
Schematic illustration of a second scattering step, carrying the energetic electron from point P2	
to point P3 [1]	3
Figure 2-6 X-ray generation in Carbon from the interaction of high-energy electrons [1] 11	L
Figure 2-7 Mass absorption coefficient as a function of the X-ray photon energy for a Cu	
specimen from Ref. [42]	3
Figure 2-8 Generated and emitted $\phi(\rho z)$ curves for the Al K α line in pure Al at 15 keV, simulated	1
using MC X-ray [55]14	Ļ
Figure 2-9 Geometry used to simulate the trajectory of an electron using the single scattering	
model from Ref. [75])
Figure 2-10 Electron trajectories of 200 electrons at 10 keV in carbon using CASINO2 [77] 21	L
Figure 2-11 a) Simulated X-ray spectrum and b) $\phi(\rho z)$ curves for a Si substrate with a 200 nm Cr	•
coating at 15 keV using MC X-ray [78]	2
Figure 2-12 Illustration of the basic principles of shape-from-stereo (stereo reconstruction) 25	5
Figure 2-13 a) Non-flat surface of aluminum; b) Non-flat profile after 3D reconstruction using	
SE-IL images; c) Non-flat surface of aluminum; and d) Non-flat profile obtained by AFM [13].	
	3
Figure 2-14 a) 3D reconstructions of the datasets with their corresponding AFM height fields	
(yellow); b) three profiles have been traced on the AFM micrographs; c) the altimetric traces	
corresponding to each profile; and d) the altimetric traces of the analogous profiles on the SEM	
reconstructions [30])
Figure 2-15 Reconstructed surfaces of: (a) ceramic material; (b) synthesis earth magma; and (c)	
syntactic foam [36]	

Figure 2-16 The 3D profile of fracture surface of Charpy specimen 3 (60°C) [36]
Figure 2-17 Geometrical characteristics of fracture surface; a) Typical view of the ductile broken
Charpy V-notch specimen; b) Typical view of the brittle broken Charpy V-notch specimen; and
c) Schematic view of geometrical characteristics [36]
Figure 2-18 EDS spectra of NIST- K411 in the flat polished condition, and from four fragments,
showing the variation in the spectral shape from the ideal [1]
Figure 2-19 Schematic of X-ray path lengths in (A) thick flat specimen and (B) particle [110].38
Figure 2-20 X-ray k ratio as a function of the beam position on a non-flat surface for the Ni K_{α}
and L_{α} lines and the Al K_{α} line. The k ratios have been computed relative to a flat NiAl
specimen. X corresponds to the height [56]
Figure 2-21 Comparison between a simulated and a measured Ti 90.5 wt% - Al 6.1wt%-V
3.4wt% [75]
Figure 3-1 The spherical particles of Ti-6Al-4V on the silicon substrate
Figure 3-2 A 4-Q BSE detector. 55
Figure 3-3 Backscattered electron images taken by 4-Q BSE detector at different magnification;
a) 500X, b) 1000X, and c) 2000X
Figure 3-4 3D digital reconstructed image along with profile at different magnification; a) 500X,
b) 1000X, and c) 2000X
Figure 3-5 Backscattered electron images taken by 4-Q BSE detector at different accelerating
voltage; a) 3 kV, b) 10 kV, and c) 20 kV
Figure 3-6 3D digital reconstructed image along with profile at different accelerating voltage; a)
3 kV, b) 10 kV, and c) 20 kV
Figure 3-7 Backscattered electron images taken by 4-Q BSE detector at different working
distance; a) 7 mm, b) 9 mm, and c) 11 mm
Figure 3-8 3D digital reconstructed image along with profile at different working distance; a) 7
mm, b) 9 mm, and c) 11 mm
Figure 3-9 Relative radius versus; a) magnification, b) accelerating voltage, and c) working
distance (Each graph represents one particle)
Figure 4-1 Definition of the P/B ratio. P is the net intensity of the characteristic line (e.g. $K\alpha$
line) an B is the background intensity at the line energy

Figure 4-2 Variation of peak (Al-Kα line) intensity, background (continuum X-ray) intensity,
and the P/B as a function of beam energy
Figure 4-3 The peak intensity, background intensity, and the P/B as a function of tilt angle 72
Figure 4-4 Variation of f ratio given by (IMax Al K α) / (IMax Al K α + IMax Au M α) as function
of tilt angle (Al deposited on Ti)
Figure 4-5 The P/B of Al-K α as a function of take-off angle
Figure 4-6 Variation of f ratio given by (IMax Al K α) / (IMax Al K α + IMax Au M α) as function
of take-off angle (Al particle deposited on Au)
Figure 4-7 Variation of the P/B, and f ratio as function of D/Xe (5 keV) for Al K α ; Xe is the
range of emitted X rays for the bulk sample, in this case at 5 keV
Figure 4-8 Variation of the P/B as a function of beam position
Figure 5-1 Effect of particle geometry on the generated, emitted X-Ray intensities, and the
absorption path
Figure 5-2 Geometry used to simulate particle on substrate
Figure 5-3 The G correction factor as a function of the beam energy for different particle size. 88
Figure 5-4 Variation of the G factor for all elements in NIST- K411 as a function of DXe 90
Figure 5-5 Error distribution of the G factor obtained from simulation and universal Equation
5.16 when <i>DXe</i> is altered
Figure 5-6 Flowchart for the validation of the universal equation (Equation 5.16)
Figure 5-7 a) Error distribution of the measured composition vs the nominal composition, and b)
Error distribution of the measured composition vs particle size
Figure 6-1 BSE images, and EDS maps for the fracture surface of Monel alloy, a) BSE, b) EDS
map Ni Kα, and c) EDS map Cu Kα
Figure 6-2 BSE images, and EDS maps for the fracture surface of Monel alloy, a) SE, b) EDS
map Ni K α , and d) EDS map Cu K α
Figure 6-3 Simulation data for the same surface used in Figure 6-1, a) BSE image, b) EDS map
Ni K α , and c) EDS map Cu K α
Figure 6-4 Simulation data for the same surface used in Figure 6-2, a) BSE image, b) EDS map
Ni Kα, and c) EDS map Cu Kα
Figure 6-5 The effect of beam energy on EDS map, left-side) Experimental data at $E=20\ keV$,
right-side) Simulation data for the same surface at $E = 10 \text{ keV}$ and $E = 20 \text{ keV}$

Chapter 1. Introduction

Fracture is the separation of a material into two or more pieces under the action of stress. The fracture of a material usually happens due to the development of certain displacement discontinuity surfaces within the solid. The fracture surface is one the most critical parts of fractography (the study of fracture surface), in which the information associated with this region can significantly affect the accuracy of quantitative analysis. In the quantitative characterization of fracture surfaces, the quality of the results can be affected in different ways, namely, image processing, hardware and software development, knowledge in fractography, electron microscopy, and modeling methods [1]. Development of the scanning/transmission electron microscopy (SEM/STEM) can significantly help in quantitative characterization of fracture surfaces, especially when it combines with Energy Dispersive X-ray Spectrometry (EDS). SEM use electrons for imaging in a similar way that light microscopes use visible light. Unlike transmission electron microscopes (TEMs), which detect electrons that pass through a very thin specimen, SEMs use the electrons that are reflected or knocked off the near-surface region of a sample to create an image. EDS is a technique for determining the elemental composition of materials in the Scanning or Transmission Electron Microscope (SEM/TEM). It uses the intensity of emitted X-Rays to get chemical composition. Converting the X-ray intensity into elemental concentration, using conventional methods, are valid for specimens having homogeneous composition and flat surfaces [2], but the fracture surfaces are non-flat. Earlier efforts that have been made to compute complete X-ray spectra for non-flat surfaces generally fall into two categories, closed form analytical models and Monte Carlo models [3, 4].

There are some uncertainties in either the correctness of the physical models or the parameters used in both approaches. Pouchou et al. [4] developed the quantitative schemes for quantitative X-ray microanalysis of multi-layered specimens, which are based on the Φ (ρ z) (a quantitative X-ray microanalysis method). Subsequently, this method extended for the microanalysis of surface segregation by Pouchou et al. [5]. In addition to these activities, a quantitative method was proposed for the microanalysis of spherical inclusions embedded in a matrix [6] as well as Monte Carlo simulations of X-ray emission from porous materials by Gauvin et al [7, 8]

For the case of samples having a rough surface, Statham [9] proposed a quantitative model based on the Peak to Background ratio (P/B), using photons of the same energy nets. Based on this method, the P/B is constant at any location on the non-flat surface and that this ratio is the same as that of a bulk material of the same composition having a flat surface. By assuming that this proposal is correct, it is possible to convert rough sample intensity data into the intensity values measured for a flat sample of the same composition and thereby using the conventional quantitative analysis methods already mentioned. However, by using a new generation of Monte Carlo program, Gauvin et al. [10] showed that the P/B is not constant for the rough surfaces. Gauvin demonstrated that this method has some weakness. For instance, the assumption that the P/B is independent of the specimen non-flat is not strictly correct since the ionization cross sections and the Bremstrahlung cross sections are not the same. More recently Gauvin et al. [3] described a new Monte Carlo program (MC X-Ray) that predicts X-ray spectra measured with an energy dispersive spectrometer (EDS). There was an excellent prediction between an X-ray spectrum measured and a simulated spectrum by using MC X-Ray. Their new Monte Carlo program can simulate the complete X-ray spectrum of a given material of homogeneous composition.

Consequently, the quantitative chemical microanalysis of the fracture surfaces with conventional methods needs to be modified to be useful for the non-flat fracture surfaces. The main problem of using conventional method is the geometrical factors such as size and shape of non-flat features which significantly influence the measured x-ray intensities due to the absorption and stopping power phenomena [11]. It is believed that having geometric information of the fracture surfaces can solve this problem to a great extent.

Therefore, the present Ph.D. study has been focused on fabrication of a 3D digital reconstruction technique to obtain geometrical information of the fracture surfaces, and improvement of the quantitative chemical characterization method, which will be useful for the chemical characterization of non-flat surfaces.

Some contributions to original knowledge are intended to be offered with this PhD project:

1. For the first time, in this Ph.D. study, a quantitative method was developed to reconstruct 3D digital images of fracture surfaces using BSE images.

- 2. In this study, for the first time, the effect of SEM parameters such as Magnification, Accelerating Voltage, and Working Distance on the 3D digital rebuilding technique was investigated.
- 3. For the first time, this study introduced a geometrical correction factor for quantitative microanalysis of particles.
- 4. This study, will help us to describe fracture behaviors that create due to chemical composition problems.
- 5. Eventually, this is the first study that established a method for quantitative characterization of fracture surfaces via scanning electron microscopy.

This thesis consists of several chapters. Chapter 1 presents the objectives of the research. An extensive literature review is given in Chapter 2. Chapter 3 introduces the modeling technique to get the 3D digital image of the fracture surfaces. Moreover, the effect of SEM parameters on the 3D digital reconstruction technique is investigated in this chapter. Chapter 4 presents the behavior of the P/B (one of the candidates for quantitative microanalysis of rough surfaces) as a function of different parameters to show "Does the efficiency of this method of analysis for particles or rough surfaces is enough?". A universal equation is introduced in Chapter 5 for geometrical correction factor to extract the quantitative microanalysis of particles. Chapter 6 illustrates primarily results of microanalysis of a real fracture surface. Chapter 7 offers the major conclusions, contributions to original knowledge, and future work.

References

- 1. Kuna, M., Finite elements in fracture mechanics. Solid Mechanics and Its Applications, 2013. 201: p. 153-192.
- 2. Poirier, D. and R. Gauvin, X-ray microanalysis of porous materials using Monte Carlo simulations. Scanning, 2011. 33(3): p. 126-34.
- 3. Gauvin, R., et al., Win X-ray: A New Monte Carlo Program that Computes X-ray Spectra Obtained with a Scanning Electron Microscope. Microscopy and Microanalysis, 2006. 12(1): p. 49-64.
- 4. Pouchou, J. and F. Pichoir, Electron probe X-ray microanalysis applied to thin surface films and stratified specimens. Scanning Microscopy, 1993. 1993(7): p. 12.
- 5. Pouchou, J., A new model for quantitative analyses. I. Application to the analysis of homogeneous samples. Rech. Aerospat., 1984. 3: p. 13-38.
- 6. Gauvin, R., P. Hovington, and D. Drouin, Quantification of spherical inclusions in the scanning electron microscope using Monte Carlo simulations. Scanning, 1995. 17(4): p. 202-219.
- 7. Gauvin, R., Review of transmission electron microscopy for the characterization of materials. Optical Science, Engineering and Instrumentation '97. Vol. 10291. 1997: SPIE.
- 8. Gauvin, R., X-Ray Emission from Porous Materials : New Results. Microscopy and Microanalysis, 1998. 4(S2): p. 206-207.
- 9. Statham, P., Measurement and use of peak-to-background ratios in X-ray analysis. Mikrochimica Acta, 1979. 8: p. 229-242.
- 10. Gauvin, R. and E. Lifshin, X-ray microanalysis of real materials using Monte Carlo simulations. Microchimica Acta, 2004. 145(1): p. 41-47.
- 11. Goldstein, J.I., et al., Scanning electron microscopy and X-ray microanalysis. 2017: Springer.

Chapter 2. Literature review

Research on the failure of materials can save lives as well as reduce costs. In this way, assessment of fracture surfaces can provide a wealth of information on the behavior of materials to prevent their failure. Therefore, having a proper quantitative method is measuring to understand the precise role of each feature in the fracture process. Quantitative x-ray microanalysis is an analytic implement, which enables factual estimates of the flat surfaces [1]. However, the non-flat of the fracture surface can directly influence the accuracy of quantitative x-ray microanalysis with conventional methods. Therefore, having a quantitative method for the fracture surface analyzing is necessary. The present work focuses on the quantitative characterization of fracture surfaces via Scanning Electron Microscopy (SEM).

In this chapter, the principles of fractography are first introduced (section 2.1). The 3D reconstruction methods are then presented (section 2.2). Section 2.3 is related to the interaction of electrons with the specimen. The detection of X-ray signals and several traditional methods for quantitative X-ray microanalysis of homogeneous flat materials are then presented (section 2.4). The Monte Carlo method is introduced in section 2.5. Finally, several traditional methods for quantitative X-ray microanalysis of rough materials are reviewed (section 2.6).

2. 1. Fractography

In 2016, it was estimated that the annual cost of fatigue of materials to the U.S. economy is around \$100 billion per year [2]. This overwhelming cost for failure due to fracture is the prime motivation for this study. One of the objectives of all failure processes is to understand fracture surface (Figure 2.1) and to get more information about it. Quantitative characterization of the fracture surface, that is, quantitative fractography, can provide useful information regarding the microstructural features and failure mechanisms that govern the material fracture [3].

Development of scanning electron microscopy (SEM) has led to significant advances in quantitative fractography. The X-ray in Energy Dispersive X-ray Spectrometry (EDS spectrum) is a good prelude to quantitative analysis as it will allow the best operating parameters for the microscope to be selected [4]. In order to quantify the characterization of fracture surfaces of engineering materials with SEM, knowledge of fractography in theory must be understood.

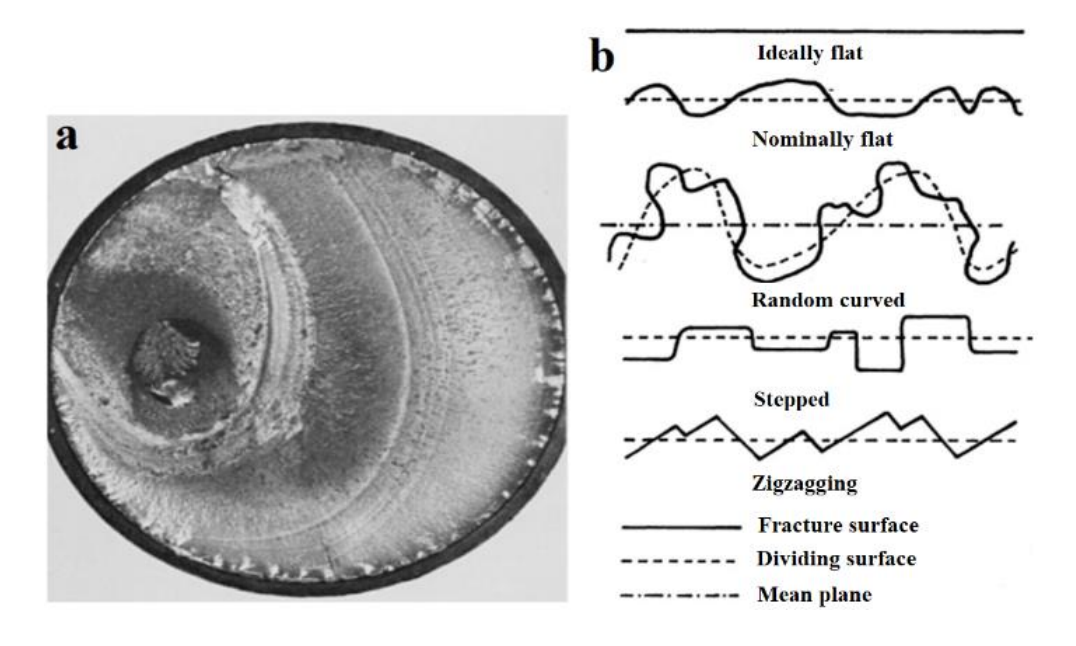


Figure 2-1 a) Surface of a fatigue fracture [4]; b) Classification of fracture features [5].

Fractography is the study of the fracture surfaces of materials to develop a failure mode and tries to disclose the superficial features on the fracture by visual inspections, looking for the propagation patterns and fracture origin. Through this characterization, it is possible to explore and determinate previous conditions that would help find the causes of the fracture [6].

2. 1. 1 Quantitative Fractography

The aim of quantitative fractography is to prompt the features and important characteristics of a fracture surface in terms of surface areas, lengths, sizes, numbers, shapes, orientations, and locations, as well as distributions of these quantities. The general availability of the SEM opened up new avenues toward the understanding of fracture structures in three dimensions. The more prominent current techniques for studying the fracture surface can be classified in accordance with the following: 1) Stereoscopic methods, 2) Projected images, and 3) Profile generation. As the stereoscopic methods are most usable, in the next part this method will be discussed in detail. The reader can refer to the reference [5, 7] for more information about Projected images, and Profile generation methods.

2. 1. 1. 1 Stereoscopic Methods

This category is including stereoscopic imaging and measurements, photogrammetric methods, and deep etching on the surface. Here, only the stereoscopic imaging is given more explanation, and the reader can refer to the reference [5] for more information about other methods.

2. 1. 1. 2 Stereoscopic Imaging

Stereoscopic pictures can be taken by SEM and TEM quite readily. In any SEM image (SE/BSE), there are two main kinds of distortion: (1) perspective error created by tilting, and (2) magnification errors caused by surface irregularities. Keeping the beam close to perpendicular to the fracture surface could diminish the first type of error. The magnification error that is the rectilinear optical equivalent of the SEM image is shown in Figure 2-2 [5]. Magnification is defined as the ratio of the image distance to the object distance. In the case of an irregular surface, the object distance is not constant. Consequently, high points on the surface have higher magnification than low points. For example, at point p in Figure 2-2, the magnification is proportional to ss'/sm, whereas at point q it is proportional to ss'/sm. Stereo-SEM pairs (two images of the same field taken at small tilt angle) make it possible to measure the coordinates of any point in the fracture surface. The geometry of this is shown in Figure 2-2 [5, 8].

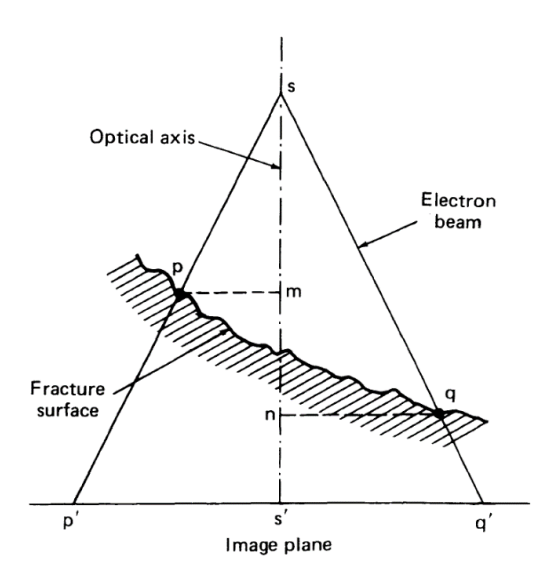


Figure 2-2 Geometry of image formation in the SEM [5].

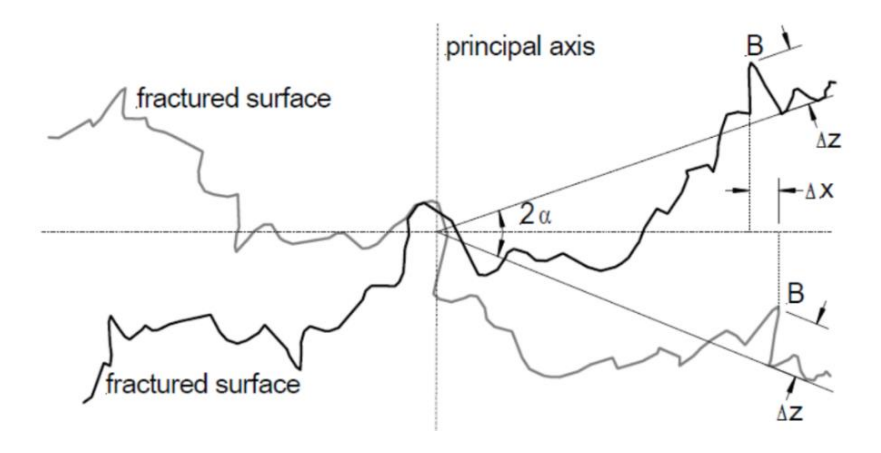


Figure 2-3 Estimation of the parallax Δx for a tilt angle 2α [8].

The main task of the stereoscopic procedure is to determine the relative vertical position Δz for all sampled surface points. For this purpose, the following Equation (2.1) is used [5]:

$$\Delta z = \left[\frac{1}{2M \sin \alpha}\right] \Delta x \tag{2.1}$$

where the height difference, Δz , between two points is determined directly from the measured parallax, Δx . Dividing Δx by the average magnification, M, then gives Δz in terms of the actual height difference [9, 10]. Since the tilt angle is fixed for one pair of photographs, Equation 2.1 may be rewritten as:

$$\Delta z = K \Delta x \tag{2.2}$$

where K characterizes the constant terms.

Equation 2.1 is strictly correct for an orthogonal projection; that is, the point *s* in the Figure 2-2 is situated at infinity. This is a reasonable assumption at higher magnifications (> 1000X), but at lower magnifications induced errors appear [11]. The x and y coordinate points can be measured directly with a superimposed grid or obtained automatically with suitable equipment [12]. Once the (x, y, z) coordinates at selected points on the fracture surface obtained, elementary calculations can be made, such as the equation of a straight line or a planar surface, the length of a linear segment between two points in space, the angle between two lines or two surfaces, and so forth [13]. But one of the limitations of stereoscopic methods is that flat, featureless areas do not have matching points in both images, so there is "data dropout" in those areas [14, 15]. Fortunately, this cannot make limitation for fracture surfaces.

2. 2. Interaction of Electron with Samples

In the SEM, the beam electrons interact with the specimen atoms through a variety of physical processes collectively referred to as "scattering events." Image formation and microanalysis in the SEM is dependent on the acquisition of signals produced from the electron beam and specimen interactions. The overall effects of these scattering events are to transfer energy to the specimen atoms from the beam electrons, thus setting a limit on their travel within the solid, and to alter the direction of travel of the beam electrons away from the well-defined incident beam trajectory. These beam electron–specimen interactions produce the backscattered electrons (BSE), secondary electrons (SE), and X-rays that convey information about the specimen, such as coarse- and finescale topographic features, composition, and crystal structure. At the level needed to interpret SEM images and to perform electron excited X-ray microanalysis, the complex variety of scattering processes will be broadly classified into "inelastic" and "elastic" scattering. The combined effect of elastic and inelastic scattering controls the penetration of the electron beam into the solid. The resulting region over which the incident electrons interact with the sample is known as interaction volume (see Figure 2.10) which is the region of the specimen in which the beam electrons travel and deposit energy. The interaction volume has several important characteristics, which determine the nature of imaging in the SEM. Inelastic scattering refers to a variety of physical processes that act to progressively reduce the energy of the beam electron by transferring that energy to the specimen atoms through interactions with tightly bound inner-shell atomic electrons and loosely bound valence electrons. These energy loss processes include ejection of weakly bound outer-shell atomic electrons (binding energy of a few eV) to form secondary electrons; ejection of tightly bound inner shell atomic electrons (binding energy of hundreds to thousands of eV) which subsequently results in emission of characteristic X-rays; deceleration of the beam electron in the electrical field of the atoms producing an X-ray continuum over all energies from a few eV up to the beam's landing energy (E₀) (bremsstrahlung); and heating of the specimen (phonon production) [1, 37].

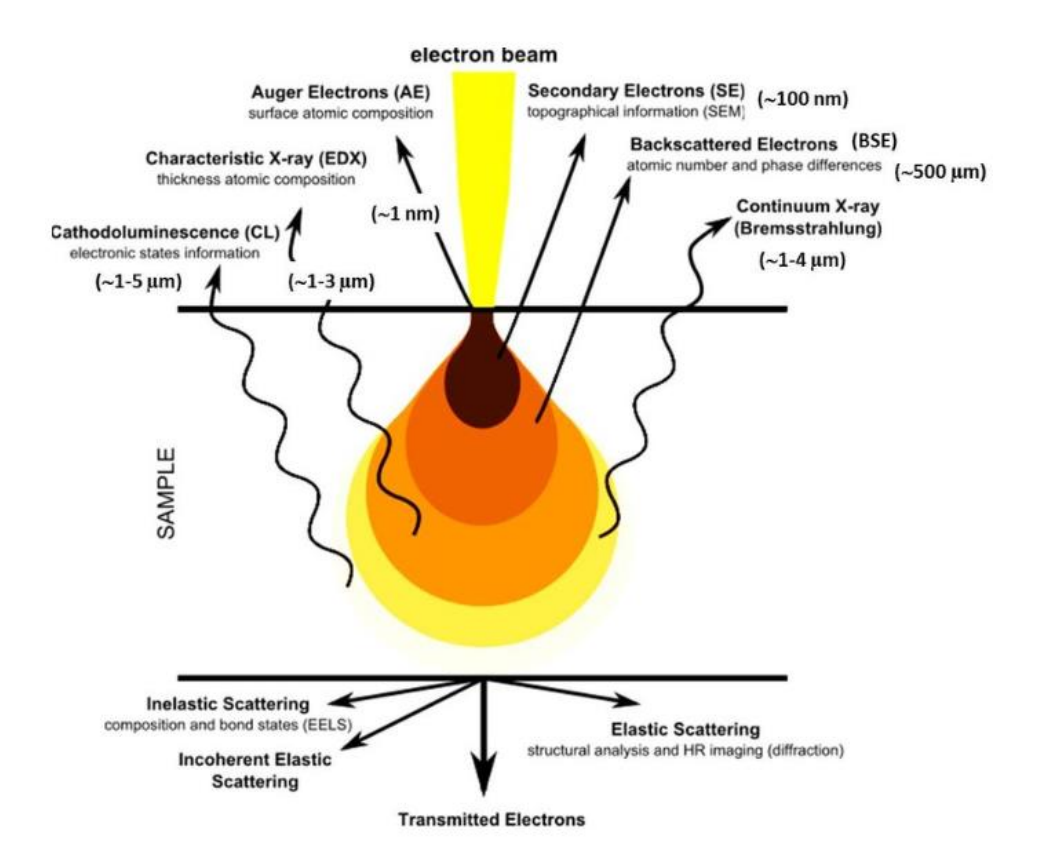


Figure 2-4 Signals emitted from different parts of the interaction volume [37].

The energy loss due to inelastic scattering sets an eventual limit on how far the beam electron can travel in the specimen before it loses all of its energy and is absorbed by the specimen. To understand the specific limitations on the distance traveled in the specimen imposed by inelastic scattering, a mathematical description is needed of the rate of energy loss (incremental dE, measured in eV) with distance (incremental ds, measured in nm) traveled in the specimen. Although the various inelastic scattering energy loss processes are discrete and independent, Bethe [38]summarized their collective effects into a "continuous energy loss approximation" [1]:

$$\frac{\mathrm{dE}}{\mathrm{ds}} \left(\frac{\mathrm{eV}}{\mathrm{nm}} \right) = -7.85 \left(\frac{\mathrm{Zp}}{\mathrm{AE}} \right) \ln \left(\frac{1.166\mathrm{E}}{\mathrm{J}} \right) \tag{2.3}$$

where E is the beam energy (keV), Z is the atomic number, ρ is the density (g/cm³), A is the atomic weight (g/mol), and J is the "mean ionization potential" (keV) given by:

$$J(keV) = (9.76Z + 58.5Z^{-0.19}) \times 10^{-3}$$
(2.4)

Simultaneously with inelastic scattering, "elastic scattering" events occur when the beam electron is deflected by the electrical field of an atom (the positive nuclear charge as partially shielded by the negative charge of the atom's orbital electrons), causing the beam electron to deviate from its previous path onto a new trajectory, as illustrated schematically in Figure 2.11. The probability of elastic scattering depends strongly on the nuclear charge (atomic number Z) and the energy of the electron, E (keV) and is expressed mathematically as a cross section, Q [1]:

$$Q_{elastic(>\varphi_0)} = 1.62 \times 10^{-20} \left(\frac{Z^2}{E^2}\right) \cot^2(\frac{\varphi_0}{2}), \text{ [events>} \varphi_0/[\text{electron}\left(\frac{\text{atom}}{\text{cm}^2}\right)]$$
 (2.5)

where ϕ_0 is a threshold elastic scattering angle. Despite the angular deviation, the beam electron energy is effectively unchanged in energy. Elastic scattering causes beam electrons to deviate out of the narrow angular range of incident trajectories defined by the convergence of the incident beam as controlled by the electron optics.

The elastic scattering cross section, Eq. 2.5, can be used to estimate how far the beam electron must travel on average to experience an elastic scattering event, a distance called the "mean free path," λ [1]:

$$\lambda_{elastic}(nm) = 10^7 \frac{A}{[N_0 \rho Q_{elastic}(>\phi_0)]}$$
 (2.6)

where A is the atomic weight (g/mol), N_0 is Avogadro's number (atoms/mol), and ρ is the density (g/cm³).

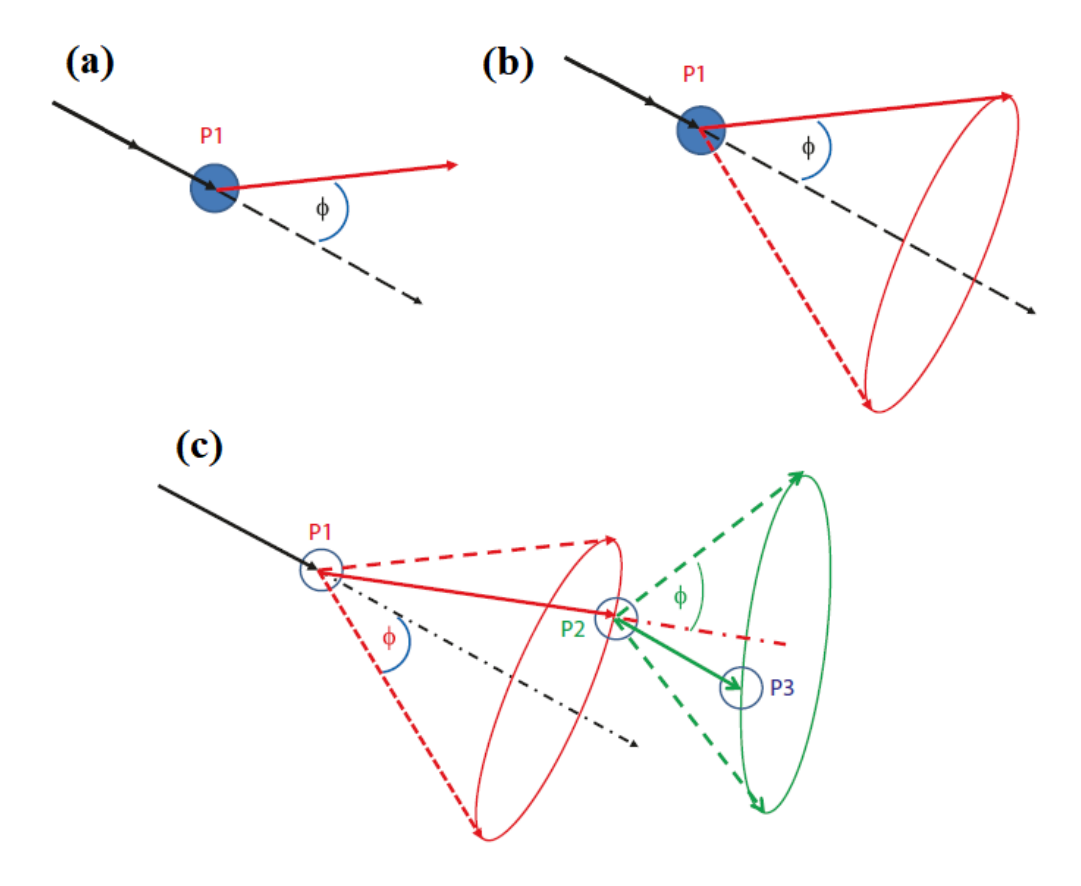


Figure 2-5 a) an energetic electron is deflected by the electrical field of an atom at location P1 through an angle φ elastic; b) The energetic electron scatters elastically at point P1 and can land at any location on the circumference of the base of the cone with equal probability; and c) Schematic illustration of a second scattering step, carrying the energetic electron from point P2 to point P3 [1].

2. 3. Secondary Electron

Secondary electrons (SE) are created when inelastic scattering of the beam electrons ejects weakly bound valence electrons (in the case of ionically or covalently bonded materials) or conduction band electrons (in the case of metals), which have binding energies of $\sim 1-15$ eV to the parent atom(s). Secondary electrons are quantified by the parameter δ , which is the ratio of secondary electrons emitted from the specimen, N_{SE} , to the number of incident beam (primary) electrons, N_B [1]:

$$\delta = \frac{N_{SE}}{N_b} \tag{2.7}$$

2. 4. Backscattered Electron

A significant fraction of the incident beam electrons undergoes sufficient scattering events to completely reverse their initial direction of travel into the specimen, causing these electrons to return to the entrance surface and exit the specimen. These beam electrons that escape from the specimen are referred to as "backscattered electrons" (BSE) and constitute an important SEM imaging signal rich in information on specimen characteristics. The BSE signal can convey information on the specimen composition, topography, mass thickness, and crystallography. Backscattered electrons are quantified with the "backscattered electron coefficient," η , defined as [1]:

$$\eta = \frac{N_{BSE}}{N_{b}} \tag{2.8}$$

where N_B is the number of beam electrons that enter the specimen and N_{BSE} is the number of those electrons that subsequently emerge as backscattered electrons.

2. 5. Characteristic X-Rays

The process of generating characteristic X-rays is illustrated for a carbon atom in Figure 2.12. In the initial ground state, the carbon atom has two electrons in the K-shell bound to the nucleus of the atom with an "ionization energy" E_c and four electrons in the L-shell, two each in the L1 and the L2 subshells bound to the atom, with specific ionization energy. An incident energetic beam electron having initial kinetic energy $E_{in} > E_c$ can scatter inelastically with a K-shell atomic electron and cause its ejection from the atom, providing the beam electron transfers to the atomic electron kinetic energy at least equal to the ionization energy, which is the minimum energy necessary to promote the atomic electron out of the K-shell beyond the effective influence of the positive nuclear charge. The total kinetic energy transferred to the K-shell atomic electron can range up to half the energy of the incident electron. The outgoing beam electron thus suffers energy loss corresponding to the carbon K-shell ionization energy E_K plus whatever additional kinetic energy is imparted [1]:

$$E_{out} = E_{in} - E_k - E_{kin} \tag{2.9}$$

The ionized carbon atom is left with a vacancy in the K-shell which places it in a raised energy state that can be lowered through the transition of an electron from the L-shell to fill the K-vacancy.

The difference in energy between these shells must be expressed through one of two possible routes:

1. The left branch in Figure 2.12 involves the transfer of this K–L inter-shell transition energy difference to another L-shell electron, which is then ejected from the atom with a specific kinetic energy:

$$E_{kin} = E_k - E_L - E_L \tag{2.10}$$

This process leaves the atom with two L-shell vacancies for subsequent vacancy-filling transitions. This ejected electron is known as an "Auger electron," and measurement of its characteristic kinetic energy can identify the atom species of its origin, forming the physical basis for "Auger electron spectroscopy."

2. The right branch in Figure 2.12 involves the creation of an X-ray photon to carry off the inter-shell transition energy:

$$E_{v} = E_{k} - E_{L} \tag{2.11}$$

Because the energies of the atomic shells of an element are sharply defined, the shell difference is also a sharply defined quantity, so that the resulting X-ray photon has an energy that is characteristic of the particular atom species and the shells involved and is thus designated as a "characteristic X-ray." Characteristic X-rays are emitted uniformly in all directions over the full unit sphere with 4π steradians solid angle [1].

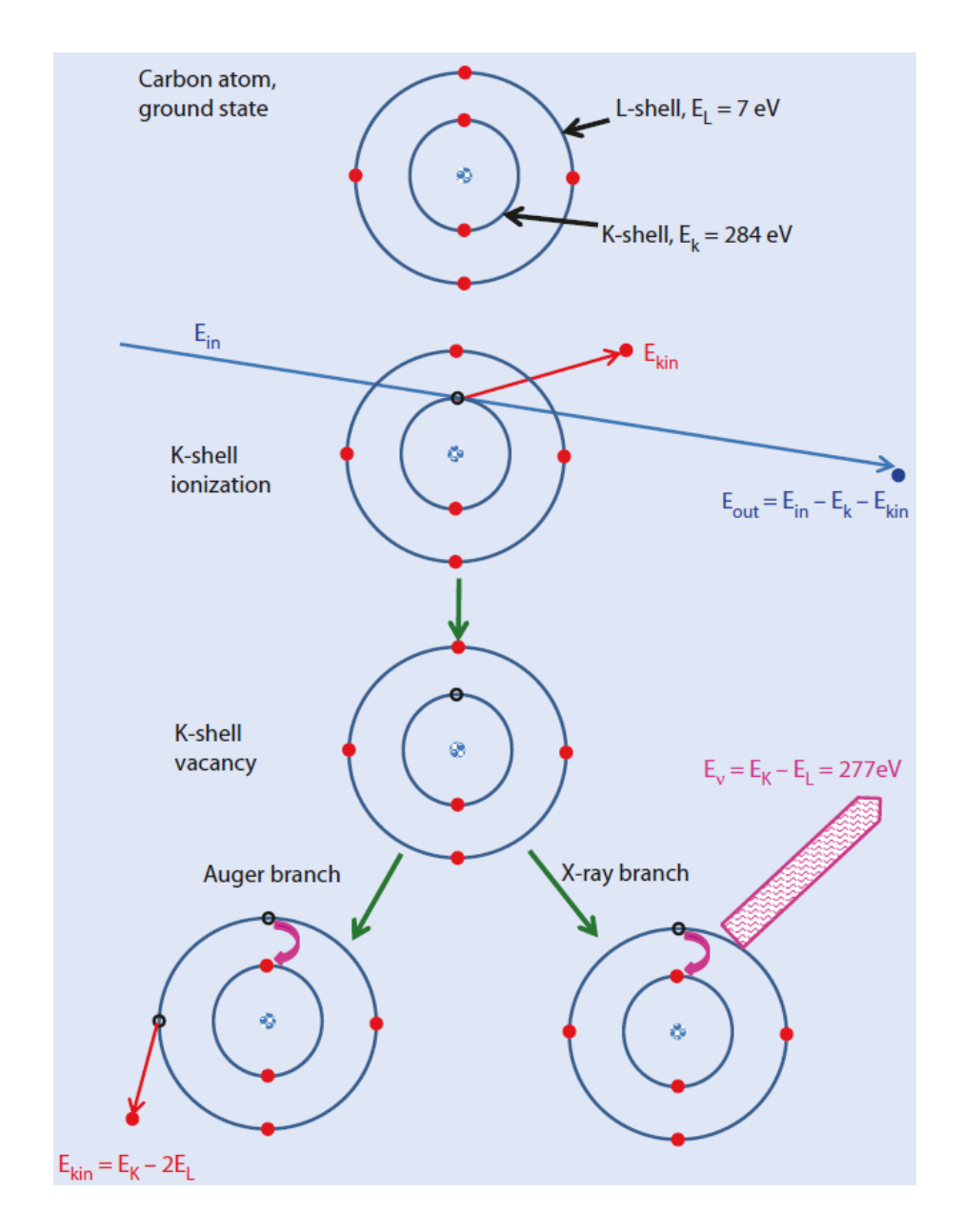


Figure 2-6 X-ray generation in Carbon from the interaction of high-energy electrons [1].

2. 5. 1 X-ray absorption

When traveling in a material, the generated X-rays are absorbed through three mechanisms: Compton scattering, Rayleigh scattering, and photoelectric effect [39]. Compton scattering is an inelastic scattering between an X-ray and an atom, resulting in the reduction of X-ray energy. It is negligible within the typical energy range of electron-induced X-ray microanalysis: 1–30 keV [1]. Rayleigh scattering is the interaction of the X-ray photon with the whole atom, resulting in the

deflection of the X-ray with no change in energy. Rayleigh scattering is important only for the absorption of collimated beams. The photoelectric effect is the most important absorption mechanism, in which the X-ray photon is completely absorbed with the ejection of an atomic electron.

The photoelectric effect happens only when the energy of the X-ray is greater than or equal to the binding energy of the atomic electron. The Beer-Lambert law describes the absorption of X-rays in a bulk sample, expressed as follows [37]:

$$I = I_0 \exp\left[-\left(\frac{\mu}{\rho}\right)\rho x\right] \tag{2.12}$$

where I is the X-ray intensity after absorption, I_0 is the incident X-ray intensity, ρx refers to the mass thickness of the specimen, which is the product of the density and thickness, μ/ρ is the mass absorption coefficient. Mass absorption coefficients of X-rays with different energies in different elements have been tabulated in units of cm^2/g [40, 41]. Figure 2.13 presents the variation of the mass absorption coefficient as a function of the X-ray photon energy in a Cu specimen. The mass absorption coefficient typically decreases as the X-ray photon energy increases. However, when the X-ray photon energy is just slightly higher than the excitation energy of a certain shell, the mass absorption coefficient increases abruptly, and this abrupt increase is called an absorption edge [49]. The absorption edges for K- and L-shells of Cu are marked in Figure 2.13 [42].

The mass absorption coefficient of a compound is calculated by summing up the weighted contributions of all the constituent elements according to their weight fractions, expressed as follows [1]:

$$\left(\frac{\mu}{\rho}\right)_{\text{comp}}^{i} = \sum_{j} \left(\frac{\mu}{\rho}\right)_{j}^{i} c_{j} \tag{2.13}$$

where $(\frac{\mu}{\rho})_{comp}^i$ is the mass absorption coefficient of X-ray i in a compound, $(\frac{\mu}{\rho})_j^i$ is the mass absorption coefficient of X-ray i in pure element j, and c_j is the weight fraction of element j in the compound.

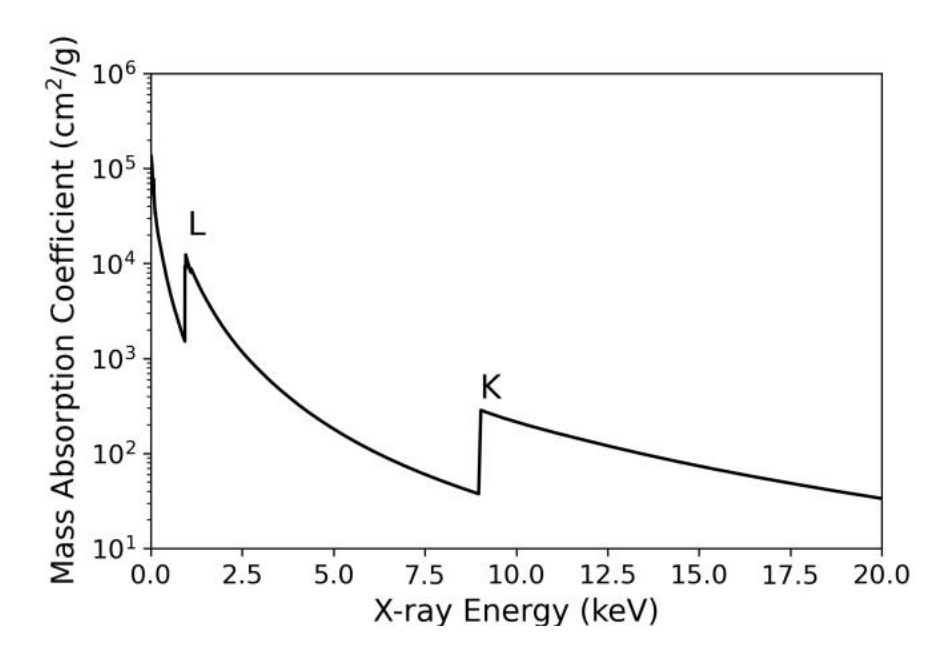


Figure 2-7 Mass absorption coefficient as a function of the X-ray photon energy for a Cu specimen from Ref. [42]

2. 5. 2 φ (ρz) curve

 $\varphi(\rho z)$ curve describes the distribution of characteristic X-ray production as a function of depth, defined as the ratio of X-ray intensity from a thin layer of a bulk specimen with a mass thickness of $\Delta(\rho z)$ located at the mass depth (ρz) , $I(\rho z)$ to that from a thin, unsupported film with the same thickness $I(\Delta \rho z)$. Thus, the total X-ray intensity for a thick sample I_{sample} is given by,

$$I_{\text{sample}} = I(\Delta \rho z) \int_0^\infty \phi(\rho z) d(\rho z)$$
 (2.14)

Figure 2.14 presents the generated (without absorption) and emitted (with absorption) $\phi(\rho z)$ curves for the aluminium (Al) K α line in a bulk Al sample at 15 keV. It is observed that the X-ray production in the first layer of the sample is greater than that in the thin unsupported film, i.e., $\phi(0)>1$. This is because some backscattered electrons travel back through the first layer to escape the sample, which produces more X-rays. As the increase of the depth, the curves first rise due to the increase of elastic scattering, which increases the travel lengths of the electrons in each thin layer. X-ray production starts to decrease with further increase in depth because of the decrease in the electron number and reduced energies of the electrons as a result of energy loss. Then the X-ray production continuously decreases to zero [1].

 $\varphi(\rho z)$ curves can be obtained experimentally using the tracer method by Casting and Descamps [43] or the wedge technique by Schmitz [44]. Also, a lot of analytical models have been proposed to calculate $\varphi(\rho z)$ curves, including thin film model (1966) [45], square model (1974) [46], the quadrilateral model (1984) [47], Gaussian model [48-50] parabolic (PAP) model [51, 52], and exponential (XPP) model [53, 54].

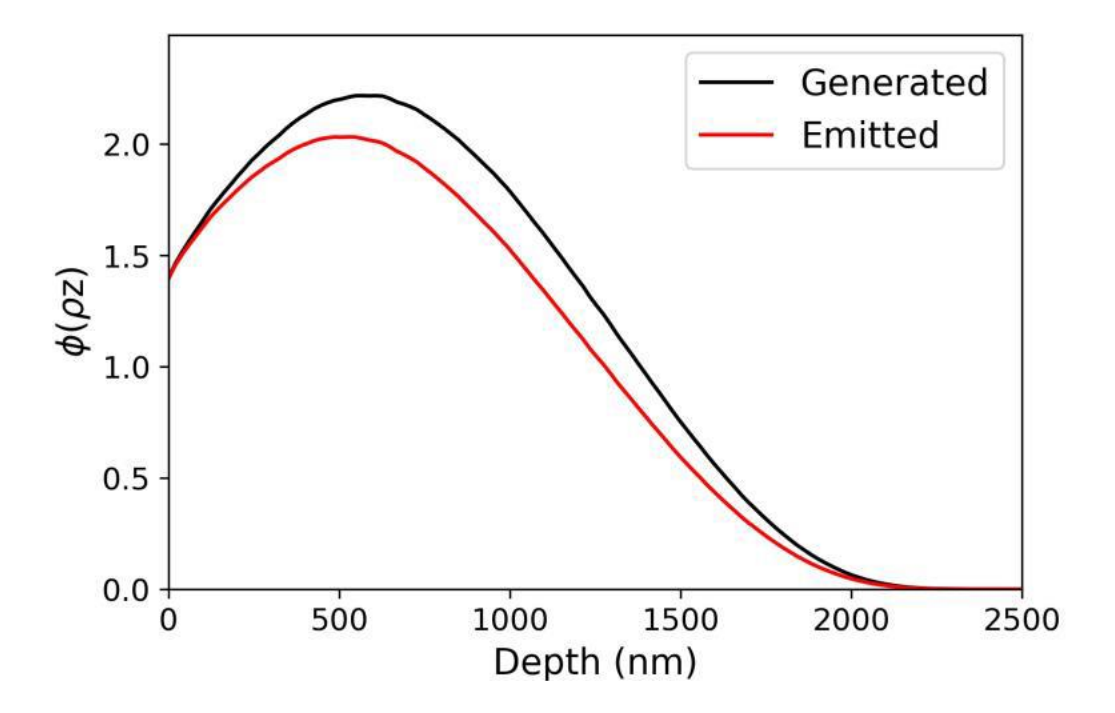


Figure 2-8 Generated and emitted $\phi(\rho z)$ curves for the Al K α line in pure Al at 15 keV, simulated using MC X-ray [55].

2. 6. Quantitative x-ray microanalysis of flat samples

Quantitative x-ray microanalysis method was first established to analyze specimens having homogeneous composition and flat surfaces [56]. Following the basic principles of electron-induced X-ray emission, two questions are answered in this section: how X-rays are detected and how to calculate the composition of an unknown specimen with the detected spectrum.

2. 6. 1 X-ray detection

Once the generated X-rays get out of the sample, some of them are detected by the X-ray detector, through which their energies or wavelengths and counts are measured. Two systems are available for such analysis: Wavelength-dispersive spectroscopy (WDS) and EDS.

WDS selects the X-rays to be counted according to their wavelengths using Bragg diffraction [55]. Bragg's law gives the n order reflection condition of an incident X-ray with a wavelength λ_x to be reflected by an analyzing crystal with lattice-plane spacing d at a certain glancing angle θ , expressed as follows:

$$n\lambda_{x} = 2d\sin\theta \tag{2.15}$$

The first order reflection (n = 1) is the most intense reflection and normally used in wavelength dispersive analysis. A crystal spectrometer can only detect X-rays of a certain wavelength at a time. A range of wavelengths can be achieved by rotating the crystal and detector at the same time, but the range is still limited by the range of rotating angle (θ typically ranges from 15° to 70°). To measure the full X-ray range, different crystals are needed. Normally, two or more WDS are equipped to cover the full X-ray range at a time. X-rays are detected with a gas-filled proportional counter through which the mean amplitude of the output pulse is proportional to the energy of the X-ray photon. For commercial EDS systems, the energy resolution of a WDS is about 10 eV; however, some WDS analyzers can produce an energy resolution below 1 eV [57].

EDS, on the contrary, detects X-rays with different energies simultaneously using a semiconductor (normally Si). X-rays are first absorbed in the semiconductor through the photoelectric effect, which results in the generation of several electron-hole pairs with a mean energy ϵ_{e-h} (3.8 eV for Si). The number of electron-hole pairs N_{e-h} is proportional to the X-ray photon energy, E_X :

$$N_{e-h} = \frac{E_X}{\epsilon_{e-h}} \tag{2.16}$$

The free electrons and positively charged holes then move to two sides of the crystal as a result of a strong electric field. The current is measured by a preamplifier to determine the energy of the X-ray photon. Two kinds of EDS detectors are widely used: the lithium-drifted silicon (Si(Li)) detector [58] and silicon drift detector (SDD) [59, 60]. The latter detector is more advanced and has a higher count rate than the former. The energy resolution of an EDS is mainly limited by the noise amplitude of the preamplifier and the peak broadening because the number of generated electron-hole pairs yields a statistical fluctuation.

Since EDS can detect X-rays with varying energies simultaneously, it takes less time for EDS to measure the full X-ray spectrum than WDS. People, therefore, prefer to use EDS for qualitative analysis. On the other hand, the energy resolution of WDS is around ten times better than EDS. WDS also shows advantages in count rate and peak to background ratio. Thus, WDS is more likely to be used for trace elements quantitative analysis. However, the difference between EDS and WDS is becoming smaller. Recently, research has been conducted to show that EDS measurement can get similar precision and accuracy as WDS for the analyses of major and minor elements [61, 62].

2. 6. 2 Traditional quantification approaches

Quantitative X-ray microanalysis calculates the composition of an unknown sample using the measured characteristic X-ray intensities. Two quantification methods are widely applied to bulk materials: the k-ratio method and the f-ratio method.

2. 6. 2. 1 k-ratio method

A k-ratio is the ratio of a pair of characteristic X-ray line intensities, I, measured under similar experimental conditions for the unknown and standard [1, 63]:

$$k = \frac{I_i}{I_{(i)}} \tag{2.17}$$

where I_i and $I_{(i)}$ are the intensity of the unknown and standard sample, respectively. The measured intensities can be associated with a single characteristic X-ray line or associated with a family of characteristic X-ray lines. Both the numerator and the denominator of the k-ratio must be measured under similar, well-controlled instrument conditions. From a set of k-ratios, it can be estimated the unknown material composition. In many cases, to a good approximation:

$$C_i \sim kC_{(i)} = \frac{I_i}{I_{(i)}C_{(i)}}$$
 (2.18)

where C_i and $C_{(i)}$ are the mass fraction of element i in the unknown and standard, respectively, and k is the k-ratio measured for element i.

All k-ratio measurements must have associated uncertainty estimates. For example, the primary source of uncertainty in a k-ratio measurement is typically count statistics although instrumental

instability also can contribute. Then, although the k-ratio is often a good first approximation to the composition. However, it should be better. The physics of the generation and absorption of X-rays is sufficiently well understood that we can use physical models to compensate for non-ideal characteristics of the measurement process. These corrections are called matrix corrections as they compensate for differences in the matrix between the standard material and the unknown material. Matrix correction procedures are typically divided into two classes $\varphi(pz)$ and ZAF-type corrections. The distinction is primarily how the calculation is divided into independent subcalculations. In a ZAF-type algorithm, the corrections for differences in mean atomic number (the Z term), X-ray absorption (the A term) and secondary fluorescence (the F term) are calculated separately. $\varphi(\rho z)$ matrix correction algorithms combine the Z and A terms into a single calculation. The distinction between $\varphi(\rho z)$ and ZAF is irrelevant for this discussion so the matrix correction will be described by the generic ZAF where this expression refers to the matrix correction associated with a material with composition [1]. The proposed method established to analyze specimens having homogeneous composition and **flat surfaces.** But as mentioned before, the fracture surfaces are not flat. Therefore, these methods do not apply to all actual examples and a great deal of attention is still being given to those examples where the flat homogeneous methods cannot be used.

2. 6. 2. 2 f-ratio method

Another emerging quantification approach is the f-ratio method [64-66]. This method is similar to the Cliff and Lorimer ratio method [67], which connects the ratio of the characteristic X-ray intensities of two constitute elements A and B of the specimen to the ratio of their element concentrations as follows:

$$\frac{c_{A}}{c_{B}} = K_{AB} \frac{I_{A}}{I_{B}} \tag{2.19}$$

where K_{AB} is the Cliff and Lorimer K factor, which can be calculated experimentally using a standard. Since the characteristic X-ray intensities are obtained from the same spectrum, the identical analysis condition that is required for the k-ratio method is not necessary. The Cliff and Lorimer method is typically applied to thin films, while the f-ratio method can be applied to bulk specimens.

In a binary system with element A and B, the f-ratio is defined as [68]:

$$f_{A} = \frac{I_{A}}{I_{A+}I_{B}} \tag{2.20}$$

where I_A and I_B are characteristic X-ray intensities of elements A and B, respectively. The benefit of the f-ratio method is that even when the concentration of element B is low and I_B is close to 0, the f-ratio is still relatively stable [69]. Normally, a calibration curve of the f-ratio versus the element concentration is first computed using either Monte Carlo simulation or analytical models, and the measured f-ratio is used to determine the concentration in the unknown sample through interpolation. The f-ratio method has been successfully applied to binary [64, 66] and multi-element systems [70].

For the mentioned quantification methods and other methods that are currently available, one identical restriction is that they can only deal with homogeneous samples or samples that are homogeneous within the interaction volume.

2. 7. Monte Carlo Modeling

For materials with complex geometries like multilayer materials and particles inside matrices, the traditional quantitative X-ray microanalysis methods that have been mentioned in section 2.2.2 are not applicable. The Monte Carlo method is a useful tool to simulate electron-solid interaction and estimate X-ray emissions and is available for materials with arbitrary geometries [39].

2. 7. 1 Monte Carlo method

The Monte Carlo model uses random numbers to forecast the result of an event [71]. In electron-induced X-ray microanalysis, it is used to compute the travel direction and travel distance after each elastic collision of the incident electron with the solid to simulate the whole electron trajectory. Then, the X-ray emission in each electron trajectory segment is calculated to obtain the full X-ray spectrum. In this section, the single scattering model which is one of the most popular models of simulating electron-solid interaction using the Monte Carlo method will be briefly introduced. In Ref. [71-74] a more detailed description of the Monte Carlo method and other models can be found.

In the single scattering model, it is assumed that only elastic scattering events control the trajectory of a given electron, and the procedure of how an electron loses its energy is continuous [71]. Figure 2.15 shows the geometry used to simulate the electron trajectory using the single scattering model [75].

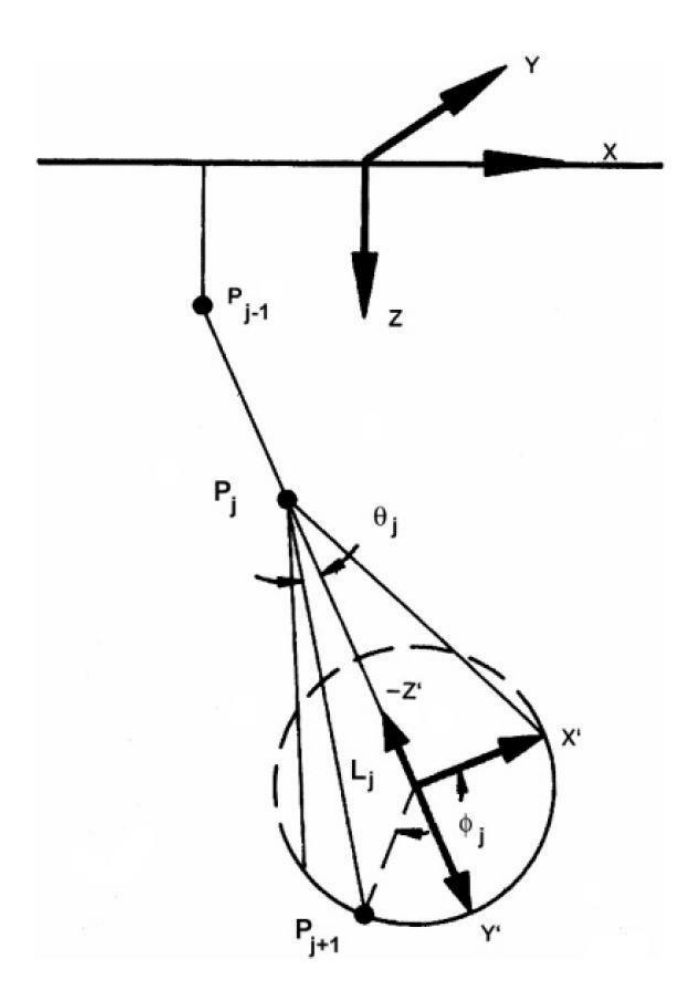


Figure 2-9 Geometry used to simulate the trajectory of an electron using the single scattering model from Ref. [75].

An electron travels to point P_j after undergoing an elastic scattering at point P_{j-1} . To determine the position of the next scattering point P_{j+1} , the travel distance L_j and travel direction are required. Subsequently it is assumed that only elastic scattering events are considered to determine the electron trajectory, the distance is related to the elastic mean free path, defined as follows:

$$\lambda = \frac{A}{N_0 \rho \sigma_E} \tag{2.21}$$

where A is the atomic weight of the target, N_0 is Avogadro's number, ρ is the density of the target, and σ_E is the elastic cross-section. The travel distance Lj is given by,

$$L_{j} = -\lambda \ln (RND) \tag{2.22}$$

where RND is a random number that is uniformly distributed between 0 and 1. The travel direction depends on the polar angle θ and azimuthal angle ϕ . When using the partial Rutherford cross-section, they are expressed as [75]:

$$\cos(\theta) = 1 - \frac{2\alpha RND}{1 + \alpha - RND} \tag{2.23}$$

$$\phi = 2\pi . RND \tag{2.24}$$

where α is the screening parameter. With both the travel distance and direction known, the coordinates of point Pj+1 can be calculated. Notice that RND in equation (2.23) to (2.24) are different and generated randomly each time before being used. The energy loss during the travel from Pj to Pj+1 is determined by the continuous slowing down approximation using the following equation:

$$E_{j+1} = E_j + \frac{dE}{dS} L_j \tag{2.25}$$

where dE/dS is the stopping power, which is typically calculated using Bethe's model [38] or its modification [76]. The electron trajectory is simulated step by step until the electron energy is small enough or the electron escapes out of the specimen. Although the same equations are used for all the electrons, the trajectories of the electrons vary because of the use of random numbers in each step. Therefore, with a great number

of simulated electrons, the Monte Carlo method can simulate the actual electron-solid interaction in experiments. Figure 2.16 shows the electron trajectories of 200 electrons in carbon (C) at 10 keV using a Monte Carlo software program CASINO2 [77]. Red curves represent the trajectories of backscattered electrons.

The X-ray production (both characteristic and bremsstrahlung) is calculated for each segment of the electron trajectories and summed up to obtain the total X-ray intensity. The characteristic X-ray intensity in a certain segment j is calculated using the following equation [71]:

$$I_{cha,j} = \frac{\sigma N_A \rho \omega L_j}{A} \tag{2.26}$$

where σ is the ionization cross-section for the emission of characteristic X-rays, ω is the fluorescence yield, and Lj is the segment length. The bremsstrahlung X-ray intensity is calculated as follows:

$$I_{brem,j} = \frac{QN_A \rho L_j}{A} \tag{2.27}$$

where *Q* is the ionization cross-section for the emission of bremsstrahlung X-rays. An X-ray spectrum of a Si substrate with a 200 nm chromium (Cr) coating simulated using MC X-ray [78] at 15 keV is presented in Figure 2.17a.

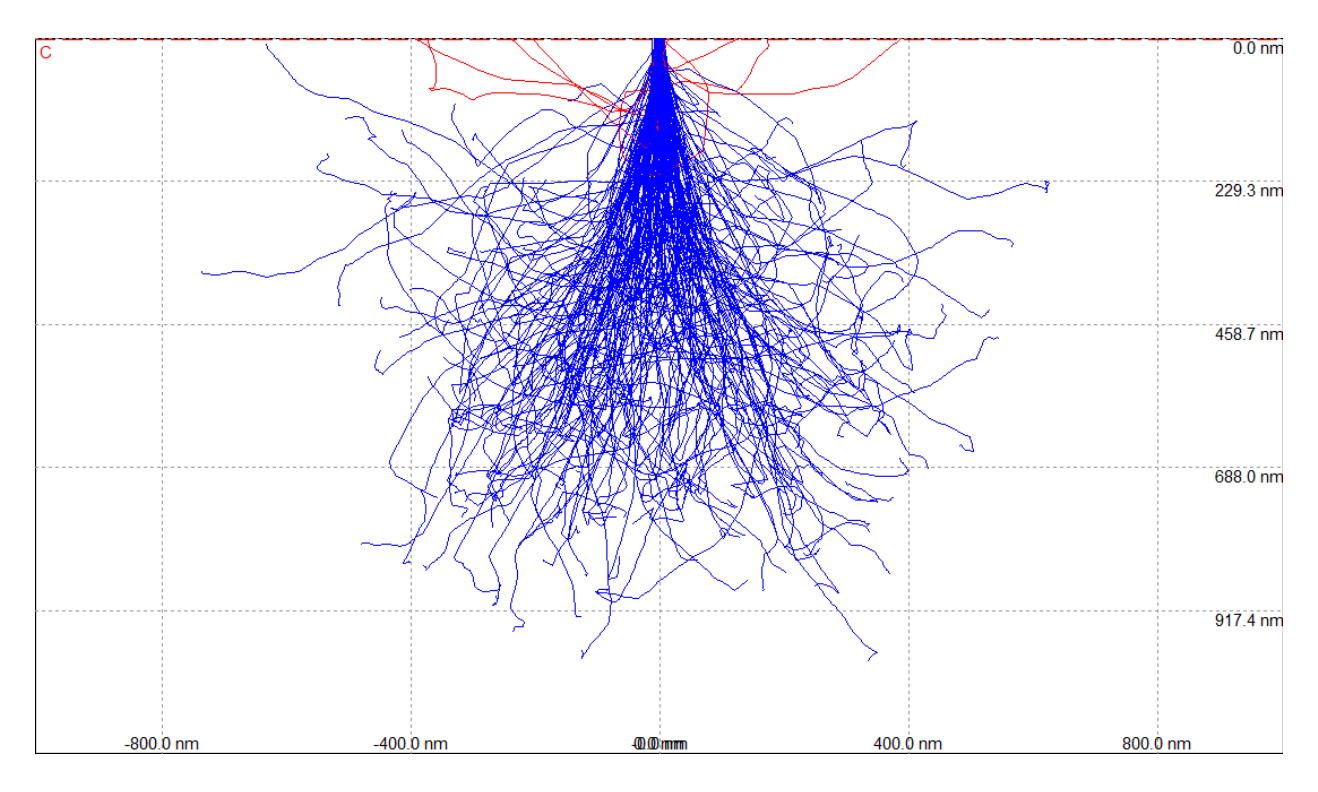


Figure 2-10 Electron trajectories of 200 electrons at 10 keV in carbon using CASINO2 [77].

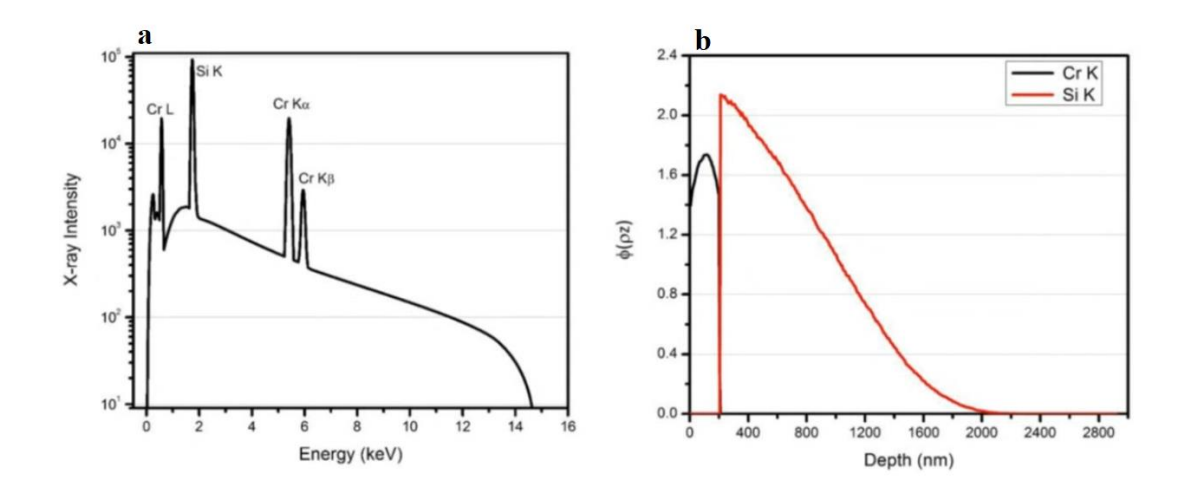


Figure 2-11 a) Simulated X-ray spectrum and b) φ(ρz) curves for a Si substrate with a 200 nm Cr coating at 15 keV using MC X-ray [78].

Monte Carlo simulation has also been widely used in studying the spatial distribution of electrons and X-rays in bulk samples [79-82]. Good agreements in $\varphi(\rho z)$ curves between the Monte Carlo simulation and experiments were found [82]. Figure 2.17b presents the generated depth distribution curves for both the Si K line and Cr K line for a Si substrate with a 200 nm Cr coating, in which the boundary at a depth of 200 nm is clearly shown.

Monte Carlo simulations are also applicable to heterogeneous materials, for example, multilayer materials [83, 84], particles [85], and grain boundaries [86].

2. 7. 2 Monte Carlo program

In this section, two commonly used Monte Carlo programs for X-ray microanalysis are briefly introduced: MC X-ray [78], and DTSA-II [87]. Gauvin's group developed MC X-ray [78] as an extension of CASINO [77, 88] and Win X-ray [75]. It computes the full X-ray spectrum for materials with various types of structures, which can be a combination or subtraction of several basic structures: box, sphere, and cylinder. It uses the single scattering model and continuous slowing down model and allows users to choose different physical models. The graphical user interface (GUI) of MC X-ray makes it easy to use. Furthermore, MC X-ray can also output the spatial distribution of the emitted X-rays. Recently, it has been integrated into Dragonfly, a software platform for image analysis, to provide more flexibility in simulated specimens and improve simulation efficiency [89].

DTSA-II [87] is an important tool to visualize, compare, manipulate, and quantify the measured spectra, and also provides a fast simulation of X-ray spectrum for arbitrary complex samples. Similar to MC X-ray, it uses the continuous slowing down approximation for calculating X-ray emission. One advantage of DTSA-II is that it includes the calculation of secondary fluorescence, which improves the accuracy of the simulated X-ray spectrum [90].

2. 8. 3D Reconstruction methods

In computer vision and computer graphics, 3D reconstruction is the process of capturing the shape and appearance of real objects. Using 3D reconstruction, one can determine any object's 3D profile, as well as knowing the 3D coordinate of any point on the profile. 3D reconstruction methods are classified into passive and active. Passive methods do not involve interaction with the object, whereas active methods use contact or a projection of some form of energy onto the object [16]. Active methods reconstruct the 3D profile by numerical approximation approach and build the object in scenario based on model. Passive methods of 3D reconstruction do not interfere with the reconstructed object; they only use a sensor to measure the radiance reflected or emitted by the object's surface to infer its 3D structure through image understanding [17].

2. 8. 1 3D reconstruction from multiple images

3D reconstruction from multiple images is the creation of 3D models from a set of images. It is the reverse process of obtaining 2D images from 3D scenes. The essence of an image is a projection from a 3D scene onto a 2D plane, during which process the depth is lost. The 3D point corresponding to a specific image point is constrained to be on the line of sight. From a single image, it is impossible to determine which point on this line corresponds to the image point. If two images are available, then the position of a 3D point can be found as the intersection of the two projection rays. This process is referred to as triangulation. The key for this process is the relations between multiple views, which convey the information that corresponding sets of points must contain some structure and that this structure is related to the poses and the calibration of the camera [18, 19] Suppose there are two images, taken from different viewpoints. Such setting is referred to as stereo. The situation is illustrated in Figure 2-4. The principle behind stereo-based 3D reconstruction is simple: given the two projections of the same point onto the two images, its 3D position is found as the intersection of the two projection rays. Repeating such process for

several points produces the 3D shape and formation of the objects in the scene. Note that this construction referred to as triangulation. Moreover, to perform this triangulation process, one needs ways of solving the correspondence problem, i.e. finding the point in the second image that corresponds to a specific point in the first image, or vice versa [20]. To reconstruct a 3D model from multiple images, proper types of features should be chosen, and appropriate formulations should be derived based on the feature characteristics for the parameter estimation. Commonly used geometric features in motion and structure problem include points, straight lines, and line segments [21-23]. There have been remarkable research results on the topic of 3D model reconstruction using line segments [24, 25]. Though some methods can automatically extract features, an extraordinary number of features are required for the optimization process. Additionally, features which are not of interest are difficult to be separated in the processing. As a result, the final 3D structure must be modified severely to exclude outliers and unnecessary features [20].

Since the 3D reconstruction of general surfaces plays an important role in many branches; for example, the morphological analysis of fracture surfaces reveals information on mechanical properties of natural or construction materials. Therefore, the 3D rebuilding of fracture surfaces must be investigated more in details. There are more techniques capable of producing 3D replicas of solid surfaces. But first, the algorithms which are used in those methods must be identified. The Structure from Motion (SfM) algorithms and the Multi View Stereo (MVS) algorithms are the most famous algorithms in this field. The prior one is used to generate sparse 3D reconstructions and the latter is used to produced dense 3D reconstructions [26]. Because the explanation of these two algorithms is beyond the scope of this project, details are discarded. The reader can refer to the source [27] for further information.

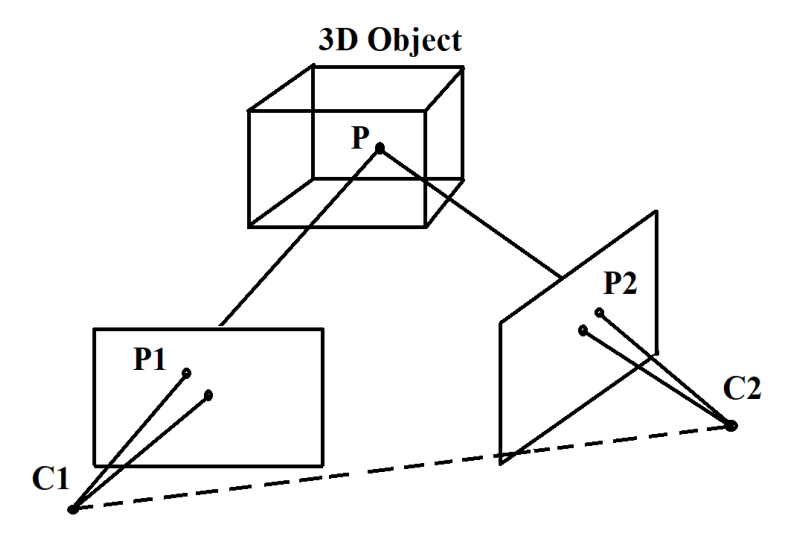


Figure 2-12 Illustration of the basic principles of shape-from-stereo (stereo reconstruction).

As part of the research into previous work, a survey of the existing open-source software that has been developed by various researchers was conducted. Based on this research, it appears that the majority of the current toolkits are based on the Bundler package, a Structure from Motion system for unordered image collections developed by Snavely [26]. Bundler generates a sparse 3D reconstruction of the scene. For dense 3D reconstruction, the preferred approach seems to be to use the multi view stereo packages (CMVS and PMVS software), developed by Furukawa [27]. Bundler, CMVS and PMVS are all command line tools. As a result, a number of other projects have developed integrated toolkits and visualization packages based on these tools. Of note are the following, which were evaluated as part of this project:

- OSM Bundler a project to integrate Bundler, CMVS and PMVS into Open Street Map
- Python Photogrammetry Toolbox (PPT) a project to integrate Bundler, CMVS and PMVS
 into an open-source photogrammetry toolbox by the archeological community
- Visual SFM a highly optimized and well-integrated implementation of Bundler, PMVS and CMVS. Of note are the inclusion of a GPU based SIFT algorithm (SiftGPU) and a multi-core implementation of the Bundle Adjustment algorithm. The use of these packages allows Visual SFM to perform incremental Structure from Motion in near linear time.

Several packages are available for visualization of point clouds, notably MeshLab, Cloud Compare and the Point Cloud Library (PCL) which integrates nicely with OpenCV.

2. 8. 2 Secondary electron (SE) or backscattered electron (BSE) signals for 3D reconstruction

In the case of using MVS method, the pipeline strongly requires image orientation estimation based on detected and matched feature points in the 2D SEM image set [28]. Therefore, obtaining 2D images with fine features at different views would be the main objective in the 3D digital reconstruction technique. At the beginning, one of our challenges was choosing the type of signals for imaging. Secondary electrons (SE) or Backscattered electrons (BSE)?! Table 2-1 shows the features of the two types of signals. By taking into account that rotation and tilting are two main factors in 3D digital reconstruction [29], and the presence of a non-flat surface differs significantly with the type, solid angle, and take-off angle of the detector used to collect the signal [1]. Notably that the location of the detector could play a significant role for obtaining more signals from rough surfaces. Therefore, backscattered electrons are most efficiently and selectively collected with a 4-quadrant backscattered electron (4Q-BSE) detector directly located on top of the sample. Based on the summarized information in Table 1, and the fact that there are more features of each 2D images, the increased accuracy and reliability to the 3D SEM surface reconstruction, it was decided to utilize the 4-quadrants backscattered electron detector to collect BSE signals for 3D digital rebuilding. The reasons for this decision are summarized as follows: (i) Backscattered electrons provides high quality topographical information of the surface, (ii) Using the backscattered electrons saves time and cost, (iii) 3D reconstruction process and post processing via BSE images are much easier than using SE images, and (iv) The most important reason for choosing BSE images is that in this situation four images are sufficient for 3D digital reconstruction to be accessed with only one scan.

Table 2-1 Comparison between SE and BSE in imaging [1].

Backscattered Electrons (BSE)

Secondary Electrons (SE)

Secondary Electrons (SE)	Duchiseutter en Erecti ons (ESE)
The small escape depth	Dependence on take-off angles
Dependence on the local tilt	Dependence on the local tilt
Small change in SE with beam energy in	Small change in BSE with beam energy in
the range 1 to 50 eV	the range 5 to 50 kV
Affected by local magnetic and electrostatic fields	Stronger variation for light element

2. 8. 3 3D rebuilding of fracture surfaces

In 2002, Pouchou et al. [13] used multiple images technique to achieve (MVS algorithm) 3D images from SEM images. They used an Everhart-Thornley detector, but conventional secondary electron (SE) images are submitted to shadowing effects, which give the impression that they contain a lot of topographical information. They are sensitive to the local orientation of the surface with respect to detector (this my help to match image features) but there gives almost no information about deep cavities or regions hidden behind steep walls. Therefore, they cannot be useful for 3D reconstruction. However, SE-IL images (achieved by In lens detector) seem to be more faded since they exhibit mainly a contrast corresponding to contours. But they are more sensitive to the surface and have a better resolution than the previous ones, so that they are loading a lot of fine information that may help in the correlation procedure, mainly at high magnification. However, there are two problems with SE-IL signals; first, because SE-IL signals are sensitivite to surface potential, so that it should be avoided from charging effects; Secondly, the sensitivity of detection is not uniform over the whole field at low magnification. By comparing non-flat profiles (see Figures 2.5), their technique had very satisfactory results between 3D reconstruction of SE-IL images in comparison with atomic force microscopy (AFM) results.

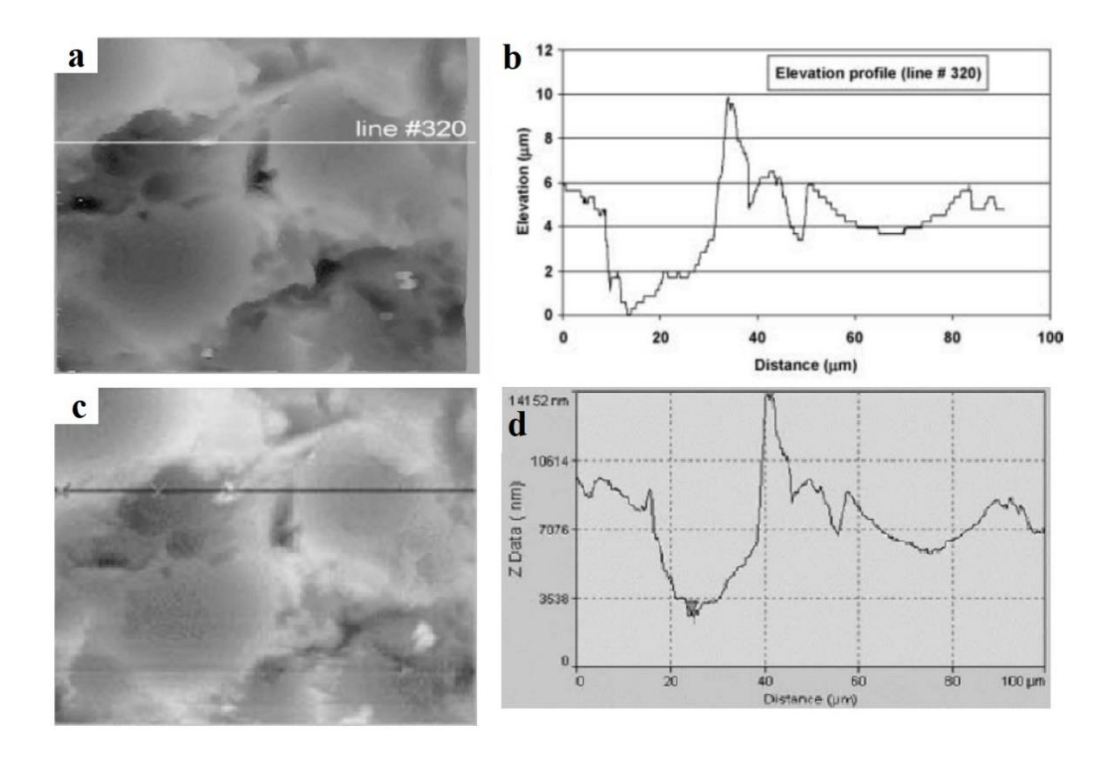


Figure 2-13 a) Non-flat surface of aluminum; b) Non-flat profile after 3D reconstruction using SE-IL images; c) Non-flat surface of aluminum; and d) Non-flat profile obtained by AFM [13].

In 2005, Raspanti et al. [30] presented a high-resolution 3D reconstruction method based on the SfM algorithm. Their method had some steps: first, reading a stereo-pair of SEM micrographs; then, selecting a number of prominent key features on the first picture; then, identifying the same features in the second picture, after that, computing the height of all the key points thus identified in both micrographs; then, connecting the points so obtained to reconstruct the spatial shape of the original specimen; finally, projecting the original picture back on the computed surface. Their results showed that the surface reconstructed by SEM micrographs, has a good resemblance to the specimen it came from by comparing with Atomic Force Microscopy (AFM). They used the second image to compute the relief of the first one, which can then be remapped exactly onto the reconstructed surface.

On the other hand, most authors [13, 30, 31] used two images symmetrically tilted by plus or minus a given angle to reconstruct a zero-tilt surface, which corresponds to neither of the original images. To obtain an objective evaluation of the correspondence, they showed three non-flat profiles along an arbitrary section were taken from AFM images (Figure 2.6) and from the equivalent SEM surfaces. Although, Figure 2.6 shows that there is a good similarity between 3D

reconstruction method comparing with AFM in some cases, but in some others (Figure 2.6-middle one) there is not appropriate fitness (a lot of noises) between two profiles. Moreover, they did not provide any correction regarding errors, which is obvious in this type of modeling.

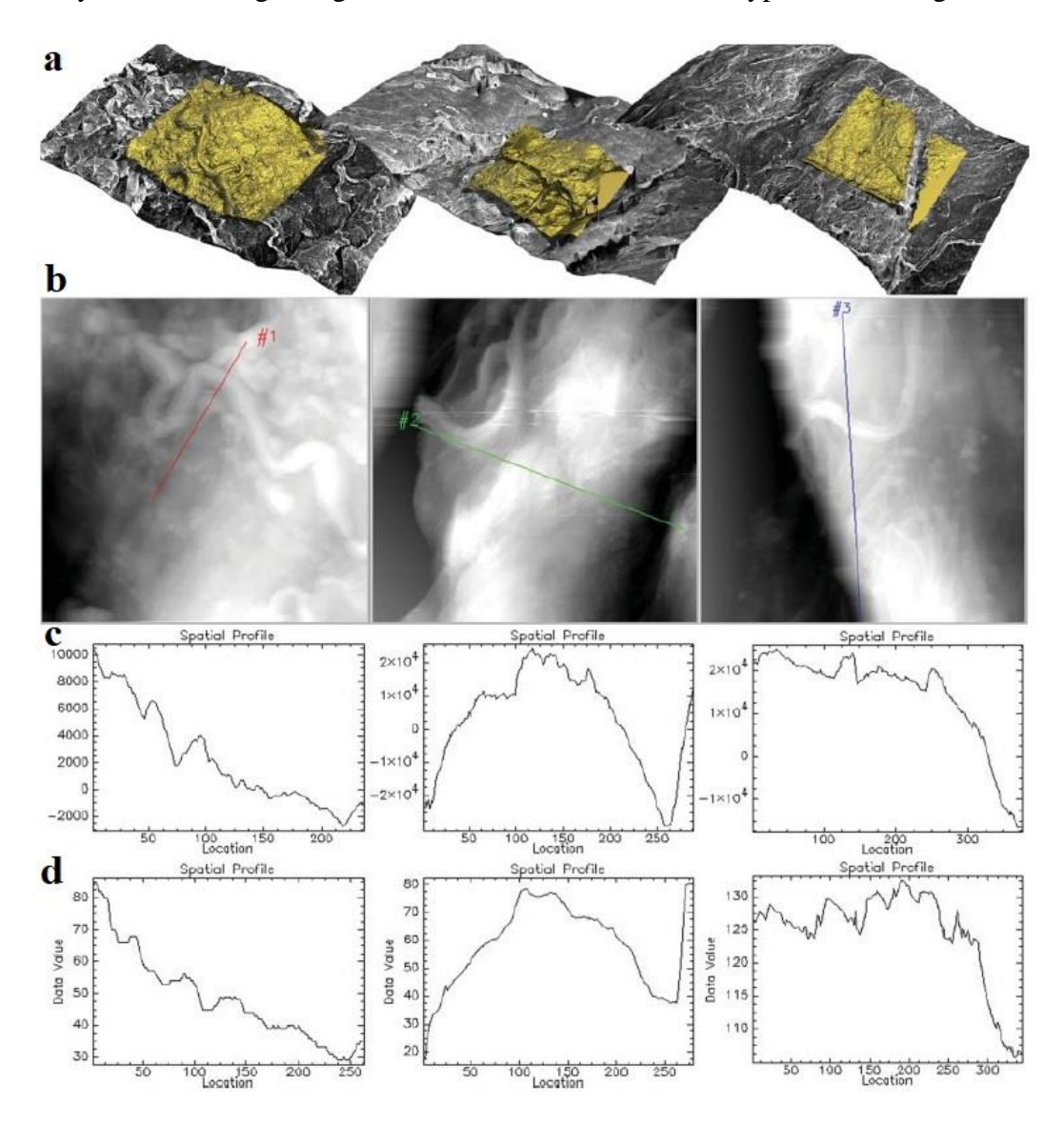


Figure 2-14 a) 3D reconstructions of the datasets with their corresponding AFM height fields (yellow); b) three profiles have been traced on the AFM micrographs; c) the altimetric traces corresponding to each profile; and d) the altimetric traces of the analogous profiles on the SEM reconstructions [30].

In 2007, Samak et al. [32] used an SfM algorithm to reconstruct 3D microstructure surfaces from SEM images. Their method was based on Computer Aided Geometric Design (CAGD) techniques [33], including stereo photogrammetry [34, 35], mesh reconstruction, texture mapping and segmentation. Based on their method, 3D points were produced by a stereo photogrammetry

process. After that, a mesh was created from the 3D points as a 3D Computer Aided Design (CAD) model for visualization and analysis. Then, the 3D mesh was reconstructed, and the microstructure surface's source image mapped onto the 3D mesh, thus combining the 3D representation with texture data. Their method went by these steps:

- 1. Pre-defining initial photography parameters.
- 2. Matching the images and computing the 3D matched points from the two stereo images.
- 3. Creating the macrostructure surface by meshing the resulting 3D points.
- 4. Defining the microstructure surface by mapping a texture on the resulting 3D mesh.
- 5. Segmenting the images to differentiate between different material-deformed regions.
- 6. Applying analyses and mechanical simulations, such as fracture analysis, by utilizing the 3D surface.

They used three different samples (ceramic material; synthetic earth magma; and syntactic foam) to analyze fracture behavior from the resulting 3D textured meshes. Each was tested at different SEM magnifications and different tilt angles. The results are demonstrated in Figure 2.7. Although they claimed that the samples produced by their method had realistic surfaces despite their different texture characteristics. However, there is a big problem with their technique; based on their claim, the SEM magnification does not improve computation results [39]. However, changing the magnification affect resolution and then the number of details which are appeared in the SEM images (2D) [1, 5] and as a result, it can affect the quality of 3D rebuilding.

In 2011, Carli et al. [29] performed a theoretical uncertainty evaluation of stereo-pairs technique for 3D SEM surface reconstruction. By taking to account of rotation and tilting as two main factors in 3D reconstruction of SEM images, they concluded that for the case of rotations, the largest uncertainty contribution is due to the reproducibility of the rotational angle, followed by the bias of the pixel size. In addition, for the case of tilting, the largest uncertainty contribution is due to the bias of the pixel size, followed by the reproducibility of the tilt angle.

In 2015, Bakic et al. [36] used 3D digital optical microscope in their study to image objects with non-flat surface of (achieved by Charpy test). A 3D profile of fracture surfaces of specimen is shown in Figure 2.8. Based on their results, by using 3D image of the fracture surfaces, it is possible to get much more information regarding fracture surface in comparison with 2D images. The analyses of the 3D profile of fracture surfaces provided background for establishment of

geometrical characteristics, as a measure of the material ductility change and could be useful tool in fractography analysis. Based on the results, by using of 3D images, they could get three new geometric characteristics; a) The angle of inclination of the specimen edge, α ; b) The maximum height of the specimen edge, h; c) The distance between specimen edge and the deepest crater (see Figure 2.9c). However, unfortunately they did not report any information about the 3D reconstruction technique which was used.

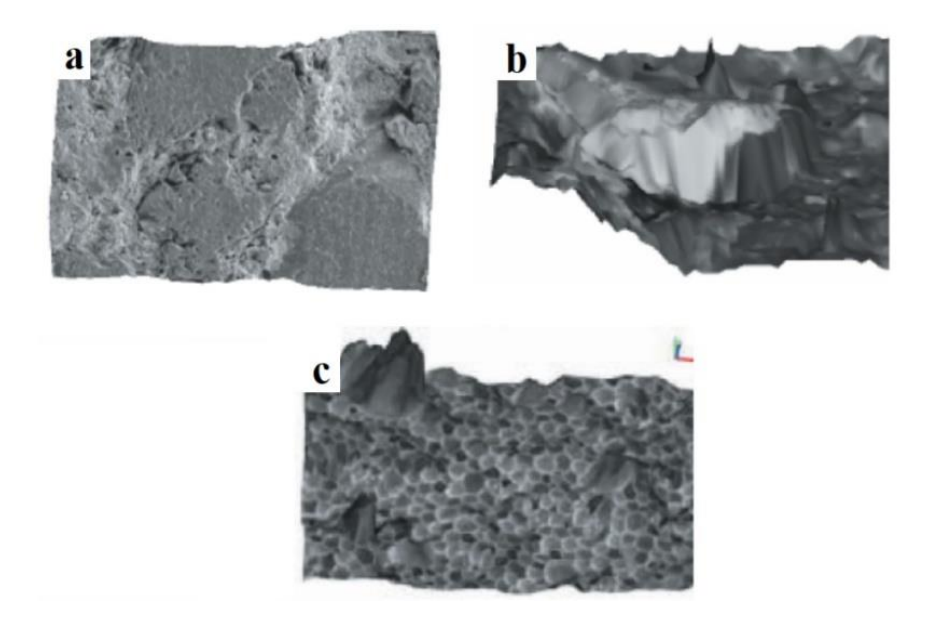


Figure 2-15 Reconstructed surfaces of: (a) ceramic material; (b) synthesis earth magma; and (c) syntactic foam [36].

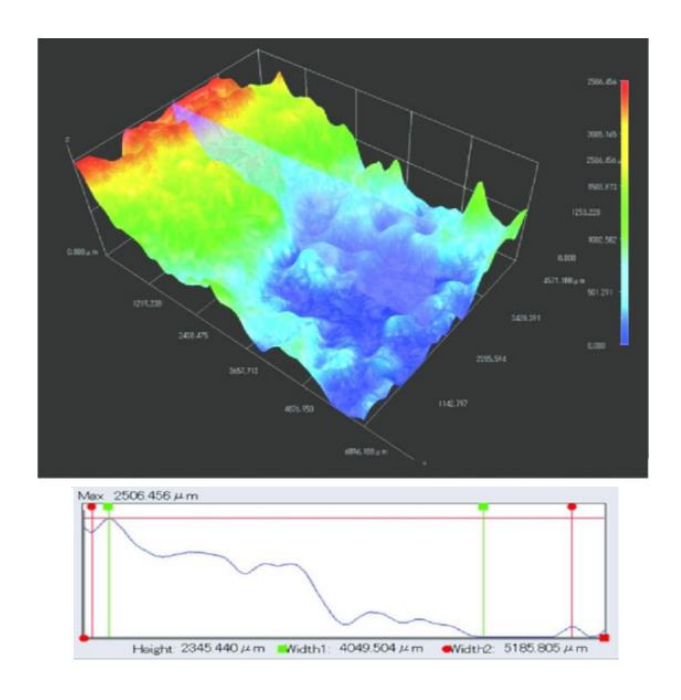
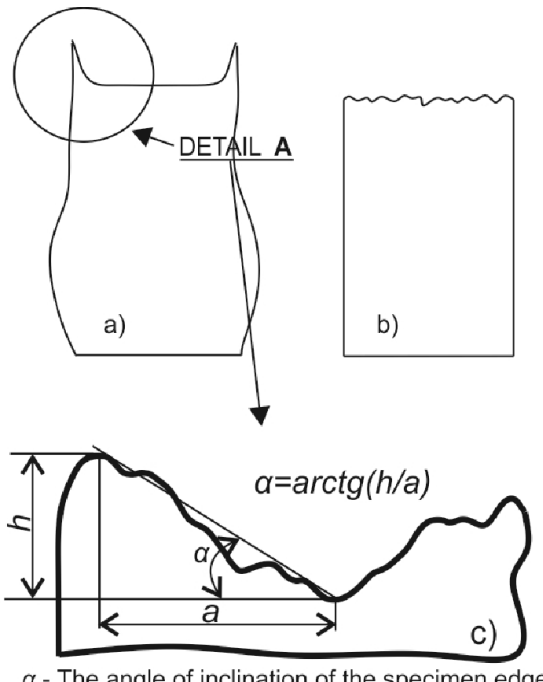


Figure 2-16 The 3D profile of fracture surface of Charpy specimen 3 (60°C) [36].



- α The angle of inclination of the specimen edge
- h The maximum height of the specimen edge
- a Distance between specimen edge and the deepest crater

Figure 2-17 Geometrical characteristics of fracture surface; a) Typical view of the ductile broken Charpy V-notch specimen; b) Typical view of the brittle broken Charpy V-notch specimen; and c) Schematic view of geometrical characteristics [36].

2. 9. Quantitative x-ray microanalysis of rough surfaces

Earlier efforts that have been made to compute complete X-ray spectra generally fall into two categories, closed form analytical models and Monte Carlo models [75]. There are some uncertainties in either the correctness of the physical models or the parameters used in both approaches. Therefore, they must be refined with the use of some modifiable parameters to attain a close match with experimental spectra. Uncertainties in fundamental parameters such as cross section (Q), detector efficiency (ϵ), and mass absorption coefficient (μ/ρ) with the analytical model approach, which is described by Fiori and Swyt [91] limits its operation. Ding et al. [92], who computed the bremsstrahlung using Monte Carlo simulations, have described the Monte Carlo modeling (second approach); however, their work was limited to pure elements and normal electron beam incidences and furthermore absolute X rays were not computed. Converting the Xray intensity into concentration, using the ZAF or the $\varphi(\rho z)$ methods, are valid for specimens having homogeneous composition and flat surfaces [93]. Pouchou et al. [94] developed the quantitative schemes for quantitative X-ray microanalysis of multi-layered specimens, which are based on the $\varphi(\rho z)$ method. After that, this method extended for the microanalysis of surface segregation by Pouchou et al. [52]. Continue these activities, a quantitative method proposed for the microanalysis of spherical inclusions embedded in a matrix [95] as well as Monte Carlo simulations of X-ray emission from porous materials by Gauvin et al. [96, 97].

2. 9. 1 Peak to Background method

Another approach to determining quantitative X-ray microanalysis for rough surfaces, is the peak to background (P/B) method, which is an extension of the Marshall–Hall method for the correction of mass loss in beam-sensitive materials [98, 99]. The P/B method [100-108] is based on the opinion that although the characteristic X-ray intensity emitted from a non-flat surface is highly dependent on geometrical effects, the P/B ratio measured between the characteristic X-rays and the continuum X-rays of the same energy is much less susceptible to sample geometry. Table 2-2 includes measurements of the k-ratio (relative to bulk K411) and the P/B from the spectra of the NIST- K411 in Figure 2.18. The flake spectra show significant differences from the spectrum of the polished bulk sample, especially at low beam energies ($E_0 < 4 \text{ keV}$). While the k-ratio for Mg for these fragments differs by a factor of 2.95 for the most extreme case, the comparable P/B ratio for Mg only varies from that of the bulk sample by a factor of 1.03. For the combination of elements

in K411 at $E_0 = 20 \, \text{keV}$, the most severe difference in the P/B observed for these fragments is 1.13 for Ca.

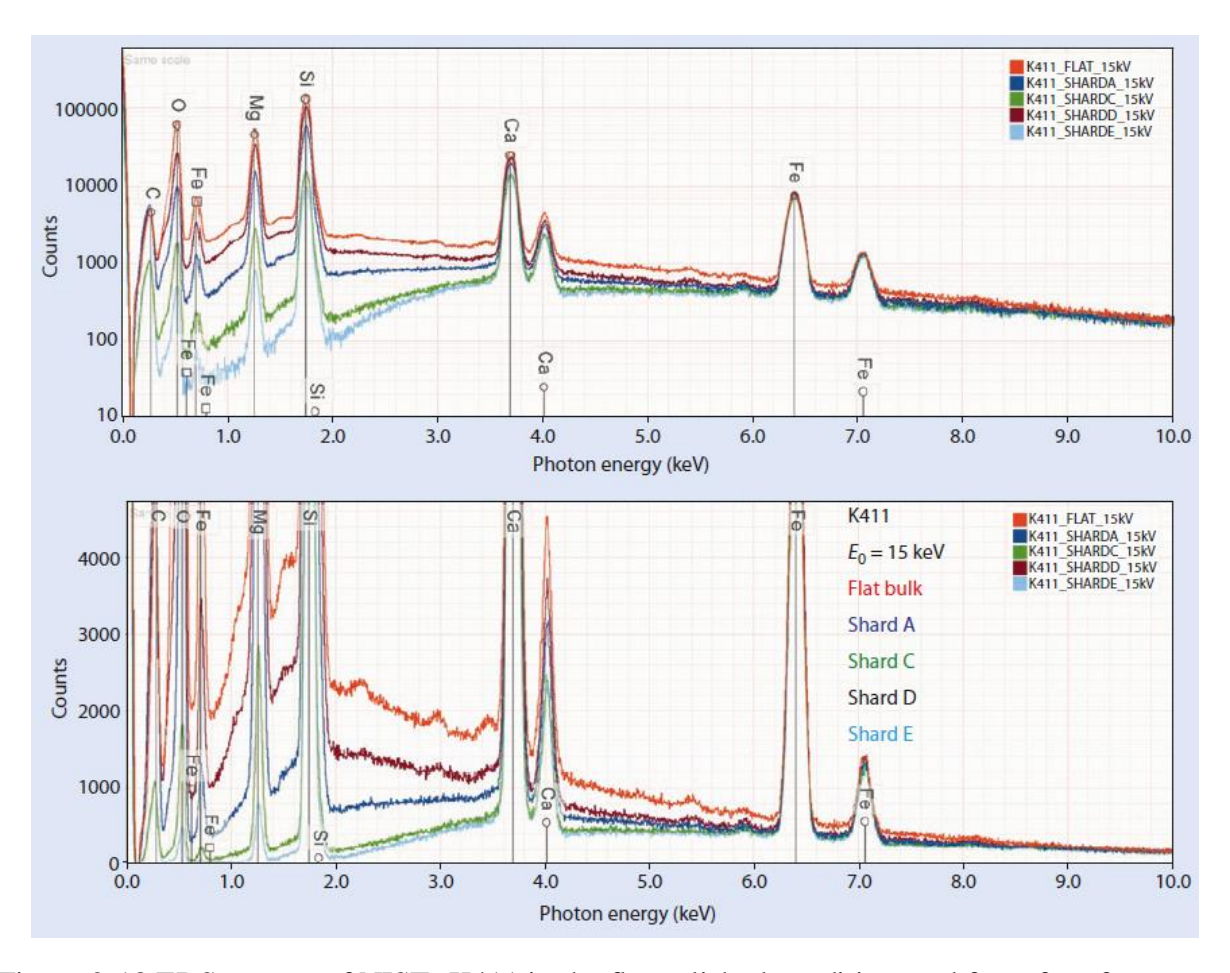


Figure 2-18 EDS spectra of NIST- K411 in the flat polished condition, and from four fragments, showing the variation in the spectral shape from the ideal [1].

Table 2-2 K411 fragments [1].

Sample	Element	P/B	k-ratio
Fragment A	Mg	4.52	0.545
Fragment C	Mg	4.49	0.339
Fragment D	Mg	4.52	1.132

Fragment E	Mg	4.73	0.389
Bulk	Mg	4.57	1.00
Fragment A	Si	16.35	0.617
Fragment C	Si	17.32	0.548
Fragment D	Si	14.95	1.06
Fragment E	Si	17.33	0.447
Bulk	Si	15.80	1.00
Fragment A	Ca	6.78	0.835
Fragment C	Ca	6.58	0.866
Fragment D	Ca	6.43	1.006
Fragment E	Ca	7.14	0.710
Bulk	Ca	6.37	1.00
Fragment A	Fe	6.48	0.911
Fragment C	Fe	6.29	0.941
Fragment D	Fe	6.50	0.986
Fragment E	Fe	6.82	0.886
Bulk	Fe	6.61	1.00
Range (shard/bulk)	Mg	1.03	2.95
Range (shard/bulk)	Si	1.10	2.24
Range (shard/bulk)	Ca	1.13	1.41
Range (shard/bulk)	Fe	1.03	1.13

Though the characteristic and continuum X-rays are produced by different physical processes [1] that have different behaviors as a function of the exciting electron energy; especially near the ionization threshold for an element, both characteristic and continuum X-rays are generated in nearly the same volume. Both types of radiation thus scale like the geometric mass effect because the loss of beam electrons due to backscattering and penetration also robs both characteristic and continuum generation processes, at least to a first order for photons of the same energy. Both types of radiation have a similar, although not identical, depth distribution; thus, the absorption paths to the detector are alike. As the same beam energy is chosen for characteristic and continuum X-rays, the geometric absorption effect is thus comparable for both. When making corrections for a non-

flat sample, the exact absorption path is very difficult to determine. Because the continuum radiation of the same beam energy is following the same path to the detector that the characteristic radiation follows, regardless of local shape, this continuum intensity I_B can be used as an automatic internal normalization factor to compensate for the major geometric effects. Additionally, the P/B ratio is independent of probe current; yet the quantification results need not be normalized. Therefore, both standards-based and standardless P/B algorithms have been implemented that provide an estimate of the analytical total [106-108].

2. 9. 1. 1 Basics of the P/B method

Take into account that the k-ratio for a sample relative to a flat, bulk standard of the same composition, $k = \frac{I_{samlpe}}{I_{bulk}}$. I is the intensity of the characteristic X-ray, I = P - B. I_{samlpe} is a strong function of the sample's size and shape, but the ratio $(\frac{I_{samlpe}}{I_{B, sample}})/(\frac{I_{Bulk}}{I_{B, Bulk}})$ involving the background at the same beam energy is nearly independent of sample size, except for very small particles where the anisotropy of the continuum emission becomes significant [109]. This experimental examination has been confirmed by theoretical calculations and Monte Carlo simulations [101, 102]. Incorporating the following correction scheme into a conventional ZAF method [100, 101]:

$$\frac{I_{\text{non-flat}}}{I_{\text{B, non-flat}}} = \frac{I_{\text{bulk}}}{I_{\text{B, bulk}}}$$
(2.28)

a modified particle intensity that compensates for the geometric effects, $I_{non-flat}^*$, can be calculated that is equivalent to the intensity that would be measured from a flat bulk target of the same composition as the particle:

$$I_{\text{non-flat}}^* \approx I_{\text{bulk}} = I_{\text{non-flat}} \times \frac{I_{\text{B, bulk}}}{I_{\text{B, non-flat}}}$$
 (2.29)

To apply Equation 2.29 for the analysis of a non-flat sample of unknown composition, the quantities $I_{non-flat}$ and $I_{B, non-flat}$ are determined from the measured X-ray spectrum. Because the composition of the non-flat sample is unknown, the term $I_{B, bulk}$ in Equation 2.29 is not known, as a bulk multi-element standard identical in composition to the unknown object is generally not available. However, an estimate of the concentrations of elements in the unknown

object is always available in the ZAF procedure, including the first step, where $C_i = \frac{k_i}{\sum k}$. The value of $I_{B, bulk}$ can therefore be estimated from the background measured on pure element standards:

$$I_{B, bulk} = \sum_{j} C_{j} I_{j,B,std}$$
 (2.30)

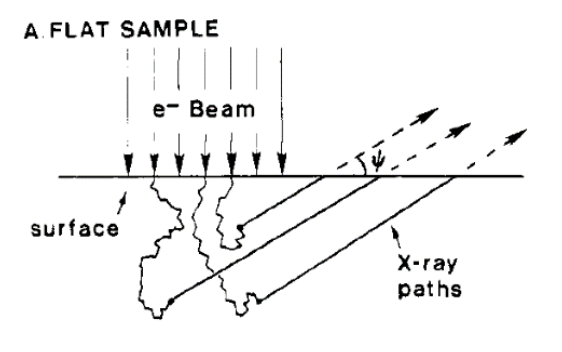
 $I_{j,B,std}$ is the pure element bremsstrahlung at the energy of interest and C_j is the composition of element j. The advantage of the P/B method is that it can be applied to spectra achieved with a focused probe directed at a specific location on a particle. Thus, particles that have a chemically heterogeneous sub-structure can be directly studied. To be effective, the P/B method requires spectra with high counts. Because the ratio of background intensities is used to scale the particle peak intensities, the statistical uncertainty in the background ratio propagates into the error in each concentration value in addition to the statistics of the characteristic peak. Even more importantly, the P/B method depends on the background radiation originating in the excited volume of the specimen only, and not in the surrounding substrate. When an irregularly shaped object such as a particle becomes small relative to the bulk interaction volume, the penetration of the beam into the substrate means that the continuum continues to be produced, even if the substrate is a low atomic number element such as carbon.

2. 9. 2 Armstrong model

Armstrong [110] developed an analytical technique and correction procedure to enable quantitative analysis of particles. Based on his model, for a non-flat specimen (Figure 2.19), 3D X-ray distribution [$\phi(x,y,z)$] must be known in advance instead of the depth distribution. For microanalysis of particles, it is required to correct the effects of sample size and shape on emitted X-ray intensity. For bulk specimens, correction effects is relatively simple. Such samples are thick with respect to electron penetration and, if the electron beam is normal to the specimen surface, the correction for x-ray absorption in the sample is a simple geometric function:

$$I_{A}(\rho z) = \varphi_{A}(\rho z)e^{-\mu_{A}csc\psi\rho z}$$
(2.31)

where ρ = density, $I_A(\rho z)$ = emitted x-ray intensity from the layer at depth Z in the sample, $\phi_A(\rho z)$ = generated primary x-ray intensity from layer at depth Z in the sample, μ_A = mass absorption coefficient by the sample for element A's x rays, ψ = take-off angle, angle between the sample-to-detector axis and the plane of the sample surface.



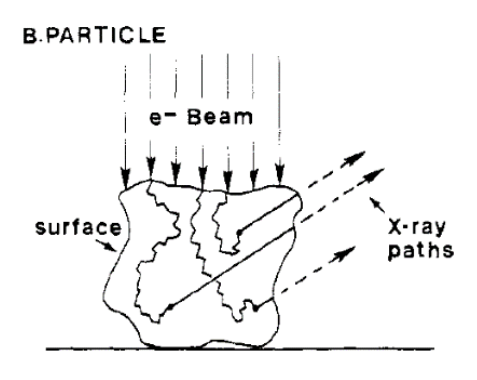


Figure 2-19 Schematic of X-ray path lengths in (A) thick flat specimen and (B) particle [110].

To calculate the total emitted primary x-ray intensity, one simply needs an accurate expression for $\phi_A(\rho z)$ and integrate the Equation (2.31) from $\rho z=0$ to ∞ or total depth of electron penetration (although as discussed below, derivation of a universally reliable expression for $\phi_A(\rho z)$ is by no means simple). In the case of the particle, electrons that would have stayed in the bulk specimen generating primary x rays may pass through the bottom or scatter out of the sides of the particle. Moreover, the x-ray absorption path length becomes a complicated function of x, y, and z related to the particle's size and shape. Thus, Equation (2.31) becomes for the particle.

$$I_{A}(\rho z) = \int_{y=\alpha_{1}(\rho z)}^{\alpha_{2}(\rho z)} \int_{x=\beta_{1}(\rho y, \rho z)}^{\beta_{2}(\rho y, \rho z)} \phi_{A}(\rho x, \rho y, \rho z) e^{-\mu_{A}g(\rho x, \rho y, \rho z)} d\rho x d\rho y \tag{2.32}$$

where $g(\rho x, \rho y, \rho z)$ is the distance from the point of x-ray generation to the particle surface along the sample-to-x-ray detector axis. To calculate $\phi_A(\rho x, \rho y, \rho z)$ it is necessary to estimate the spatial and energy distribution of the energetic electrons in the sample. For a multi-element sample containing a weight fraction C_A of element A, the number of x rays, dI, produced per electron path length, ds, is

$$dI = C_A \omega_A \rho_{iA} \frac{N_{A\rho}}{A_A} Q_A ds \tag{2.33}$$

where N_A = Avogadro's number, ρ = sample density, A_A = atomic weight of element A, $C_A \frac{N_{A\rho}}{A_A}$ = number of A atoms per unit volume, Q_A = ionization cross section for A atoms, a function of the electron energy, E, and the energy required to produce the ionization, E_c , ω_A = fluorescence yield, probability of ionization resulting in x-ray emission of A, nominally a constant, and ρ_{iA} = probability of x-ray emission being of the particular line of interest.

If one knows the number of electrons that pass through each point x, y, z, their energy distribution, and their angular distribution of travel through the x, y, z volume element, one can then derive an expression for $\phi_A(\rho x, \rho y, \rho z)$ from Equation (2.33):

$$\phi_{A}(\rho x, \rho y, \rho z) = C_{A} \frac{N_{A}}{A_{A}} \omega_{A} \rho_{ij} \int_{E=E_{0}}^{E_{c}} \int_{\theta=0}^{2\pi} \int_{\gamma=0}^{2\pi} \frac{n(E, \rho x, \rho y, \rho z, \theta, \gamma)}{\frac{d\rho s}{dV}} \times \frac{Q_{A}(E)}{\frac{dE}{d\rho s}} d\gamma d\theta dE$$
 (2.34)

where $n(E, \rho x, \rho y, \rho z, \theta, \gamma)$ = the number of electrons of energy E, scattering angle relative to the beam axis θ , and azimuthal angle in the plane normal to the beam axis γ , $\frac{dE}{d\rho s}$ = the mean electron energy loss while traveling $d\rho$, and $\frac{d\rho s}{dv}$ = the distance traveled by the electron going through the volume element dV at point x, y, z.

For the case of samples having a rough surface, Statham [104] proposed a quantitative model based on the peak to background ratio, using photons of the same energy nets (see section 2.9.1). Based on this method, the peak to background ratio is constant at any location on the non-flat surface and that this ratio is the same as that of a bulk material of the same composition having a flat surface. By assuming that this proposal is correct, then it is possible to convert rough sample intensity data into the intensity values measured for a flat sample of the same composition and thereby use the conventional quantitative analysis methods already mentioned. However, Gauvin et al. [56] by using a new generation of Monte Carlo program that computes the complete EDS x-ray spectra approved that the peak to background ratio is not constant for the rough surfaces. Gauvin showed, this method has some weakness. For instance, the assumption that the peak to background ratio is independent of the specimen non-flat is not strictly correct since the ionization cross sections and the bremstrahlung cross sections are not the same. Figure 2.20 shows X-ray k ratio as a function of the beam position on a non-flat surface for the Ni K_{α} and L_{α} lines and the Al

 K_{α} line which was obtained by new Monte Carlo program that developed by Gauvin et al. [56]. It is clear that the k ratio is a strong function of the non-flat of the specimen and these effects must be included in a quantitative procedure to relate the k ratio into specimen composition. Gauvin et al. [56] showed that the hypothesis that the peak to background is constant on a non-flat surface is not always true, especially for x-ray lines of low energy. Also, they mentioned that the peak to background ratio can be very sensitive to the electron probe diameter.

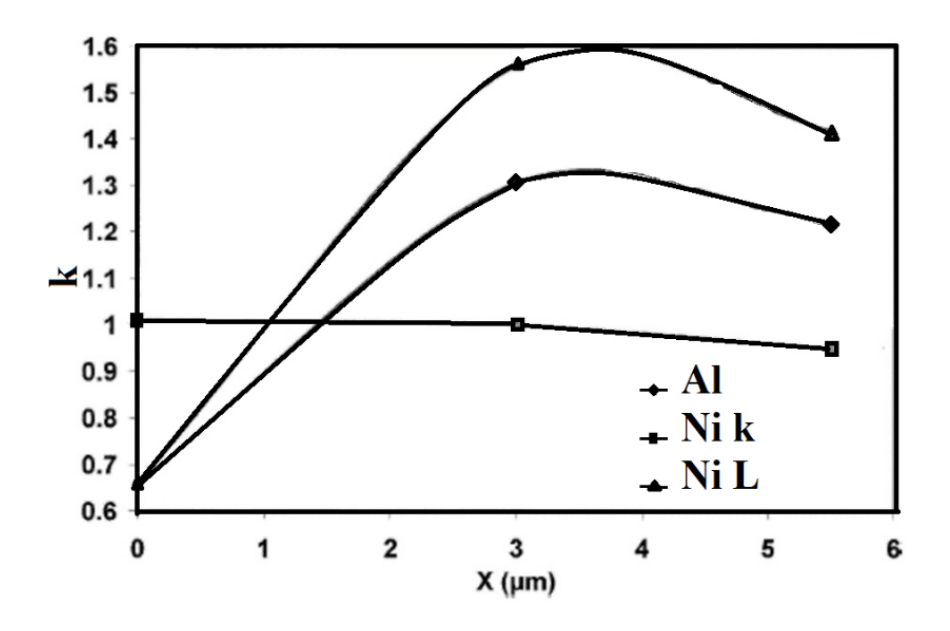


Figure 2-20 X-ray k ratio as a function of the beam position on a non-flat surface for the Ni K_{α} and L_{α} lines and the Al K_{α} line. The k ratios have been computed relative to a flat NiAl specimen. X corresponds to the height [56].

More recently Gauvin et al. [75] described a new Monte Carlo program (Win X-ray) that predicts X-ray spectra measured with an energy dispersive spectrometer (EDS) operating between 0.1 and 40 keV. There was an excellent prediction between an X-ray spectrum measured and a simulated spectrum by using Win X-ray. For example, Figure 2.21 shows the comparison of an X-ray spectrum measured from a Ti–Al 6.1 wt%–V 3.4 wt% alloy obtained at 15 keV and a simulated spectrum, which is presented by Gauvin et al. [75]. As it is seen, there is excellent prediction between measured and a simulated spectrum. Their new Monte Carlo program can simulate the complete X-ray spectrum of a given material of homogeneous composition. This program is expected to give correct approximations for the K, L, and M lines of any element as well as a good first-order estimation of the bremsstrahlung intensity. Win X-ray also can be used to find optimum

conditions to perform quantitative X-ray microanalysis in the SEM as well as to find minimum mass detection, as shown by Lifshin et al. [111].

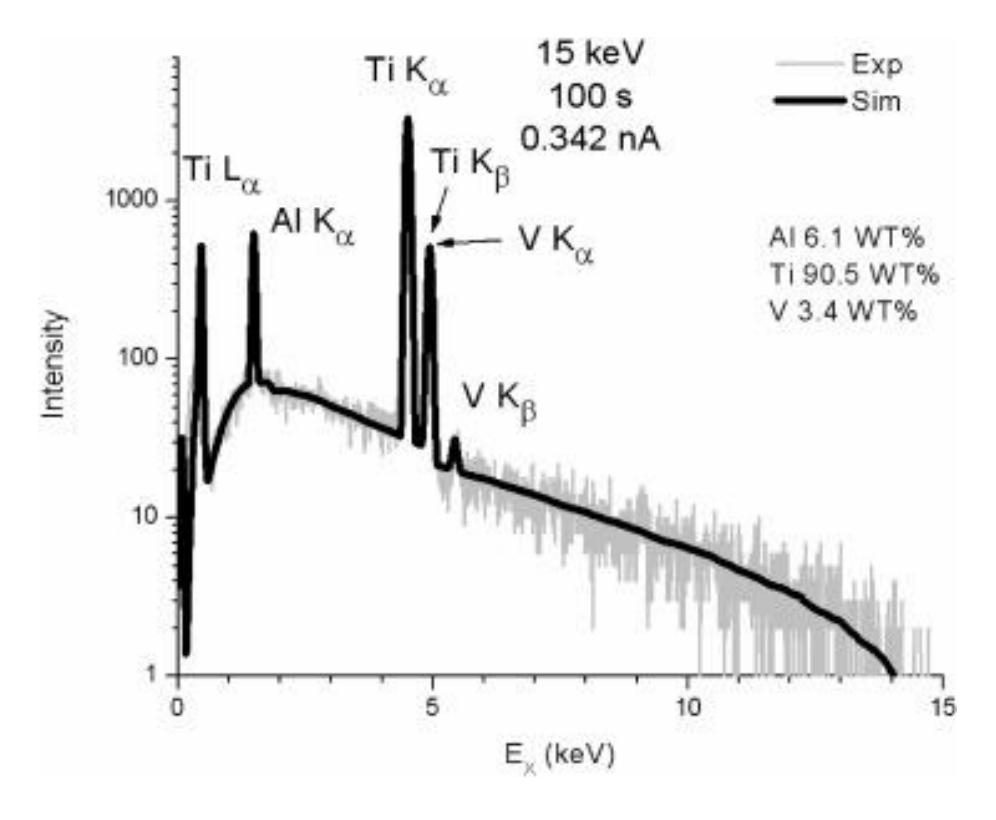


Figure 2-21 Comparison between a simulated and a measured Ti 90.5 wt% - Al 6.1wt%-V 3.4wt% [75].

2. 10. References

- 1. Goldstein, J.I., et al., Scanning electron microscopy and X-ray microanalysis. 2017: Springer.
- 2. Galyon Dorman, S.E., et al., Examination and prediction of corrosion fatigue damage and inhibition. Corrosion Reviews, 2017. 35: p. 355 363.
- 3. Roylance, D., Introduction to fracture mechanics. 2001.
- 4. Becker, W.T., et al., ASM handbook. Failure analysis and prevention, 2002. 11: p. 107.
- 5. Underwood, E.E., Quantitative fractography, in Applied metallography. 1986, Springer. p. 101-122.
- 6. Edition, M.H.N., vol. 12 Fractography. Metals Park, Ohio, 1987.
- 7. Broek, D., Some contributions of electron fractography to the theory of fracture. International Metallurgical Reviews, 1974. 19(1): p. 135-182.
- 8. Boyde, A., Quantitative photogrammetric analysis and qualitative stereoscopic analysis of SEM images. Journal of Microscopy, 1973. 98(3): p. 452-471.
- 9. Hilliard, J., Quantitative analysis of scanning electron micrographs. Journal of Microscopy, 1972. 95(1): p. 45-58.
- 10. Howell, P., Stereometry as an aid to stereological analysis. Journal of Microscopy, 1980. 118(2): p. 217-220.
- 11. Eisenhart, L.P., Coordinate geometry. 2005: Courier Corporation.
- 12. Manhart, C. and H. Harmuth, A stereoscopic method for fractographic investigations of ordinary ceramics, in Fracture of Nano and Engineering Materials and Structures. 2006, Springer. p. 297-298.
- 13. Pouchou, J.-L., et al., 3D reconstruction of rough surfaces by SEM stereo imaging. Microchimica Acta, 2002. 139(1): p. 135-144.
- 14. Zheng, L., G. Li, and J. Sha. The survey of medical image 3D reconstruction. in Fifth International Conference on Photonics and Imaging in Biology and Medicine. 2007. SPIE.
- 15. Buelthoff, H.H. and A.L. Yuille. Shape-from-X: Psychophysics and computation. in Sensor Fusion III: 3D Perception and Recognition. 1991. SPIE.
- 16. Tomasi, C. and T. Kanade, Shape and motion from image streams under orthography: a factorization method. International journal of computer vision, 1992. 9(2): p. 137-154.

- 17. Arsalan Soltani, A., et al. Synthesizing 3d shapes via modeling multi-view depth maps and silhouettes with deep generative networks. in Proceedings of the IEEE conference on computer vision and pattern recognition. 2017.
- 18. Moons, T., L. Van Gool, and M. Vergauwen, 3D reconstruction from multiple images part 1: Principles. Foundations and Trends® in Computer Graphics and Vision, 2010. 4(4): p. 287-404.
- 19. Fusiello, A., Uncalibrated Euclidean reconstruction: a review. Image and Vision Computing, 2000. 18(6-7): p. 555-563.
- Oliensis, J. and M. Werman. Structure from motion using points, lines, and intensities. in Proceedings IEEE Conference on Computer Vision and Pattern Recognition. CVPR 2000 (Cat. No. PR00662). 2000. IEEE.
- 21. Debevec, P.E., C.J. Taylor, and J. Malik. Modeling and rendering architecture from photographs: A hybrid geometry-and image-based approach. in Proceedings of the 23rd annual conference on Computer graphics and interactive techniques. 1996.
- 22. Quan, L. and T. Kanade, Affine structure from line correspondences with uncalibrated affine cameras. IEEE Transactions on Pattern Analysis and Machine Intelligence, 1997. 19(8): p. 834-845.
- 23. Zhang, Z., Estimating motion and structure from correspondences of line segments between two perspective images. IEEE Transactions on pattern analysis and machine intelligence, 1995. 17(12): p. 1129-1139.
- 24. McCann, S., 3d reconstruction from multiple images. Stanford Computational Vision and Geometric Lab, 2015.
- 25. Nyimbili, P.H., et al. Structure from motion (sfm)-approaches and applications. in Proceedings of the international scientific conference on applied sciences, Antalya, Turkey. 2016.
- 26. Snavely, N., S.M. Seitz, and R. Szeliski, Modeling the world from internet photo collections. International journal of computer vision, 2008. 80(2): p. 189-210.
- 27. Furukawa, Y. and J. Ponce, Accurate, dense, and robust multiview stereopsis. IEEE transactions on pattern analysis and machine intelligence, 2009. 32(8): p. 1362-1376.
- 28. Tafti, A.P., et al., Recent advances in 3D SEM surface reconstruction. Micron, 2015. 78: p. 54-66.

- 29. Carli, L., et al., Uncertainty evaluation for three-dimensional scanning electron microscope reconstructions based on the stereo-pair technique. Measurement Science and Technology, 2011. 22(3): p. 035103.
- 30. Raspanti, M., et al., A vision-based, 3D reconstruction technique for scanning electron microscopy: Direct comparison with atomic force microscopy. Microscopy research and technique, 2005. 67(1): p. 1-7.
- 31. Chan, E.K., et al., A new method for volumetric measurement of orthodontically induced root resorption craters. European journal of oral sciences, 2004. 112(2): p. 134-139.
- 32. Samak, D., A. Fischer, and D. Rittel, 3D reconstruction and visualization of microstructure surfaces from 2D images. CIRP annals, 2007. 56(1): p. 149-152.
- 33. Bernard, A. and A. Fischer, New trends in rapid product development. CIRP Annals, 2002. 51(2): p. 635-652.
- 34. Stampfl, J., et al., Reconstruction of surface topographies by scanning electron microscopy for application in fracture research. Applied Physics A, 1996. 63(4): p. 341-346.
- 35. Barnard, S.T. and M.A. Fischler, Computational stereo. ACM Computing Surveys (CSUR), 1982. 14(4): p. 553-572.
- 36. Bakic, G., et al., 3D PROFILING OF 12Cr HEAT RESISTANTE STEEL CHARPY V NOCH FRACTURE SURFACES OBTAINED AT DIFFERENT TEMPERATURES.
- 37. Zhou, W. and Z.L. Wang, Scanning microscopy for nanotechnology: techniques and applications. 2007: Springer science & business media.
- 38. Bethe, H., Theory of the transmission of corpuscular radiation through matter. Ann Phys Leipzig, 1930. 5: p. 325.
- 39. Scott, V.D. and G. Love, Quantitative electron-probe microanalysis. 1983.
- 40. Heinrich, K., Mass absorption coefficients for electron probe microanalysis. Proc. 11th Int. Congr. on X-Ray Optics and Microanalysis, 1986: p. 67-119.
- 41. Henke, B.L., E.M. Gullikson, and J.C. Davis, X-ray interactions: photoabsorption, scattering, transmission, and reflection at E= 50-30,000 eV, Z= 1-92. Atomic data and nuclear data tables, 1993. 54(2): p. 181-342.
- 42. Chantler, C.T., Theoretical form factor, attenuation, and scattering tabulation for Z= 1–92 from E= 1–10 eV to E= 0.4–1.0 MeV. Journal of Physical and Chemical Reference Data, 1995. 24(1): p. 71-643.

- 43. Castaing, R. and J. Descamps, Sur les bases physiques de l'analyse ponctuelle par spectrographie X. Journal de Physique et le Radium, 1955. 16(4): p. 304-317.
- 44. Schmitz, U., P. Ryder, and W. Pitsch. An experimental method for determining the depth distribution of characteristic X-rays in electron microprobe specimens. in Vth International Congress on X-Ray Optics and Microanalysis/V. Internationaler Kongreß für Röntgenoptik und Mikroanalyse/Ve Congrès International sur l'Optique des Rayons X et la Microanalyse. 1969. Springer.
- 45. Duncumb, P. and D. Melford, X-ray Optics and Microanalysis. Hermann, Paris, 1966: p. 240-253.
- 46. Bishop, H., The prospects for an improved absorption correction in electron probe microanalysis. Journal of Physics D: Applied Physics, 1974. 7(14): p. 2009.
- 47. Love, G., D. Sewell, and V. Scott, An improved absorption correction for quantitative analysis. Le Journal de Physique Colloques, 1984. 45(C2): p. C2-21-C2-24.
- 48. Packwood, R. and J. Brown, A Gaussian expression to describe φ (ρz) curves for quantitative electron probe microanalysis. X-ray Spectrometry, 1981. 10(3): p. 138-146.
- 49. Brown, J. and R. Packwood, Quantitative electron probe microanalysis using Gaussian φ (ρz) Curves. X-ray Spectrometry, 1982. 11(4): p. 187-193.
- 50. Bastin, G., F. Van Loo, and H. Heijligers, Evaluation of the use of Gaussian φ (ρz) curves in quantitative electron probe microanalysis: a new optimization. X-Ray Spectrometry, 1984. 13(2): p. 91-97.
- 51. Pouchou, J. and F. Pichoir, Quantitative microanalytic possibilities using a new formulation of matrix effects. Journal de Physique, 1984. 45(NC-2): p. 17-20.
- 52. Pouchou, J. and F. Pichoir, Un nouveau modèle de calcul pour la microanalyse quantitative par spectrométrie de rayons X. La recherche aérospatiale, 1984. 3(167): p. 92.
- 53. Pouchou, J., F. Pichoir, and D. Newbury, A simplified version of the "PAP" model for matrix corrections in EPMA. Microbeam analysis, 1988: p. 315-318.
- 54. Pouchou, J.-L. and F. Pichoir, Quantitative analysis of homogeneous or stratified microvolumes applying the model "PAP", in Electron probe quantitation. 1991, Springer. p. 31-75.
- 55. Reed, S.J.B., Electron microprobe analysis and scanning electron microscopy in geology. 2005: Cambridge university press.

- 56. Gauvin, R. and E. Lifshin, X-ray microanalysis of real materials using Monte Carlo simulations. Microchimica Acta, 2004. 145(1): p. 41-47.
- 57. Terauchi, M., et al., A new WDS spectrometer for valence electron spectroscopy based on electron microscopy. JEOL News, 2012. 47(1): p. 23-28.
- 58. Fitzgerald, R., K. Keil, and K.F. Heinrich, Solid-state energy-dispersion spectrometer for electron-microprobe X-ray analysis. Science, 1968. 159(3814): p. 528-530.
- 59. Gatti, E. and P. Rehak, Semiconductor drift chamber—An application of a novel charge transport scheme. Nuclear Instruments and Methods in Physics Research, 1984. 225(3): p. 608-614.
- 60. Strüder, L., et al., High-resolution high-count-rate X-ray spectroscopy with state-of-the-art silicon detectors. Journal of Synchrotron Radiation, 1998. 5(3): p. 268-274.
- 61. Cubukçu, H.E., et al., WDS versus silicon drift detector EDS: A case report for the comparison of quantitative chemical analyses of natural silicate minerals. Micron, 2008. 39(2): p. 88-94.
- 62. Ritchie, N.W., D.E. Newbury, and J.M. Davis, EDS measurements of X-ray intensity at WDS precision and accuracy using a silicon drift detector. Microscopy and Microanalysis, 2012. 18(4): p. 892-904.
- 63. Castaing, R., Application of electron probes to local chemical and crystallographic analysis. Ph. D. Thesis (University of Paris), 1951.
- 64. Horny, P., Development of a quantification method for X-ray microanalysis with an electron microscope. 2006.
- 65. Teng, C., H. Demers, and R. Gauvin, The standard-based f-ratio quantitative x-ray microanalysis method for a field emission SEM. Microscopy and Microanalysis, 2018. 24(S1): p. 732-733.
- 66. Horny, P., et al., Development of a new quantitative X-ray microanalysis method for electron microscopy. Microscopy and Microanalysis, 2010. 16(6): p. 821-830.
- 67. Cliff, G. and G.W. Lorimer, The quantitative analysis of thin specimens. Journal of Microscopy, 1975. 103(2): p. 203-207.
- 68. Brodusch, N., H. Demers, and R. Gauvin, Field emission scanning electron microscopy: New perspectives for materials characterization. 2018: Springer.

- 69. Gauvin, R., N. Brodusch, and P. Michaud. Determination of Diffusion Coefficients with Quantitative X-Ray Microanalysis at High-Spatial Resolution. in Defect and Diffusion Forum. 2012. Trans Tech Publ.
- 70. Teng, C., Y. Yuan, and R. Gauvin, The f-ratio quantification method applied to standard minerals with a cold field emission SEM/EDS. Talanta, 2019. 204: p. 213-223.
- 71. Joy, D.C., Monte Carlo modeling for electron microscopy and microanalysis. Vol. 9. 1995: Oxford University Press.
- 72. Heinrich, K., and Heinrich, K., The role of monte carlo calculations in electron probe microanalysis and scanning electron microscopy. ectron Probe Microanalysi.'anning Electrc Microscop, 1976: p. 1.
- 73. Kyser, D., et al., Electron Beam Interactions with Solids for Microscopy. Microanalysis and Microlithography (Scanning Electron Microscopy, O'Hare, IL, 1984), 1982: p. 287-298.
- 74. Shimizu, R. and Ding. Z.J., Monte Carlo modelling of electron-solid interactions. Reports on Progress in Physics, 1992. 55(4): p. 487.
- 75. Gauvin, R., et al., Win X-ray: A New Monte Carlo Program that Computes X-ray Spectra Obtained with a Scanning Electron Microscope. Microscopy and Microanalysis, 2006. 12(1): p. 49-64.
- 76. Joy, D. and S. Luo, An empirical stopping power relationship for low-energy electrons. Scanning, 1989. 11(4): p. 176-180.
- 77. Drouin, D., et al., CASINO V2. 42—a fast and easy-to-use modeling tool for scanning electron microscopy and microanalysis users. Scanning: The Journal of Scanning Microscopies, 2007. 29(3): p. 92-101.
- 78. Gauvin, R. and P. Michaud, MC X-ray, a new Monte Carlo program for quantitative X-ray microanalysis of real materials. Microscopy and Microanalysis, 2009. 15(S2): p. 488-489.
- 79. Curgenven, L. and P. Duncumb, Simulation of electron trajectories in a solid target by a simple Monte Carlo technique. 1971: TI Research Laboratories.
- 80. Love, G., M. Cox, and V. Scott, A simple Monte Carlo method for simulating electron-solid interactions and its application to electron probe microanalysis. Journal of Physics D: Applied Physics, 1977. 10(1): p. 7.

- 81. Joy, D.C., An introduction to Monte Carlo simulations. Scanning microscopy, 1991. 5(2): p. 4.
- 82. Karduck, P. and W. Rehbach, The Use of Tracer Experiments and Monte Carlo Calculations in the φ (ρz) Determination for Electron Probe Microanalysis, in Electron Probe Quantitation. 1991, Springer. p. 191-217.
- 83. Armigliato, A., et al., Thickness determination of Al films on Si by a monte carlo code including a secondary fluorescence correction. The Journal of Physics Colloquia 45, no. C2 (1984): C2-29.
- 84. Fitzgerald, A., A. Gillies, and H. Watton, A comparison of the composition of thin films on substrates determined by EDX and surface analysis. Surface and Interface Analysis, 1990. 16(1-12): p. 163-167.
- 85. Newbury, D.E., et al., Monte Carlo electron trajectory simulation, an aid for particle analysis. Characterization of Particles, 1980. 460: p. 39-62.
- 86. Llovet, X., E. Valovirta, and E. Heikinheimo, Monte Carlo simulation of secondary fluorescence in small particles and at phase boundaries. Microchimica Acta, 2000. 132(2): p. 205-212.
- 87. Ritchie, N.W., Spectrum simulation in DTSA-II. Microscopy and Microanalysis, 2009. 15(5): p. 454-468.
- 88. Hovington, P., D. Drouin, and R. Gauvin, CASINO: A new Monte Carlo code in C language for electron beam interaction—Part I: Description of the program. Scanning, 1997. 19(1): p. 1-14.
- 89. Rudinsky, S., et al., Extending Monte Carlo Simulations of Electron Microscopy Images and Hyperspectral Images in a User-Friendly Framework. Microscopy and Microanalysis, 2019. 25(S2): p. 222-223.
- 90. Ritchie, N.W., Efficient simulation of secondary fluorescence via NIST DTSA-II Monte Carlo. Microscopy and Microanalysis, 2017. 23(3): p. 618-633.
- 91. Fiori, C. and C. Swyt, The use of theoretically generated spectra to estimate detectability limits and concentration variance in energy—dispersive X-ray microanalysis. Microbeam analysis, 1989: p. 236-238.

- 92. Ding, Z.J., R. Shimizu, and K. Obori, Monte Carlo simulation of x-ray spectra in electron probe microanalysis: Comparison of continuum with experiment. Journal of applied physics, 1994. 76(11): p. 7180-7187.
- 93. Poirier, D. and R. Gauvin, X-ray microanalysis of porous materials using Monte Carlo simulations. Scanning, 2011. 33(3): p. 126-134.
- 94. Pouchou, J. and F. Pichoir, Electron probe X-ray microanalysis applied to thin surface films and stratified specimens. Scanning Microscopy, 1993. 1993(7): p. 12.
- 95. Gauvin, R., P. Hovington, and D. Drouin, Quantification of spherical inclusions in the scanning electron microscope using Monte Carlo simulations. Scanning, 1995. 17(4): p. 202-219.
- 96. Gauvin, R., X-Ray Emission from Porous Materials : New Results. Microscopy and Microanalysis, 1998. 4(S2): p. 206-207.
- 97. Gauvin, R., Review of transmission electron microscopy for the characterization of materials. Optical Science, Engineering and Instrumentation '97. Vol. 10291. 1997: SPIE.
- 98. Marshall, D. and T.A. Hall, A method for the microanalysis of thin films. X-ray Optics and Microanalysis, eds. Castaing R, Deschamps P, Philibert J.(Hermann, Paris), 1966. 374.
- 99. Hall, T., Some aspects of the microprobe analysis of biological specimens. Quantitative electron probe microanalysis, 1968(298).
- 100. Small, J.A.H., K. F. J.; Newbury, D. E.; Myklebust, R. L., Progress in the Development of the Peak-to-Background Method for the Quantitative Analysis of Single Particles with the Electron Probe. Scanning Electron Microscopy, 1979. 2.
- 101. Small, J., et al., The production and characterization of glass fibers and spheres for microanalysis. Scanning Electron Microsc, 1978. 1: p. 445-454.
- 102. Statham, P. and J. Pawley, New method for particle X-ray Micro-analysis based on peak to background measurements, in Scanning electron microscopy/1978. Vol. I. 1978.
- 103. Statham, P.J. and J.B. Pawley, New method for particle x-ray micro-analysis based on peak to background measurements. 1978, United States: Scanning Electron Microscopy, Inc.
- 104. Statham, P., Measurement and use of peak-to-background ratios in X-ray analysis. Mikrochimica Acta, 1979. 8: p. 229-242.

- 105. Wendt, M. and A. Schmidt, Improved reproducibility of energy-dispersive X-ray microanalysis by normalization to the background. physica status solidi (a), 1978. 46(1): p. 179-183.
- 106. August, H.J. and J. Wernisch, Calculation of the depth distribution function for continuous radiation. Scanning, 1991. 13(3): p. 207-215.
- 107. August, H.J. and J. Wernisch, Calculation of depth distribution functions for characteristic x-radiation using an electron scattering model. II—results. X-Ray Spectrometry, 1991. 20(3): p. 141-148.
- 108. August, H.J. and J. Wernisch, Calculation of depth distribution functions for characteristic x-radiation using an electron scattering model. I—theory. X-Ray Spectrometry, 1991. 20(3): p. 131-140.
- 109. Small, J., et al., Procedure for the quantitative analysis of single particles with the electron probe. Characterization of particles, 1980. 533: p. 29.
- 110. Armstrong, J.T. and Buseck, P.R., Quantitative chemical analysis of individual microparticles using the electron microprobe. Theoretical. Analytical chemistry, 1975. 47(13): p. 2178-2192.
- 111. Lifshin, E., Statistical consideration in EDS microanalysis. Microscopy and Microanalysis, 1998. 4(S2): p. 208-209.

Chapter 3. Investigation of the Effect of Magnification, Accelerating Voltage, and Working Distance on the 3D Digital Reconstruction Techniques

The accuracy of the 3D digital reconstruction is a key point for quantitative microanalysis of rough surfaces. This chapter introduces the effect of SEM parameters on 3D digital rebuilding. Magnification, Accelerating Voltage, and Working Distance are the most important SEM parameters that can affect the accuracy of the 3D model. In this part of the project, the optimum condition of SEM parameters that can help us to achieve an accurate 3D model will be investigated.

This chapter has been published as: S. M. Bayazid*, N. Brodusch, R. Gauvin, Investigation
of the Effect of Magnification, Accelerating Voltage, and Working Distance on the 3D
Digital Reconstruction Techniques, Scanning 2020, (2020) 3743267.

3. 1. Abstract

In this study, the effect of Scanning Electron Microscopy (SEM) parameters such as magnification (M), accelerating voltage (V), and working distance (WD) on the 3D digital reconstruction technique, as the first step of the quantitative characterization of fracture surfaces with SEM were investigated. The 2D images were taken via a 4-Quadrant Backscattered Electron (4Q-BSE) detector. In this study, spherical particles of Ti-6Al-4V (15-45 µm) deposited on the silicon substrate were used. It was observed that the working distance has a significant influence on the 3D digital rebuilding method via SEM images. The results showed the best range of the working distance for our system is 9 to 10 mm. It was shown that by increasing the magnification to 1000X, the 3D digital reconstruction results improved. However, there was no significant improvement by increasing the magnification beyond 1000X. In addition, results demonstrated that the lower the accelerating voltage, the higher precision of the 3D reconstruction technique, as long as there are clean backscattered signals. The optimal condition was achieved when magnification, accelerating voltage, and working distance were chosen as 1000 X, 3 kV, and 9 mm, respectively.

3. 2. Introduction

The development of the scanning electron microscope (SEM) [1] and the 3D digital reconstruction techniques [2-4] along with the development of image processing methods, hardware and software, can significantly help in a broad range of application such as investigation of fracture surfaces [5], surface engineering [6], 3D printing [7], and biological researches [8]. To reconstruct a 3D digital image from multiple SEM images, correct types of features should be chosen on the 2D images [9]. Therefore, the quality of the SEM images is the critical point in any 3D digital reconstruction method. There is a large body of research in literature on 3D digital reconstruction techniques [10-12]; however, many problems remain unsolved related to the effect of SEM parameters on the quality of 3D digital images which are obtained with SEM micrographs. Recently, some efforts have been devoted to improving the quality and correctness of the 3D digital images which were obtained with secondary electron (SE) images [13-15].

The quality of the 3D digital reconstruction method is based on shape, surface structure of the object, and the SE micrograph quality [16]. It was shown that the In-lens detector has much better results of 3D image reconstruction in comparison with the Everhart-Thornley detector since the Everhart-Thornley detector is submitted to shadowing effects more than In-lens detector [17]. It is also reported that the SEM magnification does not improve 3D digital reconstruction results [4]. However, magnification can affect the resolution and the quality of the micrographs [18, 19] and as a result, it can affect the quality of 3D digital rebuilding. By taking into account that rotation and tilting are two main factors in 3D digital reconstruction of SEM images, it was observed that for the case of rotations, the largest uncertainty contribution is due to the reproducibility of the rotational angle, followed by the bias of the pixel size.

On the other hand, for the case of tilting, the largest uncertainty contribution is due to the bias of the pixel size, followed by the reproducibility of the tilt angle [20]. On the other hand, there is very limited research concerning the 3D digital images which are obtained with backscattered electron (BSE) images [21, 22]. Since the presence of a non-flat surface differs significantly with the type, solid angle, and take-off angle of the detector used to collect the signal [18] the location of the detector could play a significant role for obtaining more signals from rough surfaces. Therefore, backscattered electrons are most efficiently and selectively collected with a 4-Quadrant Backscattered Electron (4Q-BSE) detector directly located on top of the sample. Consequently, in

this paper, the effects of SEM parameters on the 3D digital images which are taken via BSE images, as the first step of the quantitative characterization of fracture surfaces are studied.

3. 3. Method

The spherical particles of Ti-6Al-4V with different size (15-45 μ m) deposited on the silicon substrate were used (Figure 3.1). Given that the size of the spherical particles was available, the use of these spherical particles on a flat surface allowed to ensure the accuracy of the produced 3D digital images. The imaging process was performed with the SU3500 variable-pressure-SEM (Hitachi-3500) with 4-Q BSE detector (Figure 3.2) in the vacuum mode (30 Pa) with only one scan to find out the effect of SEM parameters such as magnification (M), accelerating voltage (V), and working distance (WD) in the range of 500-2000X, 3-20 kV, and 8-12 mm, respectively. Beam current, and spot intensity, were set on 146 μ A and 40 (unitless value from the SEM operating software), respectively. Each image was focused manually, and manual stigmator correction was applied after every image. The Relative Radius (R_r), Equation. 3.1, was used as a comparison operator for the size of any particles between 2D and 3D images. The relative radius was measured from 3D reconstruction's profile. After the 3D rebuilding of spherical particles, it was possible to take measurements from the non-flat profile at any position in the 3D image and then make an average.

$$R_{\rm r} = \frac{r_{\rm z} - r_{\rm X=Y}}{r_{\rm X=Y}} \times 100 \tag{3.1}$$

where R_r is the relative radius in percentage, r_z is the radius of a spherical particle in the Z direction (in the 3D image), and $r_{X=Y}$ is the radius of the same spherical particle in the X or Y direction (in the 2D image).

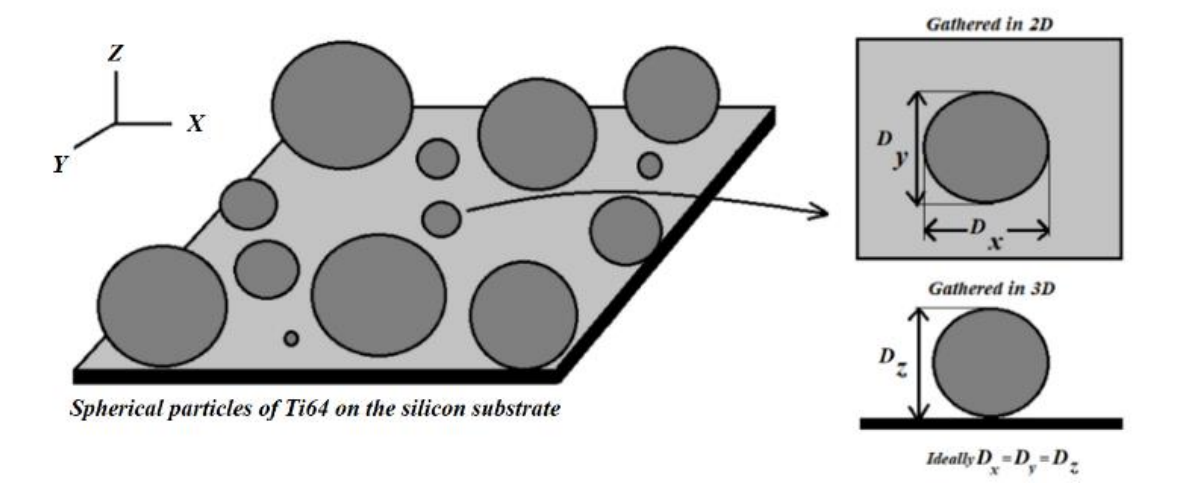


Figure 3-1 The spherical particles of Ti-6Al-4V on the silicon substrate.

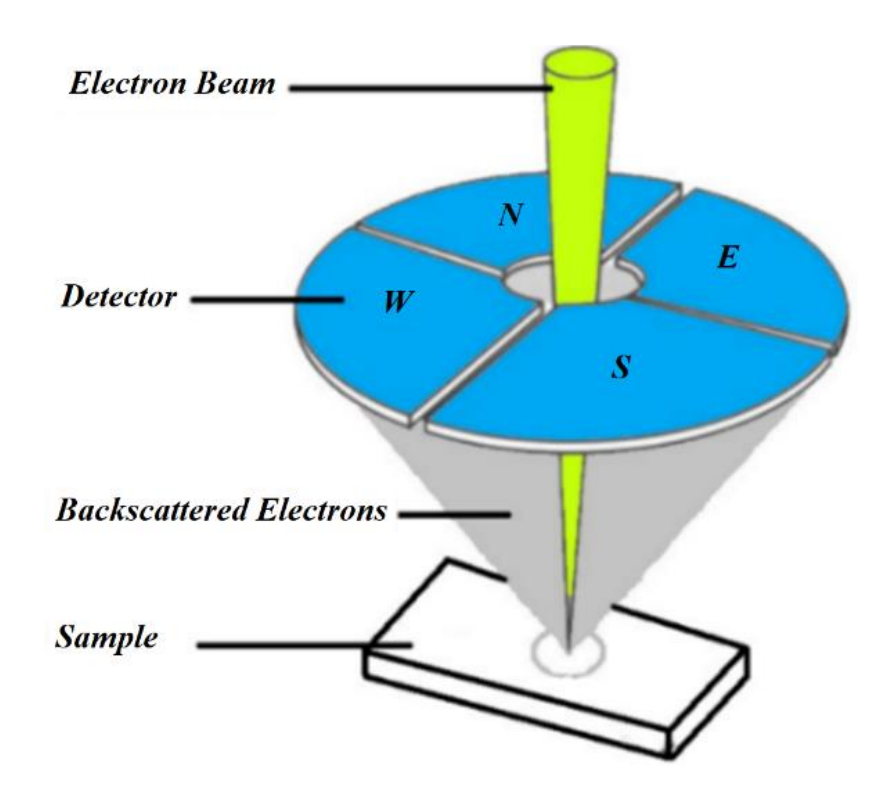


Figure 3-2 A 4-Q BSE detector.

3.4. Results

Figure 3.3 illustrates the BSE images of the different spherical particles with different magnifications. The accelerating voltage and working distance were set as constant values of 3 kV, and 9 mm, respectively. Figure 3.4 presents a 3D digital reconstruction of Ti-6Al-4V particles

along with the height profile which are shown in Figure 3.3. Figure 3.4 shows that by increasing the magnification, the non-flat profile which is the radius of the spherical particle in 3D mode increases and becomes comparable with radius of the spherical particle in 2D mode. Therefore, the higher magnification, the higher precision of 3D digital image. Figure 3.5 shows the BSE images of the different spherical particles with different accelerating voltage. The magnification and working distance were set as constant values of 1000 kV, and 9 mm, respectively. Figure 3.5 shows that the appearance of shadow and small features (shown with arrows) in the 2D images diminish by increasing the accelerating voltage because the interaction volume is proportional to the accelerating voltage (Equation. 3.2) [18]. The profile in the Figure 3.6 shows the same trend, the higher accelerating voltage, the lower precision of 3D digital image.

$$R_{K-0}(nm) = 27.6 \left(\frac{A}{7}\right)^{0.89} \rho E_0^{1.67}$$
(3.2)

where A is the atomic weight (g/mol), Z is the atomic number, ρ is the density (g/cm³), and E₀ is the incident beam energy (keV).

The BSE images of the different spherical particles which were taken at different working distance are shown in Figure 3.7. The magnification and accelerating voltage were set as constant values of 1000X, and 3 kV, respectively. The profile in Figure 3.8 shows a different scenario; the precision of 3D digital image increases by increasing the working distance but after a specific point (WD = 9 mm), start to decrease.

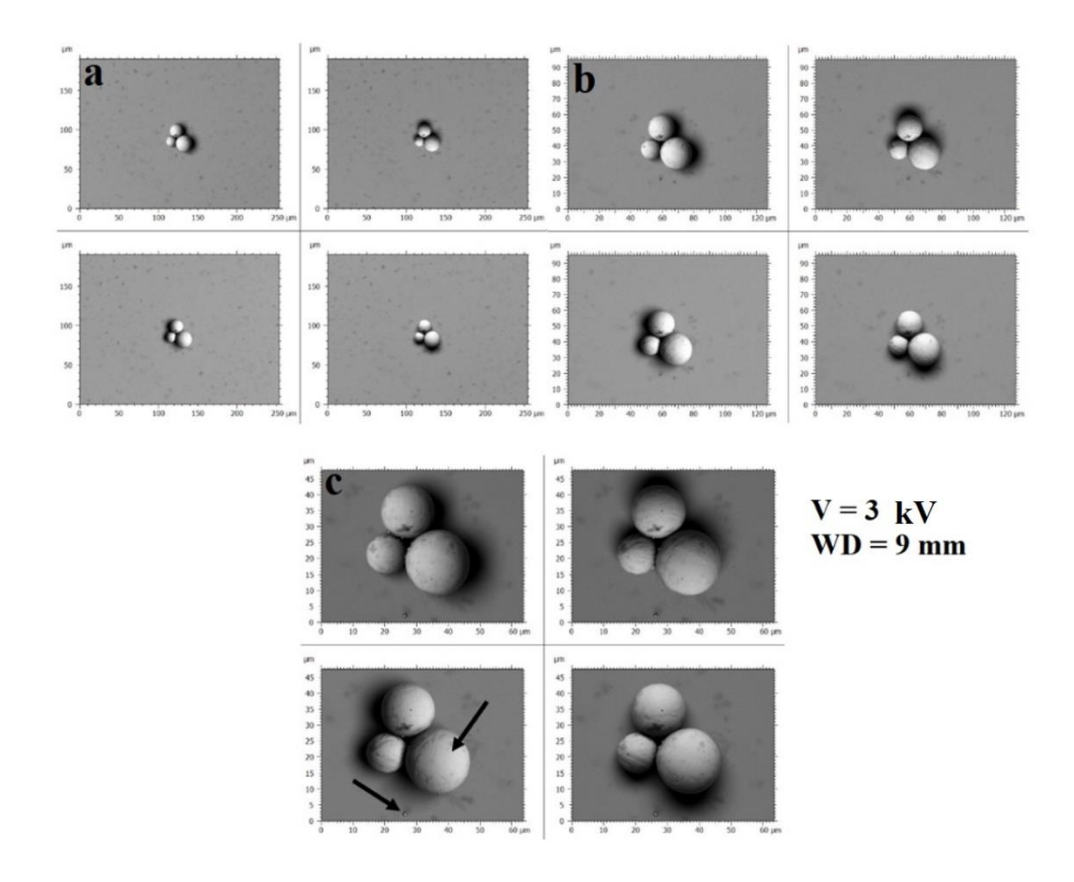


Figure 3-3 Backscattered electron images taken by 4-Q BSE detector at different magnification; a) 500X, b) 1000X, and c) 2000X.

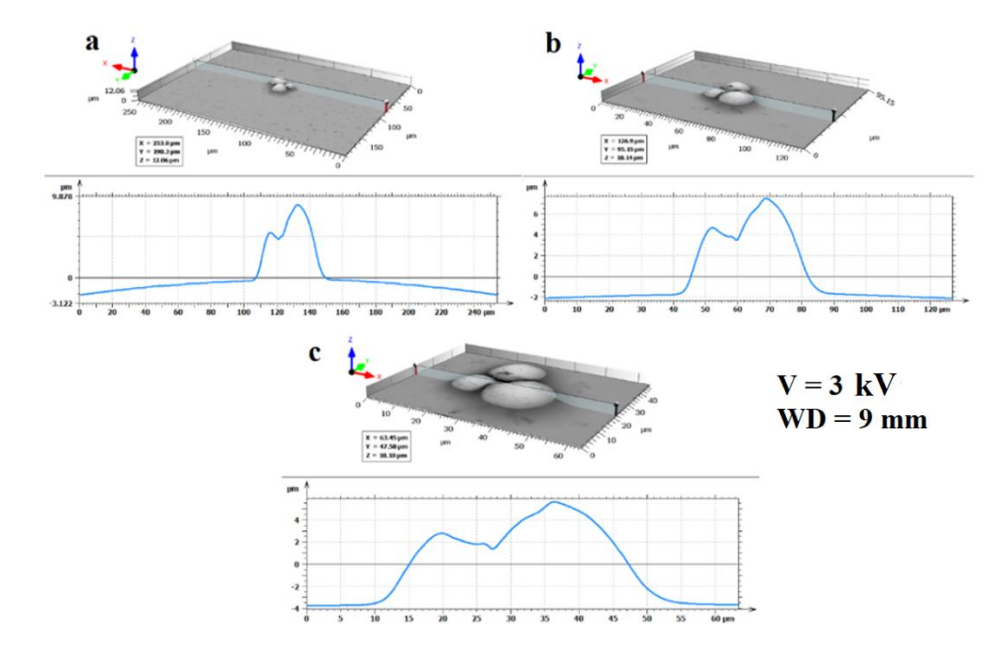


Figure 3-4 3D digital reconstructed image along with profile at different magnification; a) 500X, b) 1000X, and c) 2000X.

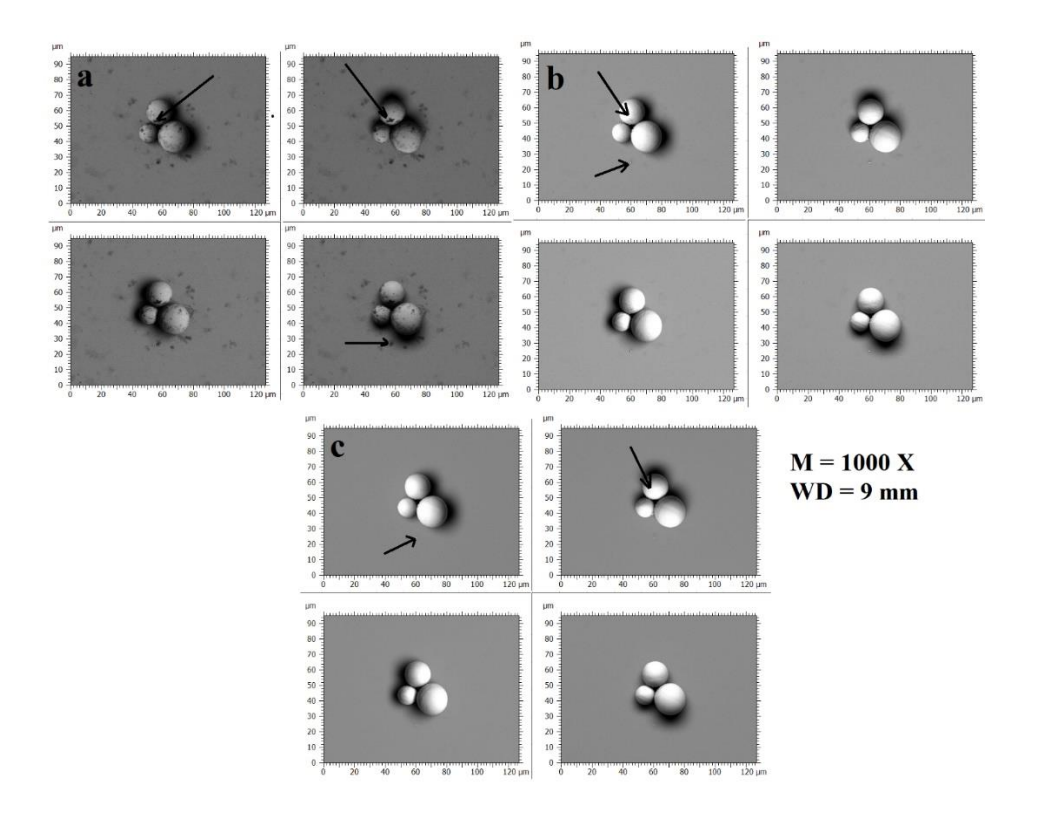


Figure 3-5 Backscattered electron images taken by 4-Q BSE detector at different accelerating voltage; a) 3 kV, b) 10 kV, and c) 20 kV.

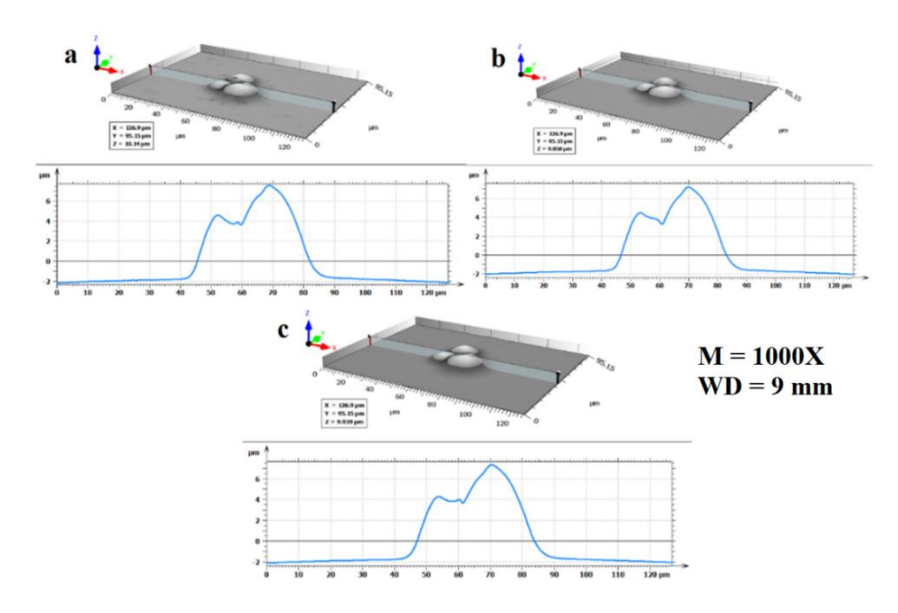


Figure 3-6 3D digital reconstructed image along with profile at different accelerating voltage; a) 3 kV, b) 10 kV, and c) 20 kV.

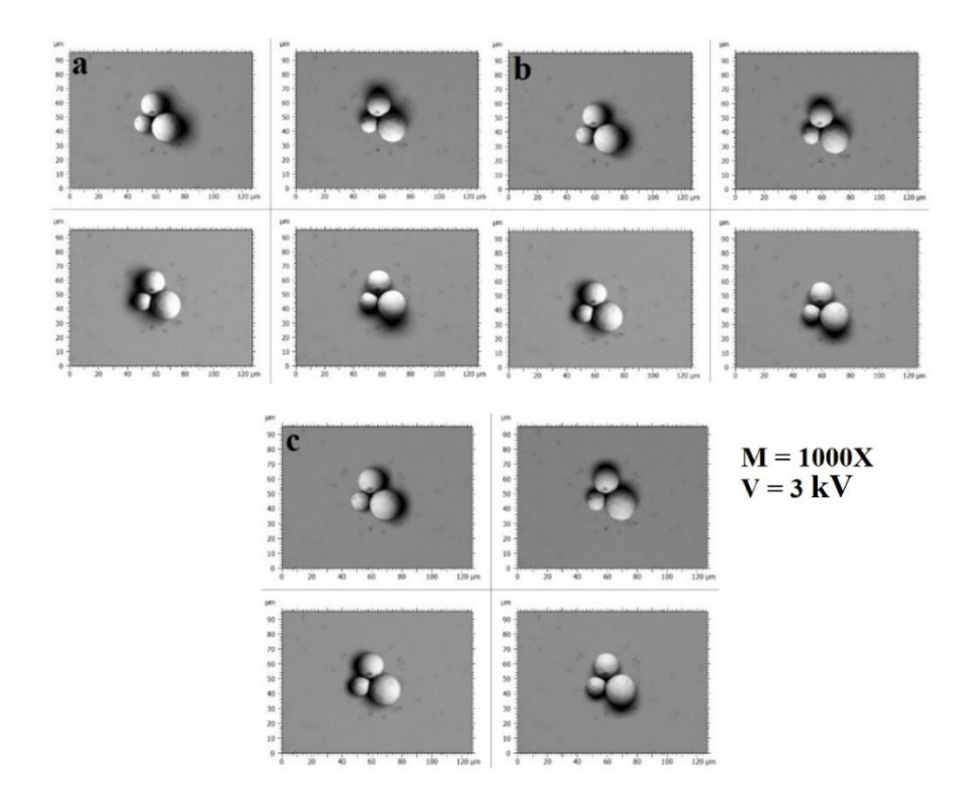


Figure 3-7 Backscattered electron images taken by 4-Q BSE detector at different working distance; a) 7 mm, b) 9 mm, and c) 11 mm.

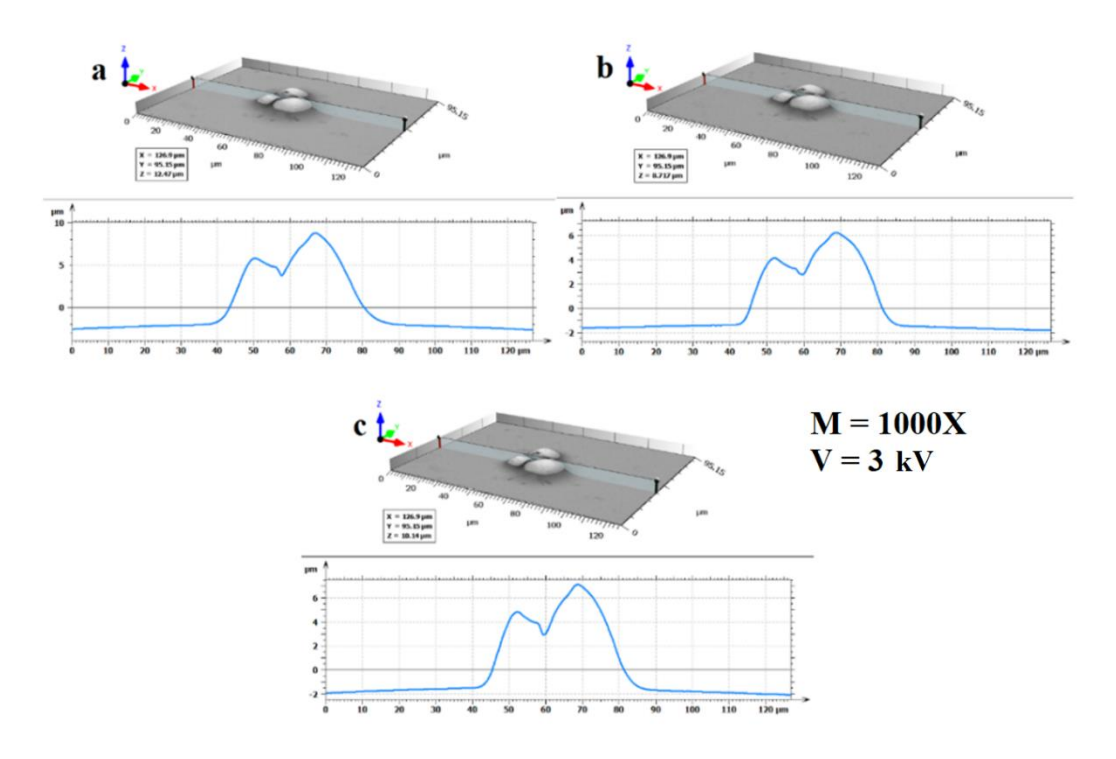


Figure 3-8 3D digital reconstructed image along with profile at different working distance; a) 7 mm, b) 9 mm, and c) 11 mm.

Figure 3.9 shows the value of the relative radius as a function of magnification (M), accelerating voltage (V), and working distance (WD) for different sizes of particles, separately. Based on the Relative Radius (Rr), Equation. 3.1 (a comparison operator for the size of any particles between 2D and 3D images), to obtain high accuracy of 3D reconstruction data we need to have small Relative Radius (Rr) for any 3D rebuilding. It can be seen from Figure 3.9 a that by increasing the magnification until 1000, the relative radius decreases. On the other hand, by increasing the magnification more than 1000X, significant change in the relative radius is not seen. Result showed that when the magnification is less than 1000X, the small features such as small particles (2.68 µm) cannot be seen even in the 2D images. Therefore, using these images for 3D reconstruction is not useful and makes a lot of error (Figure 3.9 a). One way to solve this problem could be using the low accelerating voltage in order to decrease the interaction volume. Regardless of the size of the spherical particles, as the accelerating voltage rises, the relative radius enhances, which is not appropriate for 3D reconstruction. Because the size of the interaction volume increases with the accelerating voltage (Equation 3.1) [18]. In this situation, signals (BSE) will come from deeper inside of the sample and consequently, the resolution of small features on the surface will decrease. Therefore, at low accelerating voltage, the interaction volume is small and close to the surface and subsequently, obtaining more signals to produce a high-resolution image is possible. Moreover, the experimental results showed that reducing the accelerating voltage more than 3 kV, would outcome in disruptive results due to losing signals without enough energy to reaching the surface (Figure 3.9 b). Then, Figure 3.9 b shows that when the accelerating voltage increases from 3 to 20 kV, Rr (which accounts for amount of error) increases form the range of 0-5% to the range of 10-15%, which is not appropriate for a 3D reconstruction. On the other hand, Figure 3.9 c displays that the relative radius declines as the working distance increases, but larger working distance causes the relative radius to worsen.

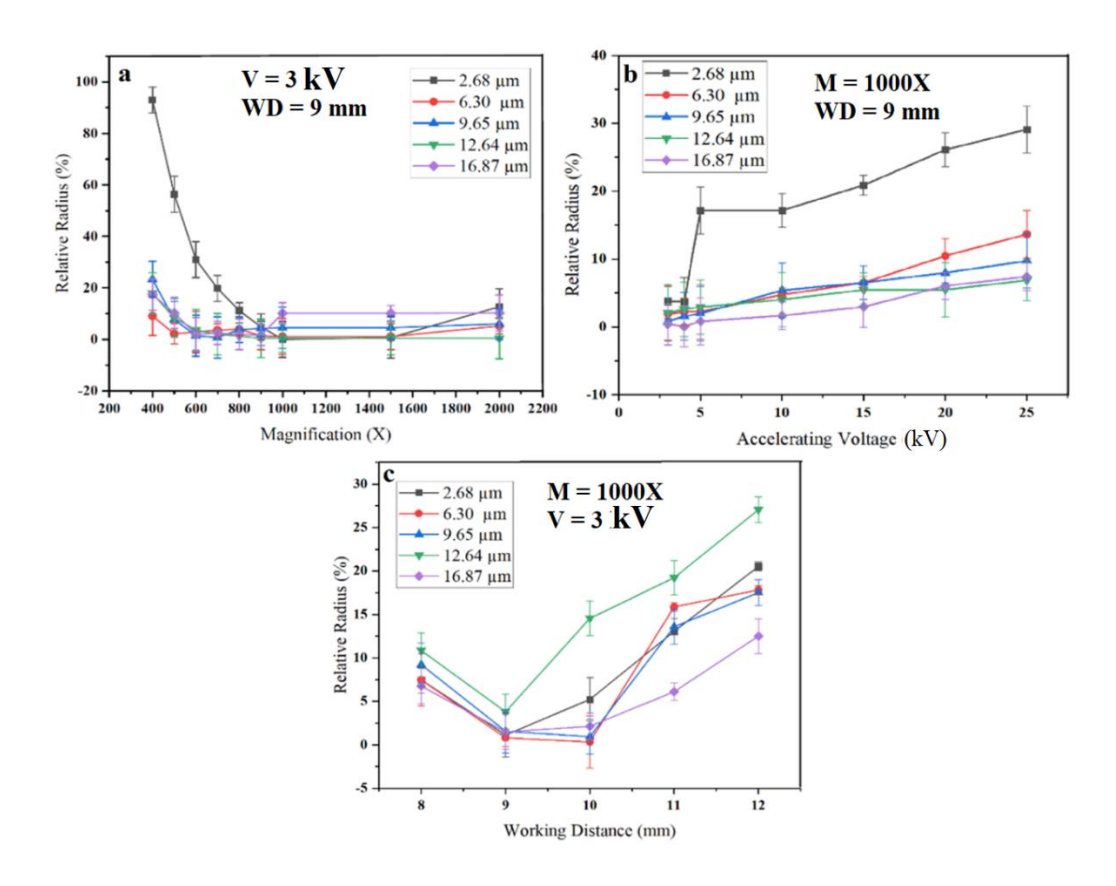


Figure 3-9 Relative radius versus; a) magnification, b) accelerating voltage, and c) working distance (Each graph represents one particle).

3. 5. Discussion

It was observed (Figure 3.4 and Figure 3.9 a) that by increasing the magnification to 1000, the relative radius declines thereby increasing quality of 2D images increases. However, by increasing magnification over 1000X, there is no significant improvement on the quality of 2D images and the relative radius. This behavior can be explained by the size of the pixels at any image. For any combination of SEM parameters, there is always a threshold contrast below which features of the specimen will not be visible. This threshold contrast depends on the relative size and shape of the feature of interest. The visibility of large objects and extended linear objects persists when small objects have dropped below the visibility threshold. That is, at low magnification the size of the pixel increases. Each pixel represents a unique sampling of specimen features and properties, provided that the signal(s) collected are isolated within the area represented by that pixel [18]. Therefore, in low magnification (M < 1000X), the specimen features and properties of specimen cannot be seen and as a result, the relative radius is too large. In addition, this trend worsens for features and properties of the specimen which are very small (Ti-6Al-4V particle with 2.68 µm

radius) in low magnification. Form these curves (Figure 3.9 a), the relative radius, and hence the accuracy of 3D images produced, is a strong function of the magnification of the taken picture and these effects must be included in the digital 3D reconstruction method.

Observation showed that (Figure 3.6 and Figure 3.9 b), regardless of the size of the spherical particles, as the accelerating voltage rises, the relative radius enhances, which is not appropriate for 3D reconstruction. The size of the interaction volume increases rapidly as the accelerating voltage increases [18]. In this situation, (BSE) signals will come from deeper inside of the sample and consequently, the resolution of small features on the surface will decrease. Therefore, at low accelerating voltage, the interaction volume is small and close to the surface and subsequently, obtaining more signals to produce a high-resolution image is possible. Moreover, the experimental results showed that by dropping the accelerating voltage more than 3 kV, would result in a disruptive outcome due to losing signals without enough energy in reaching the surface. Note that this is true for a thermionic gun due to the spherical aberration, but this might not be true with a FE-SEM.

Figure 3.8 and Figure 3.9 c display the behavior of 3D digital reconstruction method and relative radius when the working distance changes. There are two scenarios; first, for high depth of field, the largest working distance is needed; and second, for high-resolution mode, the smallest working distance is needed [18]. When considering high resolution, as well as, high depth of field, necessary to obtain high-quality image with more features, the behavior of the curves (see Figure 3.9 c) is sensible. More specifically, reaching the high depth of field, requires the largest working distance. On the other hand, high resolution requires the smallest working distance. The largest working distance is mandatory if we want to have a high depth of field. On the other hand, the smallest working distance is necessary if we need high resolution. As a result, the pattern of the curves (see Figure 3.9 c) makes sense. Note that the increase of the working distance more than the optimum range (9-10 mm) causes a decrease in the resolution.

3. 6. Conclusion

The present study was aimed to identify the optimal and most influential SEM parameters on the accuracy of the 3D digital reconstruction method which is under development. Various combinations of processing parameters were considered to evaluate the relative importance of parameters. It was observed that the working distance is a significant influential parameter in the digital 3D rebuilding method via SEM images. The best condition was obtained when the working distance was between 9 to 10 mm. It was found that by increasing the magnification to 1000X, the quality of 2D images which is important for 3D digital reconstruction, improved. However, for magnifications over 1000X, not only is there no significant improvement in the quality of 2D images, but it can reduce the scan size. From our observations, as the accelerating voltage increases (more than 3 kV), the appearance of the small feature in the 2D images decreases due to the size of the interaction volume, which is not appropriate for 3D reconstruction. SEM parameters including magnification at 1000X, accelerating voltage at 3 kV, and working distance at 9 mm have been found to be the optimal parameters for the specific geometry of our SEM with a BSE detector located on top of the sample surface. It must be noted though that due to varying detector – pole piece distances available in commercially available SEMs, these optimum values may vary slightly and may be optimized as well for each instrument.

3. 7. Acknowledgments

This research was supported by the MEDA Award from McGill University and Aluminum Research Centre-REGAL. We would like to thank them. We are also immensely grateful to Mr. Giacomo Daniel Di Silvestro (PhD student at McGill University) for his comments on an earlier version of the manuscript.

3. 8. References

- González-Velázquez, J.L., Fatigue Fracture, in Fractography and Failure Analysis. 2018,
 Springer. p. 71-95.
- 2. Moons, T., L. Van Gool, and Vergauwen, M., 3D reconstruction from multiple images part 1: Principles. Foundations and Trends® in Computer Graphics and Vision, 2010. 4(4): p. 287-404.
- 3. Arsalan Soltani, A., et al. Synthesizing 3d shapes via modeling multi-view depth maps and silhouettes with deep generative networks. in Proceedings of the IEEE conference on computer vision and pattern recognition. 2017.
- 4. Samak, D., Fischer, A., and Rittel, D., 3D reconstruction and visualization of microstructure surfaces from 2D images. CIRP annals, 2007. 56(1): p. 149-152.
- 5. Jessop, C., et al., 3D characterization of rolling contact fatigue crack networks. Wear, 2016. 366: p. 392-400.

- 6. Shyam, A. and Milligan, W., Effects of deformation behavior on fatigue fracture surface morphology in a nickel-base superalloy. Acta Materialia, 2004. 52(6): p. 1503-1513.
- 7. Flores, R.L., et al., The technique for 3D printing patient-specific models for auricular reconstruction. Journal of Cranio-Maxillofacial Surgery, 2017. 45(6): p. 937-943.
- 8. Tafti, A.P., et al., Recent advances in 3D SEM surface reconstruction. Micron, 2015. 78: p. 54-66.
- 9. Oliensis, J. and Werman, M., Structure from motion using points, lines, and intensities. in Proceedings IEEE Conference on Computer Vision and Pattern Recognition. CVPR 2000 (Cat. No. PR00662). 2000. IEEE.
- 10. Martišek, D., 3D reconstruction of the surface using a standard camera. Mathematical Problems in Engineering, 2017. 2017.
- 11. Torres, J., et al. 3D Digitization using structure from motion. in CEIG-Spanish Computer Graphics Conference. 2012.
- 12. Zolotukhin, A., Safonov, I., and Kryzhanovskii, K., 3D reconstruction for a scanning electron microscope. Pattern recognition and image analysis, 2013. 23(1): p. 168-174.
- 13. Limandri, S., et al., 3D scanning electron microscopy applied to surface characterization of fluorosed dental enamel. Micron, 2016. 84: p. 54-60.
- 14. Tafti, A.P., et al., 3DSEM++: Adaptive and intelligent 3D SEM surface reconstruction. Micron, 2016. 87: p. 33-45.
- 15. Yan, S., Adegbule, A., and Kibbey, T.C., A hybrid 3D SEM reconstruction method optimized for complex geologic material surfaces. Micron, 2017. 99: p. 26-31.
- 16. Eulitz, M. and Reiss, G., 3D reconstruction of SEM images by use of optical photogrammetry software. Journal of structural biology, 2015. 191(2): p. 190-196.
- 17. Pouchou, J.-L., et al., 3D reconstruction of rough surfaces by SEM stereo imaging. Microchimica Acta, 2002. 139(1): p. 135-144.
- 18. Goldstein, J.I., et al., Scanning electron microscopy and X-ray microanalysis. 2017: Springer.
- 19. Underwood, E.E., Quantitative fractography, in Applied metallography. 1986, Springer. p. 101-122.

- 20. Carli, L., et al., Uncertainty evaluation for three-dimensional scanning electron microscope reconstructions based on the stereo-pair technique. Measurement Science and Technology, 2011. 22(3): p. 035103.
- 21. Hemmleb, M., et al. 3D surface reconstruction with segmented BSE detector: New improvements and application for fracture analysis in SEM. in European Microscopy Congress 2016: Proceedings. 2016. Wiley Online Library.
- 22. Borzunov, A., et al., 3D surface topography imaging in SEM with improved backscattered electron detector: Arrangement and reconstruction algorithm. Ultramicroscopy, 2019. 207: p. 112830.

Chapter 4. Study of the Peak to Background (P/B) Method Behavior as a Function of Take-Off Angle, Tilt Angle, Particle Size, and Beam Energy

The Peak to Background (P/B) is one of the candidate models for quantitative characterization of rough surface. Based on this method, the P/B is constant at any location on the non-flat surface and that this ratio is the same as that of a bulk material of the same composition having a flat surface. By assuming that this proposal is correct, it is possible to convert rough sample intensity data into the intensity values measured for a flat sample of the same composition and thereby using the conventional quantitative analysis methods already mentioned. However, in this chapter, the behavior of the P/B as a function of different parameters such as take-off angle, tilt angle, particle size, and beam energy are investigated using the Monte Carlo model to show "Does the efficiency of this method is enough for microanalysis for particles or non-flat surfaces?".

• This chapter has been published as: S. M. Bayazid*, Y. Yuan, R. Gauvin, Study of the Peak to Background (P/B) Method Behavior as a Function of Take-Off Angle, Tilt Angle, Particle Size, and Beam Energy, Scanning 2021, (2021) 8070721

4. 1. Abstract

Monte Carlo simulations were performed to investigate the behavior of the Peak to Background ratio (P/B) of particles on substrate as a function of different variables such as take-off angle, tilt angle, particle size, and beam energy. The results showed that the P/B highly depends on the beam energy, the size of particles, and the composition of the substrates. Results showed that the rate of intensity reduction of the peak is less than the background for a high tilt angle, and thereby the P/B increases at a high tilt angle. It was shown that by increasing the take-off angle, the P/B initially reduces and then reaches a plateau. Results showed, the P/B highly depends on particle size. Analyses showed that by moving the electron beam from the center to the side of the particle, the P/B increases. Finally, the spherical particles have higher sensitivity of the P/B to the beam position than the cubical particles.

4. 2. Introduction

Converting the X-ray intensity into elemental concentration for non-flat samples has been challenging for decades. Conventional methods such as ZAF or $\varphi(\rho z)$ methods are valid for specimens with homogeneous composition and flat surfaces [1]. Some problems with the analysis of non-flat specimens are described in the following. First, the undefined incidence angle of electrons makes it difficult to model both the backscattered electrons and the depth distribution of the generated X-rays. Second, the take-off angle, and the average depth of the generated X-rays are not well specified for non-defined geometries, thus the absorption path length can change considerably. Moreover, some side-scattering might happen in the case of the particle's analysis due to the geometry factor. Finally, for small particles, the randomization process of electrons has not been completed before they leave the particles. Therefore, the anisotropy in the bremsstrahlung X-ray may not be negligible [2-4].

Several methods including the Armstrong model [5], the Peak to Background (P/B) method [6, 7], and the Monte Carlo simulations [1] have been proposed to overcome this matter. Armstrong et al. [5] developed analytical approximations and calculated X-ray corrections iteratively in a similar manner to the ZAF method for the homogeneous composition. Armstrong's model is based on the classification of particles by shape. However, the computation of the multi-dimensional integrals required can be time-consuming [6]. Moreover, the dependency of the Armstrong model on the particle's shape limits its application in the characterization of non-flat surfaces [2]. On the other hand, in the case of rough surfaces, the P/B method [6-8] was proposed as a quantitative model, which is an extension of the Marshall-Hall model [9, 10] for the correction of mass loss in beam-sensitive materials. Declared by this method, the P/B is constant at any location on the rough surface, and that this ratio is the same as that of bulk material of the same composition having a flat surface.

However, using Monte Carlo simulations, Gauvin et al. [11] showed that the P/B is not constant for the rough surfaces. Gauvin demonstrated that the P/B has some weaknesses. For instance, the assumption that the P/B is independent of the specimen non-flat is not strictly correct since the ionization cross-sections and the Bremsstrahlung cross-sections are not the same. Rez et al. [2] indicated that the P/B increases with increasing overvoltage, therefore the voltage dependence to the P/B ratio means that it is not truly independent of geometry. Researchers [4, 12] showed that

the most likely source of error in the P/B method is the uncertainty in the calculation of the continuous spectrum intensity. However, Heckel et. al [13] pointed that the influence of statistical errors of the continuous spectrum counts can be diminished by prolonging the measuring times. Some concerns in using the P/B for quantitative characterization of non-flat surfaces have still remained for decades. In this paper, the behavior of the P/B as a function of different parameters such as take-off angle, tilt angle, particle size, and beam energy are investigated using the Monte Carlo model to show "Does the efficiency of this method of analysis for particles or rough surfaces is enough?".

4. 3. Method

To calculate P/B ratios for different conditions, various Monte Carlo simulations were performed using the Monte Carlo program described in reference[14]. MC X-Ray is a new Monte Carlo program that is an extension of the Casino [15, 16] and Win X-Ray [17]. It does X-ray microanalysis from the simulation of electron scattering in solids of different types of geometries. Scatterings are built based on an accidental process where electrons are simulated using a forward scattering random walk. The methodology, calculations, and physics of the program were described in reference [14]. The simulations were performed for spherical particles of Al deposited on substrates (C, Ti, Ag, and Au). In this work, the beam diameter was equal to 10 nm and 100000 electrons were used to simulate electron trajectories in order to compute X-ray emission for particles. The main variables used in these simulations were beam energy, tilt and take-off angles, particle size, particle's shape (sphere and cubic) and the composition of the substrate. The P/B was calculated for the total number of peak counts to the number of background counts under the peak (Figure 4.1).

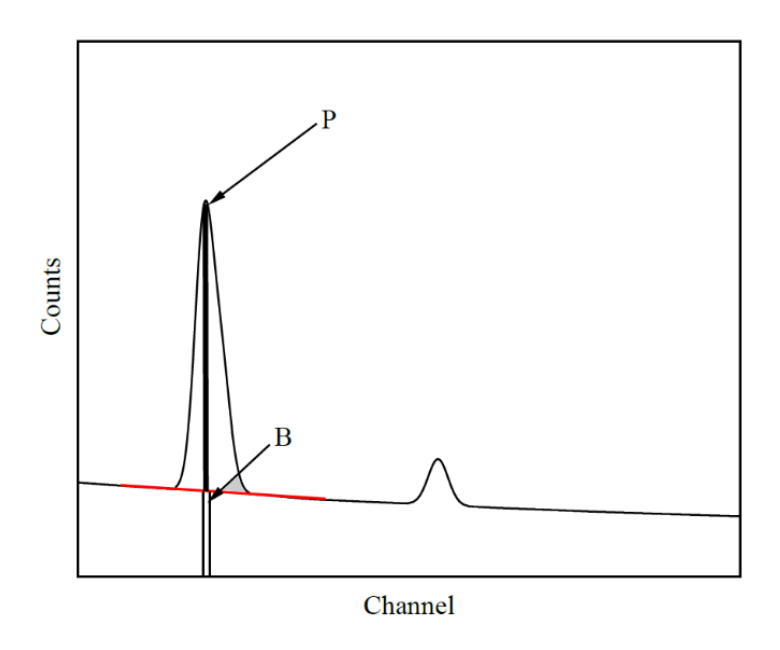


Figure 4-1 Definition of the P/B ratio. P is the net intensity of the characteristic line (e.g. $K\alpha$ line) an B is the background intensity at the line energy.

4. 4. Results

4. 4. 1 Beam energy

Figure 4.2A shows the variation of the peak intensity for Al-K α as a function of beam energy when the beam is located at the center of spherical particles. The tilt and take-off angles were set at 0 and 40 degrees, respectively. The peak intensity increases with the beam energy, goes to a maximum value depending on the size of the particle and then decays when the beam energy is further increased. Results show that the maximum value of the peak intensity depends on the size of the particle. The bigger the size of the particle, the higher the maximum value of the peak intensity. On the other hand, the intensity of the background (continuum x-ray) continuously increases as the beam energy increases. However, there is a small reduction in the background intensity when the beam energy is larger than 27 keV. The background intensity is a function of the beam energy according to Kramers [18]. As the beam energy increases, the maximum continuum energy increases. Note that at certain beam energy, a small particle has higher background intensity in comparison with a big particle (Figure 4.2B) because of the electron transition phenomenon [4].

The peak and background intensities for all particles are the same as long as the beam energy is less than 5 keV. Figure 4.2C indicates that not only the P/B changes with the size of the particle but also it varies with beam energy. Regardless of the particle size, the value of the P/B rises with beam energy, goes to a maximum, and then decays to a plateau. It also shows that the bigger the size of the particle, the higher the P/B value. Figure 4.2D shows that the P/B depends on the substrate that the particle deposited on it. When the beam energy is more than 10 keV, the higher the atomic number of the substrate, the lower the P/B. For beam energies more than 10 keV, the electron range increases, and the X-rays are generated inside the substrate as well, therefore this phenomenon could affect the P/B.

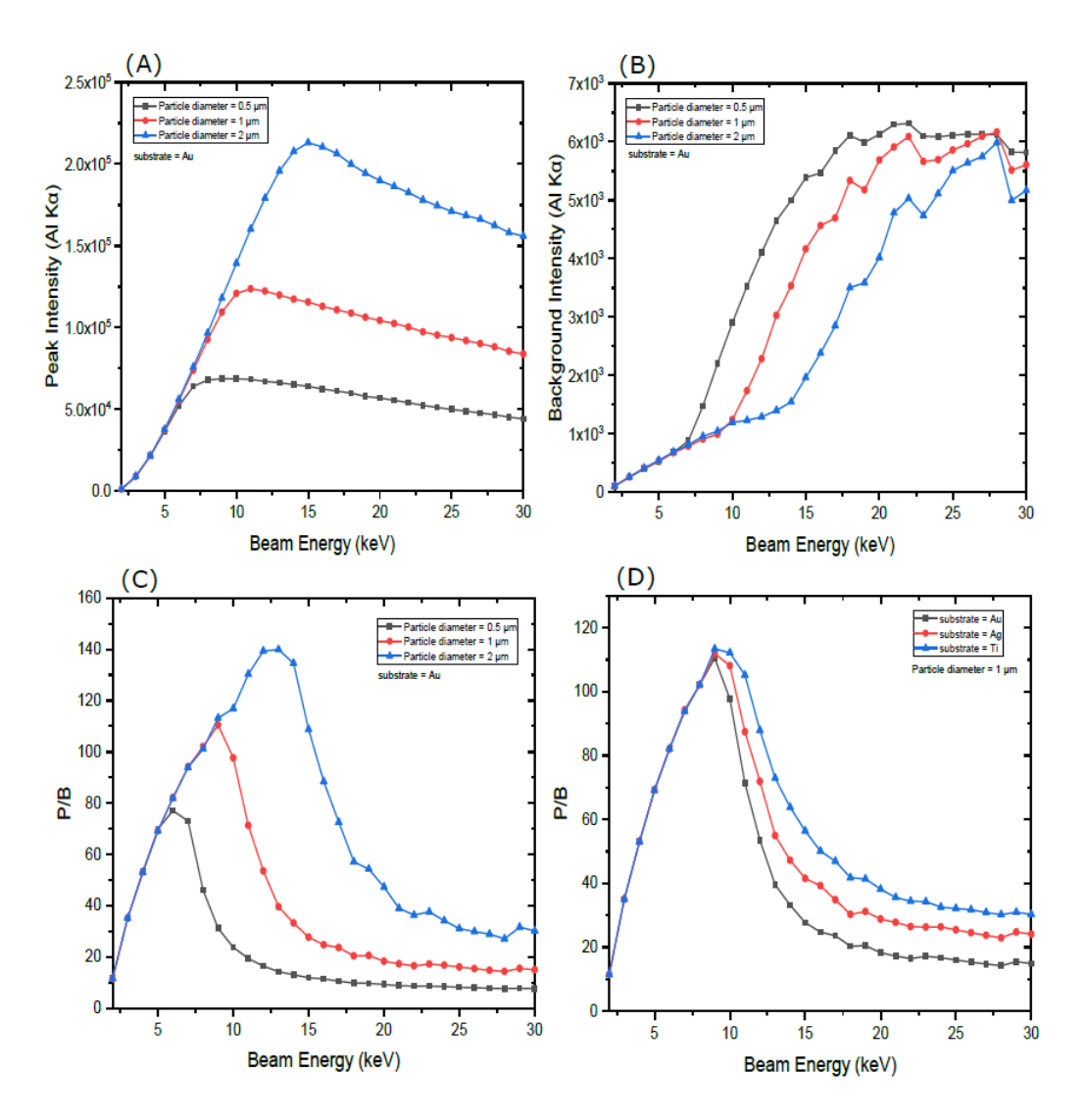


Figure 4-2 Variation of peak (Al-Kα line) intensity, background (continuum X-ray) intensity, and the P/B as a function of beam energy.

4. 4. 2 Tilt angle

Although the peak intensity and background intensity decrease as the tilt angle increases, the P/B is almost stable from 0 to 60 degrees of tilting. It means that the rate decreasing for both intensities is nearly the same. However, the P/B increases as the tit angle is larger than 60 degrees (see Figure 4.3). Results show that the P/B is roughly stable as a function of tilt angle when the beam energy is low (5 keV). On the other hand, for high beam energies (20 keV) the P/B grows from roughly 38 to 80 when the tilt angle changes from 60 to 80 degrees.

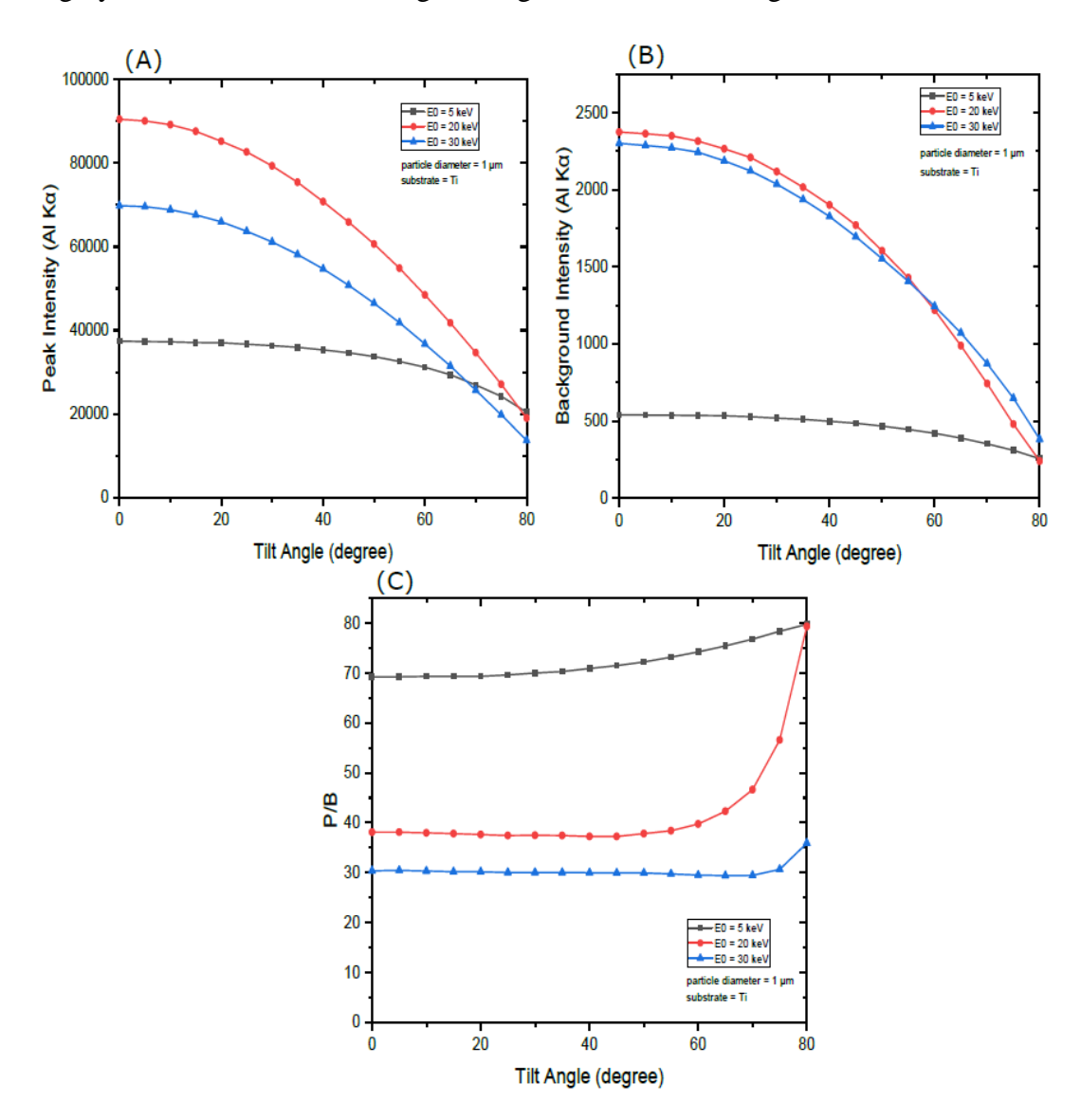


Figure 4-3 The peak intensity, background intensity, and the P/B as a function of tilt angle.

Figure 4.4 shows the variation of the f ratio given by $(I_{Max} \ Al \ K\alpha) / (I_{Max} \ Al \ K\alpha + I_{Max} \ Au \ M\alpha)$ as a function of tilt angle. Results show that the f ratio decreases with increasing tilt angle for the beam energy of 20 keV, goes to the minimum value at 70 degrees, and then increases again by increasing the tilt angle. This trend is similar for the beam energy of 30 keV but the minimum value of the f ratio happens at 75 degrees.

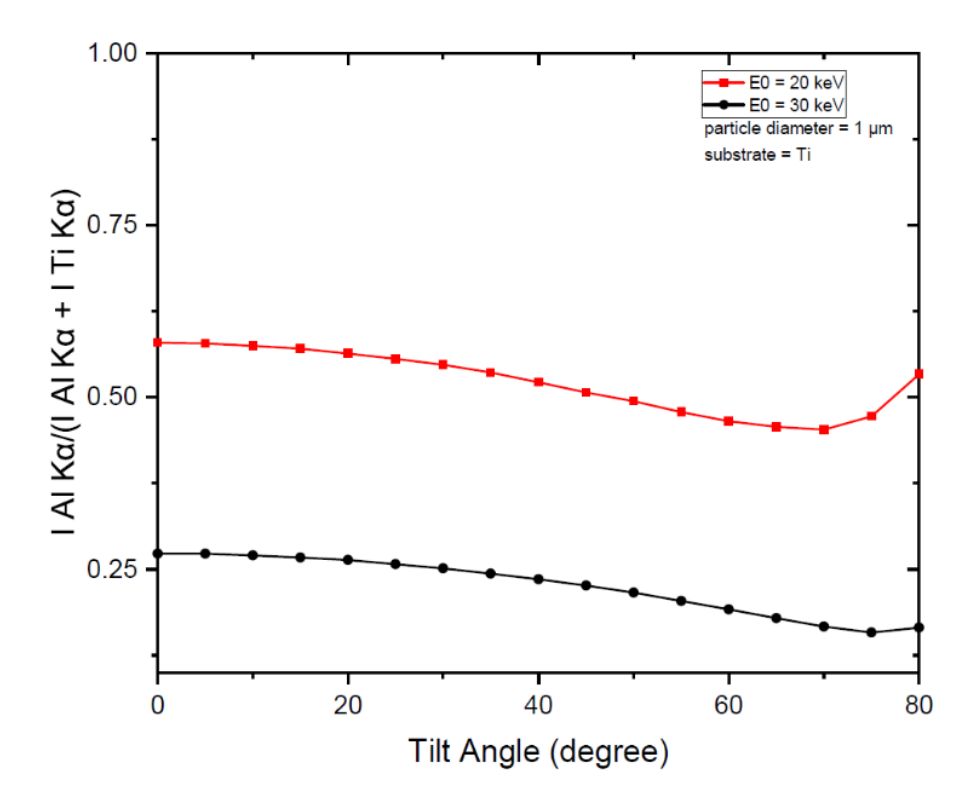


Figure 4-4 Variation of f ratio given by (IMax Al K α) / (IMax Al K α + IMax Au M α) as function of tilt angle (Al deposited on Ti).

4. 4. 3 Take-off angle

Figure 4.5 shows the variation of the P/B for Al-K α as a function of the take-off angle. The beam diameter and tilt angle were 10 nm and 0 degrees, respectively. It is shown that the P/B does not change with the take-off angle at low beam energy (5 keV). However, for high beam energy values (20, 30 keV), the P/B decreases as the take-off angle increases. Figure 4.5 shows that the P/B exponentially decreases when the take-off angle increases from 0 to 85 degrees. The variation of R ratio as a function of take-off angle is shown in Figure 4.6. Results show that the variation of the f ratio when the take-off angle increases are higher for small particles. For example, the variation of the R ratio when the take-off angle changes from 0 to 85 degrees for small particles (5

nm) is 51%; however, for a bigger particle ($1\mu m$), the f ratio variation is 10%. The f ratio for small particles (5 nm) decreases sharply by increasing the take-off angle, goes to a minimum, and then increases to a plateau. However, for particles with 1 μm diameter, the f ratio decreases smoothly and continuously by increasing the take-off angle and reaches a plateau. Regardless of the particle size and the take-off angle, the higher the beam energy, the lower the f ratio.

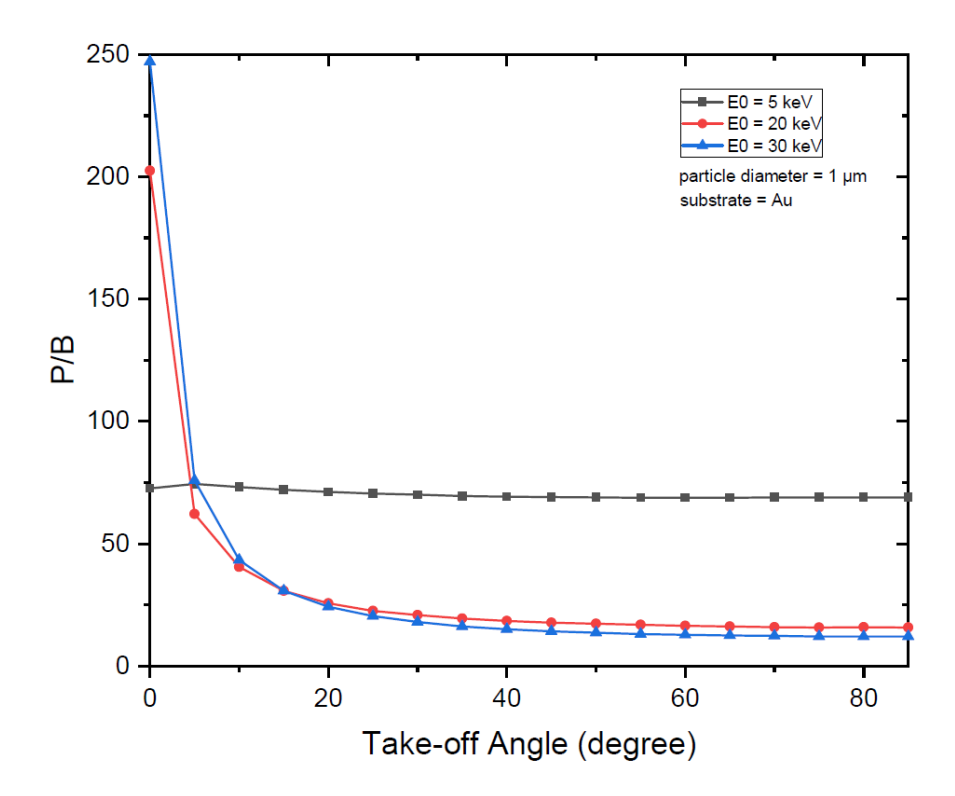


Figure 4-5 The P/B of Al-K α as a function of take-off angle.

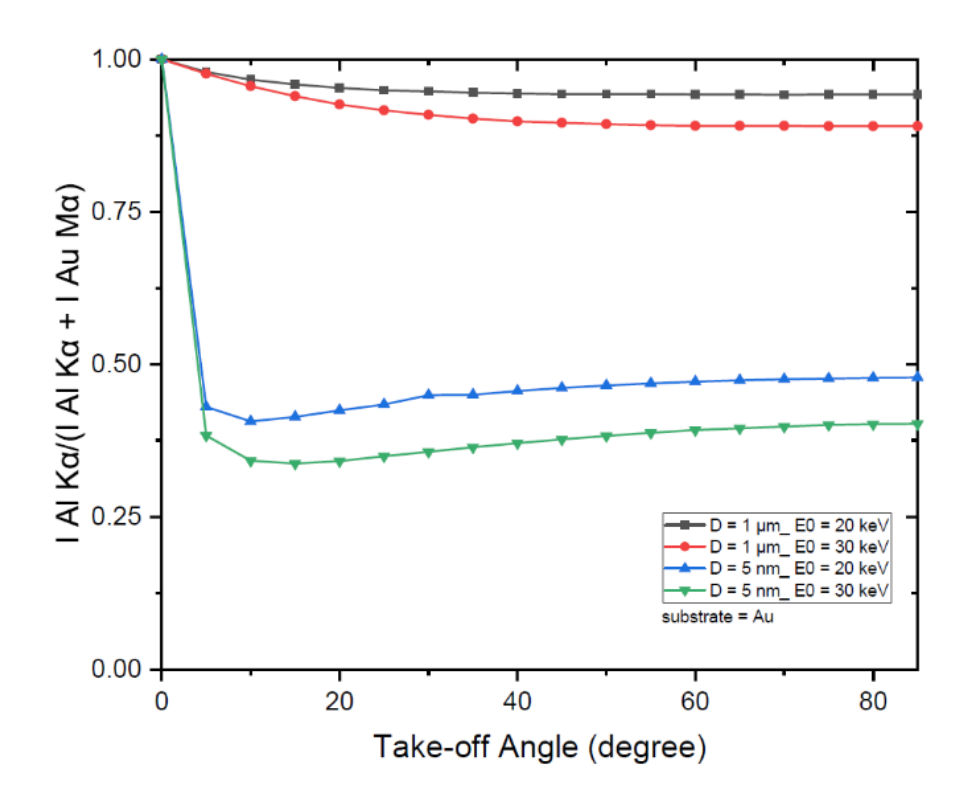


Figure 4-6 Variation of f ratio given by (IMax Al K α) / (IMax Al K α + IMax Au M α) as function of take-off angle (Al particle deposited on Au).

4. 4. 4 Particle size

Figure 4.7A shows the variation of the P/B and f ratio as a function of particle size (D, particle diameter) normalized by X-ray emitted range (X_e) at different beam energies. For a certain beam energy, when the size of the particle increases, the P/B increases monotonically and then goes to the plateau. The higher the beam energy, the plateau happens at a bigger particle diameter. For small particles, the higher the beam energy, the less the P/B due to the size of the interaction volume. The R ratio increases as the particle size increases (see Figure 4.7B). At any particle size, the lower the beam energy, the higher the f ratio.

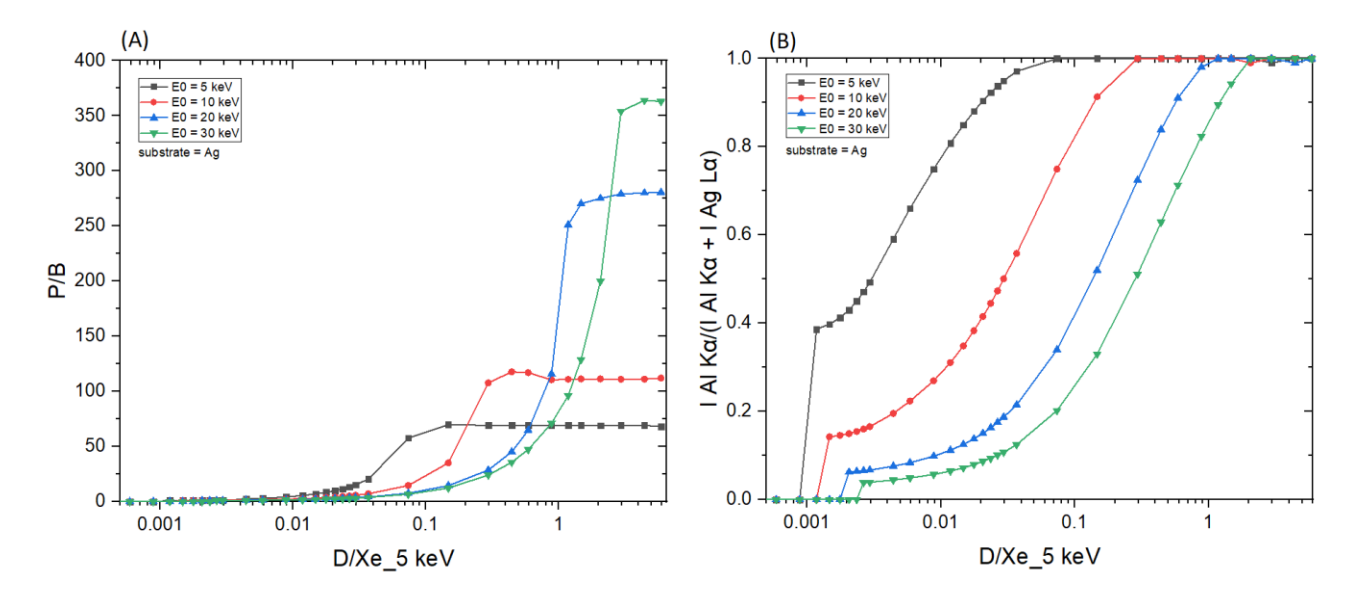


Figure 4-7 Variation of the P/B, and f ratio as function of D/Xe (5 keV) for Al K α ; Xe is the range of emitted X rays for the bulk sample, in this case at 5 keV.

Figure 4.8 shows that when the beam position is moved from the center of the particle (0) to the left side (in this case), the P/B is constant until 100 nm for both cubical and spherical particles. However, from this point (100 nm) all the way to the end, the P/B increases for bath particles. Results show that the P/B for a spherical particle is more sensitive to the beam position than the cubical particle because the variation of the P/B in the case of spherical particle is more than cubical one. It could be concluded that the P/B depends on the particle shape and beam position.

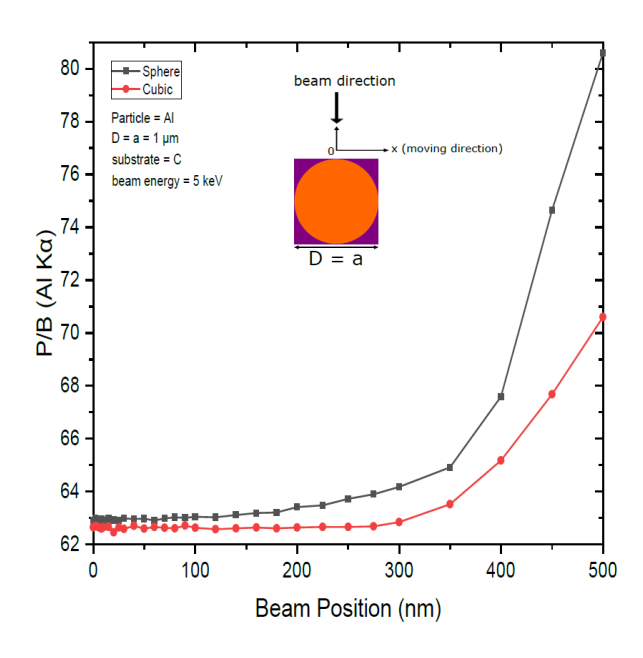


Figure 4-8 Variation of the P/B as a function of beam position.

4. 5. Discussion

The presented results show that the P/B is not constant on a non-flat surface. Figures 4.2C and 4.2D indicated that not only the P/B highly depend on beam energy, but it relies on substrates for chemical characterization of particles. What is clear is that the P/B is less sensitive to the size of particles at low beam energy (less than 5 keV). It means that the size of particles at low beam energy (less than 5 keV) does not affect the P/B. However, when the beam energy is greater than 5 keV, the P/B is not the same for all particles (0.5, 1, 2 μm). This behavior can be explained via interaction volume. For low beam energies (less than 5 keV), the interaction volume is a part of particles volume (0.5, 1, 2 µm), however, when the beam energy increases, the interaction volume increases, and it can cover all over the small particles. Because the characteristic and Bremsstrahlung cross-sections [2] behave very similarly at high beam energies, thus the P/B tends to a constant at high beam energies. On the other hand, at high beam energies, the P/B changes when the substrate of the particle differs (Figure 4.2D). Because at high beam energy the interaction volume is too big and includes some part of the substrate. As a result, depending on the atomic number of the substrates, the backscattering affects the P/B value. Although it has been shown by Rez et al. [2] that the tilting does not affect the P/B in the range of 0 to 40 degrees, but our results showed (Figure 4.3C) that the P/B changes for high tilt angles (60 to 80 degrees), especially at high beam energies. At high tilt angles (60 to 80 degrees), the number of electrons that penetrate to the particle to generate x-rays reduce, thus the peak and the background intensities decrease as well. But as Figures 4.3A and 4.3B show, the rate of intensity reduction of the peak is less than the background, therefore the P/B increases at a high tilt angle.

The variation of the f ratio with tilt angle (see Figure 4.4) is in agreement with the proposed assumption. Figure 4.5 showed that the take-off angle has a high impact on the P/B, especially at high beam energies, since the absorption path increases (if the particle size and the X-rays position remains the same) as the take-off angle goes from 0 to 40 degrees for a spherical particle. However, at low beam energy (5 keV), the take-off angle does not affect the P/B. Because the interaction volume is very small in comparison with the situation when the beam energy is 30 keV. Therefore, the absorption path is almost constant as the take-off angle changes. Moreover, increasing the take-off angle more than 40 degrees does not change the P/B. It could be explained that when the take-off angle is more than 40 degrees, the number of emitted X-rays that could reach to the detector

are very small and the geometry does not have big effect on the absorption path. Figure 4.7A showed that the P/B is affected by the particle size. Although Statham et al. [6] that the P/B is the same for particles with diameter 3 μm and 9 μm at beam energy of 20 keV . Nevertheless, our results showed that the P/B is not constant when the size of particles is changed between 1 to 5 μm at beam energy of 20 keV. At the beam energy of 5 keV, the P/B changes when the particle diameter goes from 1 to 500 nm. However, the P/B does not change for particles larger than 500 nm.

The problem with the quantitative microanalysis of particles is that electrons can be scattered from all sides of particles, so the generated x-rays depend on the size and shape of particles [6, 19]. On one hand, the characteristic X-ray generated within the particle is only a fraction of the X-ray generated in a bulk sample of the same composition, when particle sizes are below the interaction volume of the electrons [2]. On the other hand, the shape of a particle makes it very difficult to correctly consider the path of characteristic X-rays between their generation locations and the particle surface [6, 19]. Therefore, geometric factors impact the measured x-ray intensities and thereby the P/B, and the quantitative analysis of particles [2, 19, 20]. Another reason that shows the P/B highly depends on the geometry and the beam position was shown in Figure 4.8. Results showed that by moving from the center to the side of the particle, the P/B increases, this P/B boosting is more for the spherical particle than the cubical one. Therefore, it could be concluded that the P/B pertains to the geometry and the beam position. Similarly, Newbury [19] has reported that the intensity of a peak varies if the beam position is changed on the particle.

4. 6. Conclusion

The Peak to Background ratio can be affected by many factors. In this study, the P/B was analyzed while beam energy, tilt angle, take-off angle, and particle size were changing. It was shown that not only the P/B highly depend on beam energy and the size of particles, but it relies on substrates. Results showed that at a high tilt angle, the rate of intensity reduction of the peak is less than the background, therefore the P/B increases. Moreover, the tilting cannot affect the P/B at the range of 0 to 40 degrees. On the other hand, the take-off angle highly affects the P/B of the particles. The higher the take-off angle, the lower the P/B. The dependency of the P/B to the take-off angle increases when the beam energy increases. The effect of particle size at different beam energies on the P/B showed that the P/B is not constant when the size of particles is changed,

depending on the beam energy. More investigation showed that by moving from the center to the side of the particle, the P/B increases, this P/B enhancing is more for the spherical particle than the cubical one. It could be concluded that the P/B depends on the geometry and the beam position.

4. 7. Acknowledgments

Financial support from the Natural Science and Engineering Research Council of Canada (NSERC) and from the McGill MEDA Award is gratefully acknowledged.

4. 8. References

- 1. Gauvin, R., Quantitative X-ray microanalysis of heterogeneous materials using Monte Carlo simulations. Microchimica Acta, 2006. 155(1): p. 75-81.
- 2. Rez, P. and J. Konopka, Limitations in the use of the peak-to-background method for quantitative analysis. X-Ray Spectrometry, 1984. 13(1): p. 33-37.
- Giannuzzi, L.A., Scanning Electron Microscopy and X-Ray Microanalysis 4th Edition, Joseph I. Goldstein, Dale E. Newbury, Joseph R. Michael, Nicholas WM Ritchie, John Henry J. Scott, David C. Joy, Springer, 2018, 550 pp. ISBN: 978-1-4939-6674-5. Microscopy and Microanalysis, 2018. 24(6): p. 768-768.
- 4. Lábár, J.L. and S. Török, A peak-to-background method for electron-probe x-ray microanalysis applied to individual small particles. X-Ray Spectrometry, 1992. 21(4): p. 183-190.
- 5. Armstrong, J.T. and P.R. Buseck, Quantitative chemical analysis of individual microparticles using the electron microprobe. Theoretical. Analytical chemistry, 1975. 47(13): p. 2178-2192.
- 6. Statham, P. and J. Pawley, New method for particle X-ray Micro-analysis based on peak to background measurements, in Scanning electron microscopy/1978. Vol. I. 1978.
- 7. Statham, P., Measurement and use of peak-to-background ratios in X-ray analysis. Mikrochimica Acta, 1979. 8: p. 229-242.
- 8. Small, J., et al., The production and characterization of glass fibers and spheres for microanalysis. Scanning Electron Microsc, 1978. 1: p. 445-454.
- 9. Marshall, D. and T.A. Hall, A method for the microanalysis of thin films. X-ray Optics and Microanalysis, eds. Castaing R, Deschamps P, Philibert J.(Hermann, Paris), 1966. 374.

- 10. Hall, T., Some aspects of the microprobe analysis of biological specimens. Quantitative electron probe microanalysis, 1968(298).
- 11. Gauvin, R. and E. Lifshin, X-ray microanalysis of real materials using Monte Carlo simulations. Microchimica Acta, 2004. 145(1): p. 41-47.
- 12. Reed, S. Peak to background ratio in microprobe analysis. in Vth International Congress on X-Ray Optics and Microanalysis/V. Internationaler Kongreß für Röntgenoptik und Mikroanalyse/Ve Congrès International sur l'Optique des Rayons X et la Microanalyse. 1969. Springer.
- 13. Heckel, J. and P. Jugelt, Quantitative analysis of bulk samples without standards by using peak-to-background ratios. X-Ray Spectrometry, 1984. 13(4): p. 159-165.
- 14. Gauvin, R. and P. Michaud, MC X-ray, a new Monte Carlo program for quantitative X-ray microanalysis of real materials. Microscopy and Microanalysis, 2009. 15(S2): p. 488-489.
- 15. Hovington, P., D. Drouin, and R. Gauvin, CASINO: A new Monte Carlo code in C language for electron beam interaction—Part I: Description of the program. Scanning, 1997. 19(1): p. 1-14.
- 16. Drouin, D., et al., CASINO V2. 42—a fast and easy-to-use modeling tool for scanning electron microscopy and microanalysis users. Scanning: The Journal of Scanning Microscopies, 2007. 29(3): p. 92-101.
- 17. Gauvin, R., et al., Win X-ray: A New Monte Carlo Program that Computes X-ray Spectra Obtained with a Scanning Electron Microscope. Microscopy and Microanalysis, 2006. 12(1): p. 49-64.
- 18. Kramers, H.A., XCIII. On the theory of X-ray absorption and of the continuous X-ray spectrum. The London, Edinburgh, and Dublin Philosophical Magazine and Journal of Science, 1923. 46(275): p. 836-871.
- 19. Newbury, D.E., Quantitative electron probe microanalysis of rough targets: Testing the peak-to-local background method. Scanning: The Journal of Scanning Microscopies, 2004. 26(3): p. 103-114.
- 20. Goldstein, J.I., et al., Scanning electron microscopy and X-ray microanalysis. 2017: Springer.

Chapter 5. A Universal Equation of Geometrical Correction Factor for Quantitative Characterization of Spherical Particles

Quantitative microanalysis of a bulk sample using the ZAF method is very simple because there are excellent models for $\varphi(\rho z)$ curves and the computation of the absorption due to the flat surface is straightforward. Such models do not exist for particles. While X-Ray microanalysis can be a useful tool for initial characterization of particles, it is not quantitative because the geometry of particles presents problems that are not present in the microanalysis of a bulk sample. Therefore, to apply the conventional ZAF model for particles, some modification is needed by adding a geometrical correction factor (G). In this chapter, a Geometrical correction factor (G) as the fourth factor in the ZAF-method (ZAFG) for quantitative characterization of particles is introduced and analyzed while different SEM parameters are varied.

This chapter has been published as: S. M. Bayazid*, N. Brodusch, N. Dumaresq, R. Gauvin, A Universal Equation of Geometrical Correction Factor for Quantitative Characterization of Spherical Particles, Chemical Papers 2023, (submitted).

5. 1. Abstract

The derivation of a universal equation to calculate a Geometrical correction factor (G) as the fourth factor in the conventional ZAF method for quantitative characterization of spherical particles (NIST-K411 subtracted on Carbon) is introduced. Findings showed that the G factor as a function of $\frac{D}{X_e}$ is the best description of the model, where D is the diameter of particles, and X_e is the range of emitted x-rays in a bulk sample with the same chemical composition. An excellent agreement was observed with experimental data obtained from NIST-K411 standard particles. Results showed that as X_e becomes greater than D, the G factor decays exponentially regardless of the incident electron energy, the X-Ray lines, and chemical composition of particles. It was shown that when $\frac{D}{X_e} > 1$ for a particle, then G = 1. In this condition, the particle works as a bulk sample. Data indicated that the G factor only depends on $\frac{D}{X_e}$, neither the chemical composition nor the beam energy.

5. 2. Introduction

Quantitative microanalysis of particles is become important in science and technology [1]. Although X-Ray microanalysis can be a useful tool for preliminary characterization of particles, it is not quantitative because the geometry of particles introduces problems that are not present in the microanalysis of a bulk sample [2]. The problem with the quantitative microanalysis of particles is that electron-induced X-Rays can be emitted from all sides of a single particle, so the generated X-Rays depend on the size and shape of the particles [2, 3]. Moreover, the characteristic X-Ray generated within the particle is only a fraction of the X-Ray generated in a bulk sample of the same composition, when particle size is below the interaction volume of the electrons [4]. Furthermore, the shape of a particle makes it difficult to correctly consider the path of characteristic X-Rays between their generation locations and the particle surface (Absorption path) [2, 3] (see Figure 5.1). Therefore, as shown in Fig 1, the geometry of particles impacts the generated, emitted, or measured X-Ray intensities and thereby the quantitative analysis of particles and it is not possible to use the conventional ZAF method [3-5].

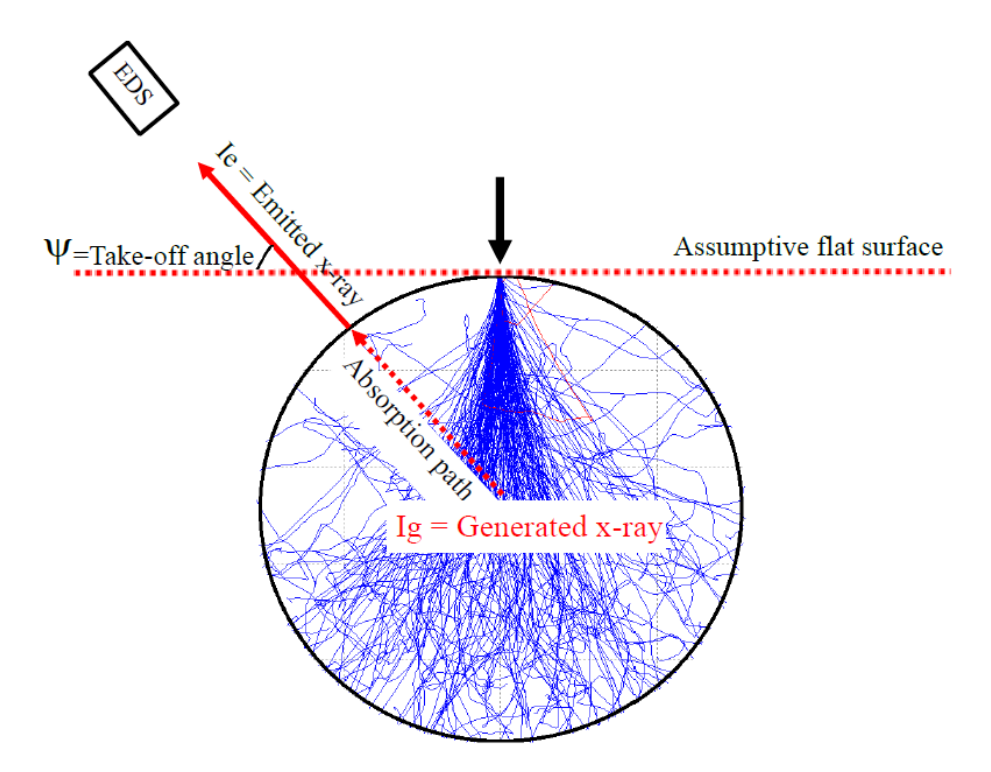


Figure 5-1 Effect of particle geometry on the generated, emitted X-Ray intensities, and the absorption path.

Several techniques have been proposed to perform quantitative X-Ray microanalysis for particles or non-flat surfaces. These techniques include normalization of the results that come from the conventional ZAF method [5], the Armstrong model [6] which is based on classification of particles by shape, the Peak to Background ratio (P/B) method [2, 7], and Monte Carlo simulations [8-14]. Although the P/B ratio has distinct advantages, it also has drawbacks. Gauvin et al. [11] showed that the assumption that the P/B is independent of the sample non-flat is not strictly correct since the ionization cross-sections and the Bremsstrahlung cross-sections are not the same for rough surfaces. Alternatively, it is commonly accepted that the Monte Carlo model is ideal for quantitative characterization of particles [8-16]. For instance, Monte Carlo simulations have demonstrated that they could improve the accuracy of quantitative X-Ray microanalysis of nonflat surfaces [11]. However, although the Monte Carlo technique possesses several disadvantages, its time-consuming [2, 17] outweighs the benefits. Nevertheless, machine learning could speed up the Monte Carlo modeling by a factor of 10000 [18, 19]. Therefore, Monte Carlo modeling along with machine learning looks like the best choice to develop quantitative schemes to perform x-ray microanalysis of non-flat surfaces. In this study, using Monte Carlo simulations, a Geometrical correction factor (G) as the fourth factor in the ZAF-method (ZAFG) for quantitative characterization of particles is introduced and computed as a function of different SEM parameters. Using the new ZAFG method makes it possible to quantify particles even without using Monte Carlo simulation once the G-factor has been computed using Monte Carlo modelling.

5. 3. Description of the geometrical correction factor (G)

The Monte Carlo simulations were performed using the MC-X-Ray software described in references [15, 20]. It computes generated and emitted X-Rays from the simulation of electron scattering in solids for different types of specimen geometries. Scattering is simulated using random numbers and total/partial elastic cross sections with energy losses computed with the continuous slowing down approximation [15, 20]. Figure 5.2 shows the geometries used in this program to simulate X-Ray emission from spherical particles of different sizes on different substrates. In this work, 100000 electron trajectories were used to compute X-Ray emission from particles and the variables used in these simulations were beam energy, particle size, the chemical composition of the particulate and the substrate.

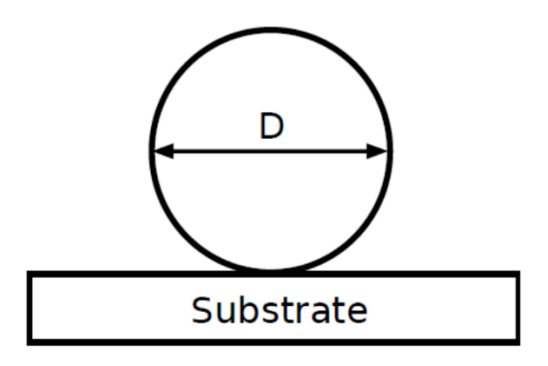


Figure 5-2 Geometry used to simulate particle on substrate.

Quantitative microanalysis of a bulk sample in the ZAF formalism is described by Equation (5.1) [5]:

$$\frac{c_i}{c_{(i)}} = ZAF \frac{I_i}{I_{(i)}} \tag{5.1}$$

where I_i and $I_{(i)}$ are the net x-ray intensities for each element i in the unknow, and standard sample, respectively and C_i and $C_{(i)}$ are the weight fractions for each element i in the unknow, and standard sample, correspondingly. Z is the atomic number correction factor, A is the absorption correction factor, and F is the fluorescence correction factor of X-Rays generated in the unknow sample for each element i.

Castaing [21, 22] has shown that the generated intensity (I_g) can be computed via Equation (5.2):

$$I_g = \int_0^\infty \varphi(\rho z) d(\rho z) \tag{5.2}$$

where $\varphi(\rho z)$ is the distribution of characteristic X-Ray production with depth z, and ρ is density of the material. However, with the absorption phenomenon, the emitted intensity, (I_e) , is given by

$$I_e = \int_0^\infty \varphi(\rho z) e^{-\frac{\mu}{\rho}(\rho z)csc\psi} d(\rho z)$$
 (5.3)

where, $\frac{\mu}{\rho}$ is the X-Ray mass absorption coefficient, $(\rho z)csc\psi$ is the absorption path length, and ψ is the take-off angle.

Philibert [23] has described the Z and A corrections as

$$Z = \frac{\int_0^\infty \varphi(\rho z) d(\rho z)_{std}}{\int_0^\infty \varphi(\rho z) d(\rho z)_{unk}}$$
 (5.4)

$$A = \frac{f(\chi)_{std}}{f(\chi)_{unb}} \tag{5.5}$$

$$f(\chi) = \frac{\int_0^\infty \varphi(\rho z) e^{-\frac{\mu}{\rho}(\rho z) csc\psi} d(\rho z)}{\int_0^\infty \varphi(\rho z) d(\rho z)}$$
 (5.6)

$$F = \frac{(1 + \sum_{j=1}^{m} f_{c,j} + f_{Br})_{(i)}}{(1 + \sum_{j=1}^{m} f_{c,j} + f_{Br})_{i}}$$
(5.7)

where *std* and *unk* refer to standard and unknown sample, respectively. For pure standard specimen, $f_{c,j}$ is null. For a multielement sample, $f_{c,j}$ and f_{Br} refer to the characteristic fluorescence and the bremsstrahlung fluorescence [24], respectively.

Quantitative microanalysis of a bulk sample using the conventional ZAF method is simple because existing models for $\varphi(\rho z)$ curves and absorption path are satisfactory for bulk *flat* samples [5]. Such models do not exist for particulates. Consequently, to apply the conventional ZAF model for particles, we propose to modify the original ZAF method by adding a geometrical correction factor, G.

Using the conventional ZAF method for a particle and a bulk sample with the same chemical composition, the G factor (to describe the geometrical effects) could be added to the ZAF method as

$$\frac{c_p}{c_b} = ZAFG \frac{l_p}{l_b} \tag{5.8}$$

where I_p and I_b are the net X-Ray intensities for each element i in the particle, and bulk sample, respectively, C_p and C_b are the weight fractions for each element i in the particle, and bulk sample, correspondingly. G is the geometrical correction factor, Z is the atomic number correction factor, A is the absorption correction factor, and F is the fluorescence correction factor of X-Rays emitted in the standard sample for each element i.

If the fluorescence correction is neglected, the ZA term can be obtained as

$$ZA = \frac{c_{bulk}I_{std}}{c_{std}I_{bulk}} \tag{5.9}$$

where std and bulk refer to standard and bulk sample, respectively. Note, the only difference between standard and bulk samples is the chemical composition (they are both bulk) (C_{bulk} , C_{std}).

Combining Equation (5.7) and Equation (5.8), with $C_p = C_b$, the G factor is described as

$$G = \frac{I_{bulk}}{I_p} \frac{1}{[ZA]} = \frac{I_{bulk}^2}{I_p I_{std}} \frac{C_{std}}{C_p}$$
 (5.10)

where I_p , I_{bulk} and I_{std} are the measured x-ray intensities for each element i in the particle, bulk, and standard samples, respectively. C_p and C_{std} are the weight fractions for each element i in particle, and standard sample, correspondingly. G is the geometrical correction factor, Z is the atomic number correction factor, and A is the absorption correction factor of x-rays generated in the standard sample for each element i.

5. 4. Materials and Method

To validate modeling data, the standard Energy Dispersive Spectroscopy (EDS) analysis was performed on the NIST - K411 (Ca = 0.112, Fe = 0.112, Mg = 0.092, O = 0.429, and Si= 0.256 in weight fraction %) standard particles (D = 0.5, 1, 2.5, 5, 10, 15, 25, 40 μ m) using a SU-3500 [High-Tech Canada, Rexdale, ON, Canada] at E₀ = 20 keV. Each standard EDS analysis was repeated 3 times for selected particle size. Pure elements were used as standard samples for Fe, Mg, and Si. Anorthite (CaAl₂Si₂O₈) was used as a standard sample for Ca and O. To maximize the accuracy of the experimental tests, they were done with a probe size significantly smaller than the particle size and with a long acquisition time (320 s). The average measured current was 220 pA. The beam size must be smaller than the particle size (D) and in the center of particles to avoid any X-Rays/electrons losses other than those resulting from the change of accelerating voltage. Another issue that needs to be addressed is beam drifting due to specimen charging. To overcome this problem, the acquisitions were done in the variable-pressure mode in the SEM-SU3500 (Hitachi-3500) equipped with EDS (Oxford).

5. 5. Results and discussion

Figure 5.3 shows the variation of the G factor for Ca-K α as a function of beam energy for NIST-K411 particles deposited on C substrate. As it can be seen, for a big particle (D \geq 10 μ m), the G factor is almost independent of the beam energy. Therefore, in the range of 3 to 30 keV, a particle of K411 with D \geq 10 μ m behaves like a bulk sample. As the particle size diminish below 1 μ m, transmission of electrons through the particle increases significantly, increasing the substrate (C) contribution to the X-Ray spectrum [5]. Therefore, increasing the beam energy for small particles

 $(D < 1 \ \mu m)$, decreases the intensity of the generated X-Rays for the particle dramatically, and thereby the G factor which is proportional to the intensity of particles (Eq. 5.10) decreases. The behavior of the curves in Figure 5.3, can be explained with Equation 5.10 and the interaction volume concept. Equation 5.10 shows that the G factor is proportional to the ratio of the generated X-Ray for the particle to the generated X-Ray of the bulk sample to the power of 2. For particles with intermediate size (D = 500 nm, 1 μm), the interaction volume is contained within the particle at low beam energies (3-5 keV). As a result, the G factor is close to 1 for a low beam energy (E₀ = 3 keV). To sum up, the G factor decreases below 1 as soon as the interaction volume is larger than the particle; therefore, based on the Equation 10, the behavior of G factor is justifiable. Moreover, results show that when particle size increases the G factor rises as well and it reaches its maximum (G = 1) at a specific particle size, depending on the beam energy. Plus, by increasing the particle size, its behavior gets closer to that of a bulk sample, and therefore the G factor is equal to one. More research on Figure 5.3 showed that the particle size corresponding to G = 1 for each beam energy is equal to the electron range [12] in a bulk sample with the same composition.

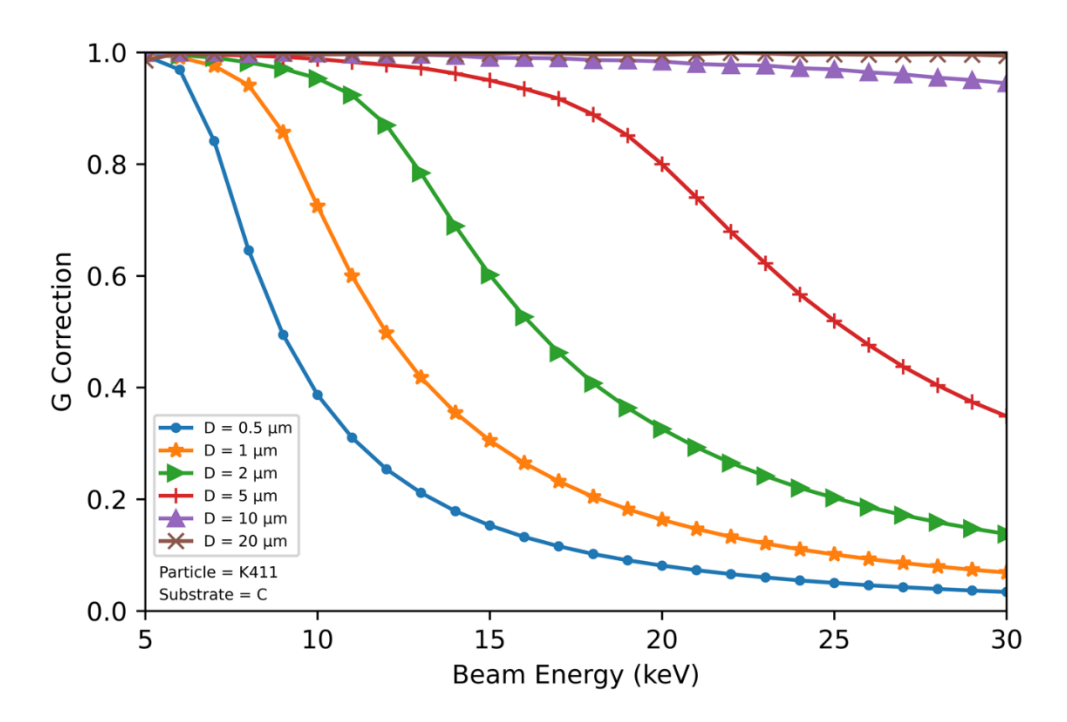


Figure 5-3 The G correction factor as a function of the beam energy for different particle size.

Figure 5.3 shows that the G factor depends on the beam energy and particles size. However, when the G factor is plotted as a function of $\frac{D}{X_e}$, where D is the particles size and X_e is the range of emitted x-rays in a bulk sample, the G factor shows a unique behavior (Figure 5.4).

 X_e can be obtained via Gauvin's universal Equation 5.11 [25].

$$X_e = \lambda \sin \psi \left(1 - e^{-\frac{X_g}{\lambda \sin \psi}} \right) \tag{5.11}$$

where ψ is the take-off angle, λ is the mean free path for the absorption with the Equation (5.11)

$$\lambda = \frac{1}{\rho_{Spec} \sum_{i=1}^{n} c_i \frac{\mu}{\rho}} \tag{5.12}$$

 c_i is the weight fraction of the n elements of the irradiated material, $\frac{\mu}{\rho}$ is the mass absorption coefficient of the characteristic X-ray line in element i and ρ_{Spec} is the mass density of the material, X_g is the X-Ray generation range as given by the Equation (5.13)

$$X_g = \frac{k}{\rho} (E_0^n - E_c^n) \tag{5.13}$$

where k and n are constants that depend on the atomic number of the irradiated material Z:

$$k = 43.04 + 1.5Z + 5.4 \times 10^{-3}Z^2$$
 (5.14)

$$n = 1.755 - 7.4 \times 10^{-3}Z + 3.0 \times 10^{-5}Z^2 \tag{5.15}$$

In Equation 5.13, E_0 is the incident electron energy, E_c is the critical ionization energy of the electronic subshell of the characteristic line.

The G factor as a function $\frac{D}{X_e}$ when the particle size, the beam energy, and the x-ray line were changed at the same time was plotted (Figure 5.4). The independence of the G factor from all parameters is shown in Figure 5.4.

Fitting data indicated that the behavior of the G factor as a function of $\frac{D}{X_e}$ can be given as:

$$G = 1 - e^{-\alpha \left(\frac{D}{X_e}\right)^{\beta}} \tag{5.16}$$

where D is the diameter of particle, X_e is the range of emitted x-rays in a bulk sample, the α and β are constant values. The α and β in Equation 5.16 were found as 66.75 and 1.6. Normalization of particle diameters (D) with emitted x-rays range (Xe) gives us the exact size of particles that contain the 95% of interaction volume. Consequently, when $\frac{D}{X_e} > 1$, the particle behaves almost as a bulk sample at specific beam energy. Having a unique behavior of the G factor while all parameters are changed shows the G factor does not rely on any specific parameters and it only depends on $\frac{D}{X_e}$ (Figure 5.4). Results show that using Equation 5.16 and modified ZAF model (ZAFG) makes it possible to easily obtain the chemical composition of particles by back-calculation of the Z and A, which will be shown in the following.

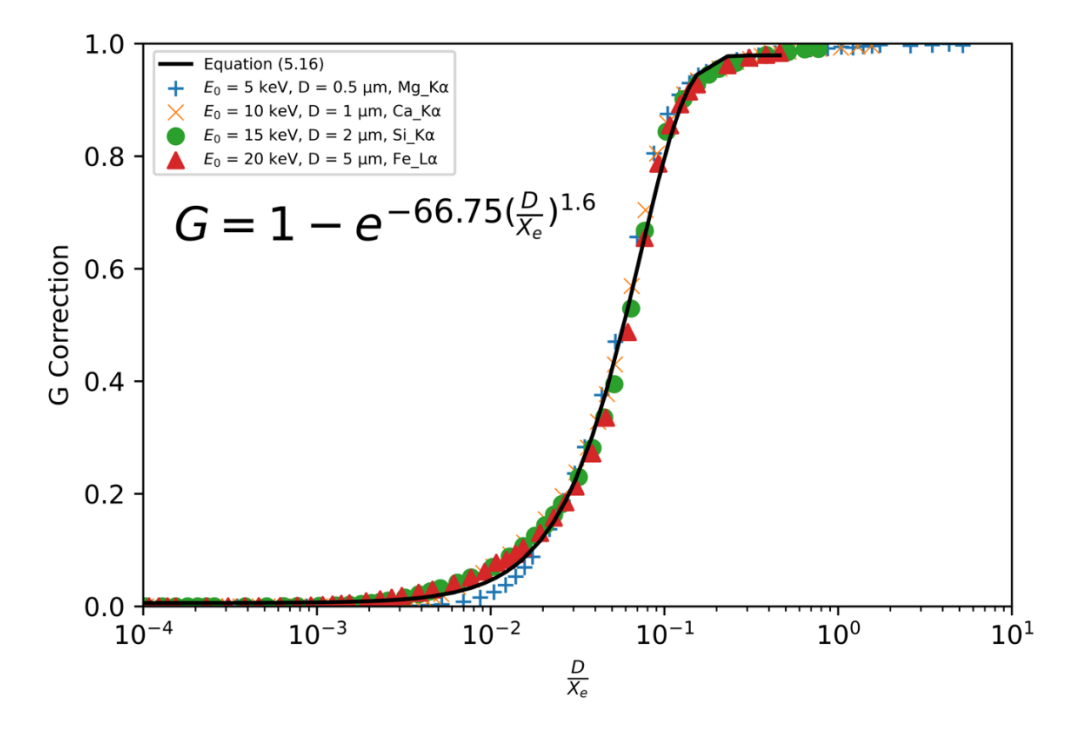


Figure 5-4 Variation of the G factor for all elements in NIST- K411 as a function of $\frac{D}{X_e}$.

Figure 5.5 shows the error distribution between the simulation points and the universal Equation 16 for the G factor when $\frac{D}{X_e}$ is changed. As it can be seen, the difference between the G factor obtained from simulation and the universal Equation 5.16 is less than 6 %. The maximum range of error (4 - 5.8 %) occurs when $0.02 < \frac{D}{X_e} < 0.06$. This error is for particle size (D) less than 250 nm. Therefore, it is recommended to use simulation data in this range if high accuracy is needed.

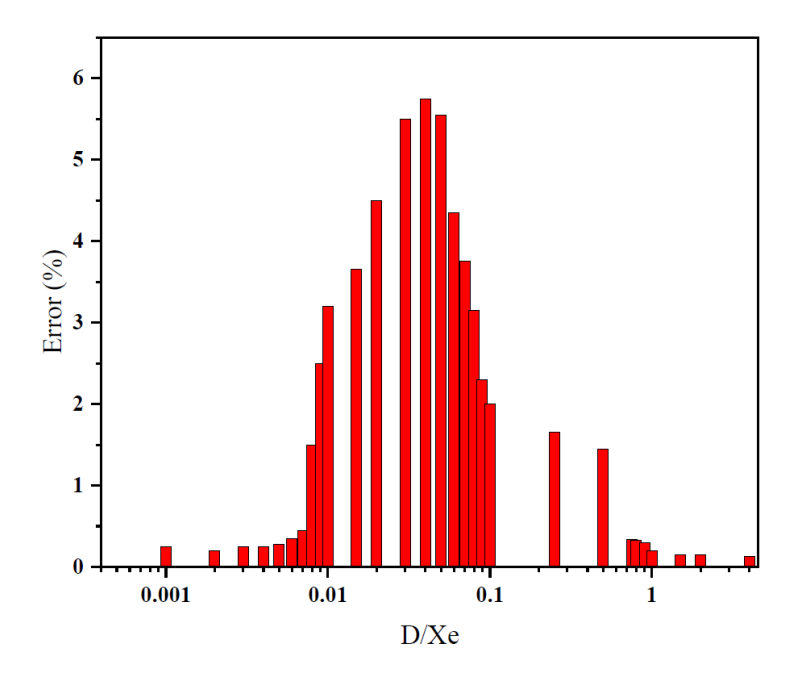


Figure 5-5 Error distribution of the G factor obtained from simulation and universal Equation 5.16 when $\frac{D}{X_p}$ is altered.

5. 5. 1 Validation of the ZAF(G) Model

To validate Equation 5.16, the standard EDS analysis was performed on the NIST- K411 standard particles. Figure 5.6 shows the flowchart of validation procedure. As a first step, an estimation of the chemical composition ($C_i^{Estimated}$) was done for each element (i) in several NIST- K411 particles. Then, using an SEM image, the size of each particle (D) was measured (Error < 5%). After that, X_e was calculated via the MC X-Ray for the bulk sample (Bulk NIST- K411). Following that, the G value was found by Equation 16. Using the following Equation 5.17, the intensity of the bulk sample (NIST- K411) is accessible:

$$I_i^b = \frac{I_i^p}{G} \tag{5.17}$$

Where I_i^b , I_i^p are the generated X-Ray intensities for each element i in particles and bulk sample (NIST- K411). Using the conventional ZAF method, Equation 1, a new $C_i^{Estimated}$ was obtained. These steps were repeated until it converges.

Table 5-1 lists the chemical composition of the NIST- K411 standard particles measured with the EDS standard quantitative analysis (conventional ZAF method-CalcZAF software) and the ZAFG

model (Equation 5.16). An excellent agreement is observed with data obtained from the ZAFG method. As the particle size decreases, the contribution of the substrate in X-Ray generation increases because small particles (D < 500 nm) lose a huge fraction of electrons due to the interaction volume concept. Therefore, emitted X-Rays do not represent X-Rays emitted from the particle itself.

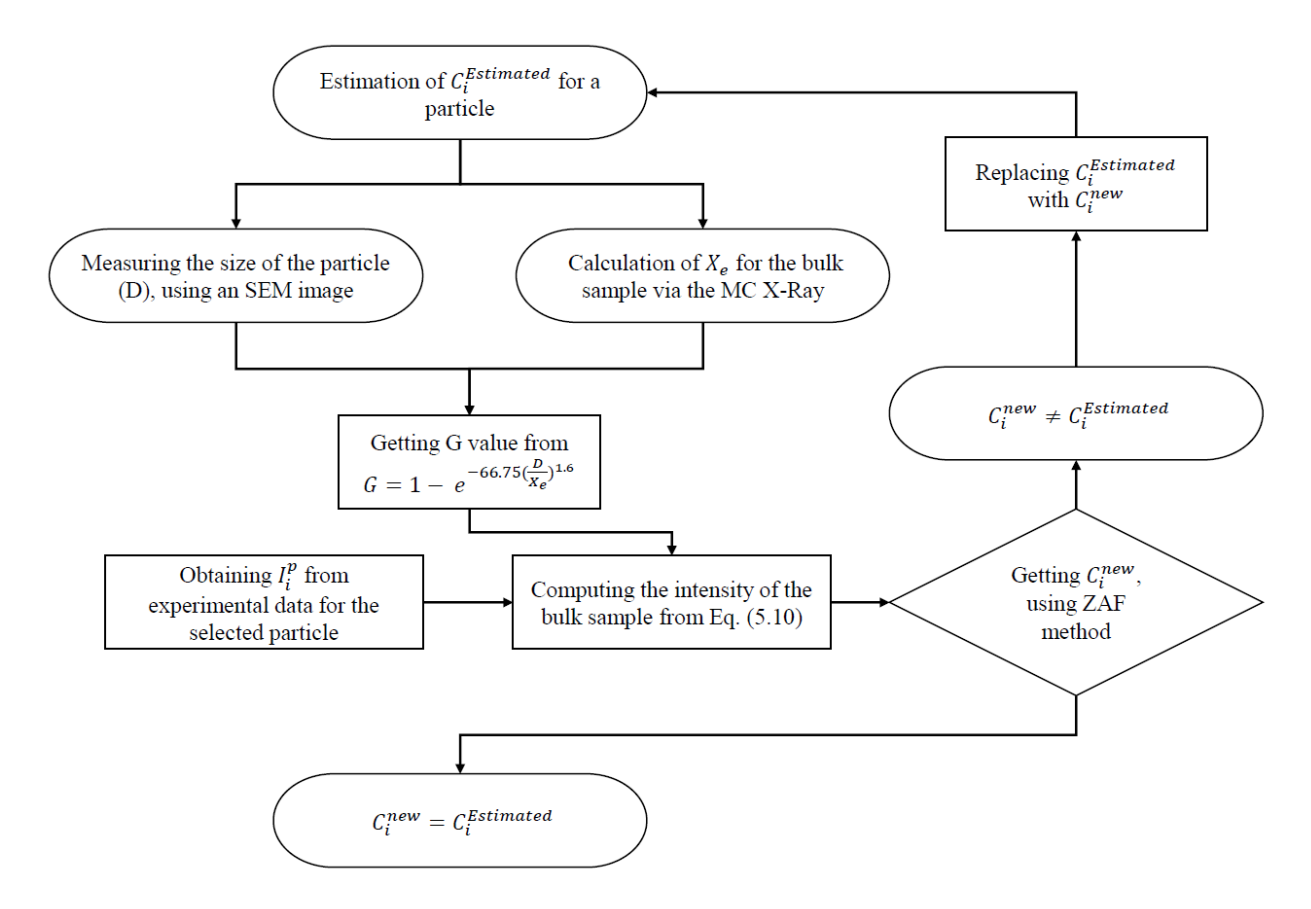


Figure 5-6 Flowchart for the validation of the universal equation (Equation 5.16).

Figure 5.7 indicates the error distribution of the measured composition vs the nominal composition and particle size. Figure 5.7a shows that the maximum error of the measured composition vs the nominal composition for individual elements is less than 1%. Although the maximum error of the sum weight fraction is 2.2% for a particle with $D = 0.5 \mu m$. However, for particles with $D > 1 \mu m$, the maximum error is 1.5%. Figure 5.7b indicates that as the particle size (D) increases, the error of the measured composition vs the nominal composition decreases. As it was already shown when $\frac{D}{X_e} > 1$, the G = 1, and thereby the particle works as a bulk sample. Therefore, reduction in error by increasing the particle size makes sense.

Table 5-1 Weight fractions of Ca, Mg, Fe, Si, and O in the NIST- K411 standard particles measured with EDS standard quantitative analysis, and the ZAF(G) method.

		Particle Size (D), μm							
		0.5	1	2.5	5	10	15	25	50
				Qua	antification	Method			
	NIST				ZA	F(G) Model			
	Certificate								
Elements		Weight Fraction (%)							
Ca	0.112	0.100	0.102	0.101	0.111	0.100	0.114	0.114	0.111
Fe	0.112	0.094	0.094	0.116	0.113	0.110	0.109	0.109	0.114
Mg	0.092	0.085	0.077	0.089	0.090	0.099	0.088	0.095	0.101
O	0.429	0.419	0.438	0.429	0.426	0.430	0.429	0.431	0.427
Si	0.256	0.262	0.260	0.249	0.250	0.255	0.254	0.249	0.251
Sum	1.001	0.960	0.971	0.984	0.990	0.994	0.994	0.998	1.004

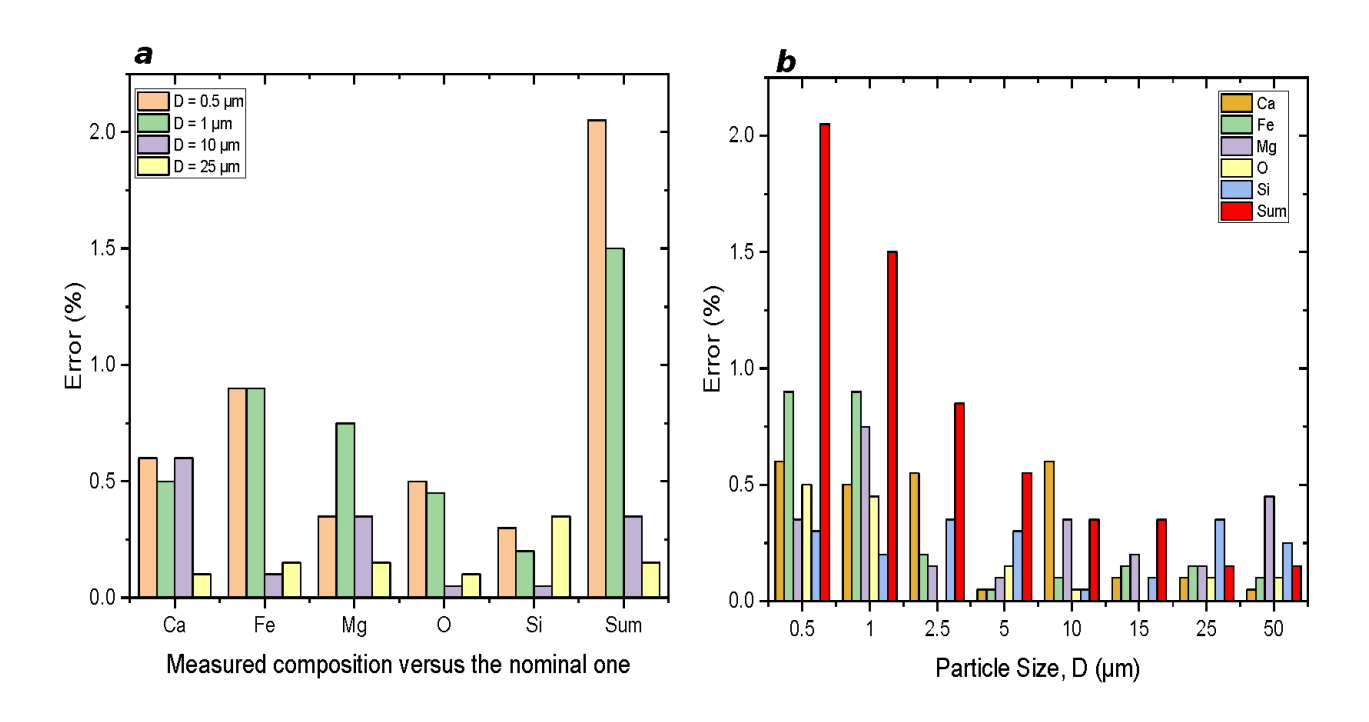


Figure 5-7 a) Error distribution of the measured composition vs the nominal composition, and b) Error distribution of the measured composition vs particle size.

5. 6. Conclusion

A universal equation to compute the geometrical correction factor (G) for quantitative microanalysis of particles has been derived. This equation is valid for homogeneous particles. Chemical composition computed using the universal equation agrees with data obtained from experimental work. It was shown that the G factor highly depends on $\frac{D}{X_e}$, where D is the particles size, and X_e is the range of emitted X-Rays in a bulk sample. Results showed that the G factor has unique behavior even if the beam energy, the X-Ray line, the particle size, and the chemical composition of particles are different. It was shown that when $\frac{D}{X_e} > 1$, G = 1, and thereby the particle x-ray emission behaves as a that of a bulk sample. In this situation, the conventional ZAF method can be used. Using the G factor will help to compute accurate quantitative X-Ray microanalysis for spherical particles but could be easily applied to different types of non-flat samples. In this case, the particular geometry will need to be accounted for the Monte-Carlo computation. By assuming that the G factor should not be changed by changing the composition, there is an opportunity to back-calculate the Z&A factors for different particle sizes and compare results with bulk specimens. In future work, the method will need to be validated on different types of shapes and with a larger batch of sample composition to evaluate the robustness of the method.

5. 7. Acknowledgment

Financial support from the Natural Science and Engineering Research Council of Canada (NSERC) and from the McGill MEDA Award is gratefully acknowledged.

5. 8. Declarations

Competing interests: The authors announce no competing interests.

5.9. Reference

- 1. Ngomsik, A.-F., et al., Magnetic nano- and microparticles for metal removal and environmental applications: a review. Comptes Rendus Chimie, 2005. 8(6): p. 963-970.
- 2. Statham, P.J. and J.B. Pawley, New method for particle x-ray micro-analysis based on peak to background measurements. 1978, United States: Scanning Electron Microscopy, Inc.
- 3. Newbury, D.E., Quantitative electron probe microanalysis of rough targets: testing the peak-to-local background method. Scanning, 2004. 26(3): p. 103-14.

- 4. Rez, P. and J. Konopka, Limitations in the use of the peak-to-background method for quantitative analysis. 1984. 13(1): p. 33-37.
- 5. Joseph I. Goldstein, D.E.N., Patrick Echlin, David C. Joy, A. D. Romig, Jr., Charles E. Lyman, Charles Fiori, Eric LHshin, Scanning Electron Microscopy and X-Ray Microanalysis. A Text for Biologists, Materials Scientists, and Geologists. 1992.
- 6. Armstrong, J.T. and P.R. Buseck, Quantitative chemical analysis of individual microparticles using the electron microprobe. Theoretical. Analytical Chemistry, 1975. 47(13): p. 2178-2192.
- 7. Small, J.A.H., K. F. J.; Newbury, D. E.; Myklebust, R. L., Progress in the Development of the Peak-to-Background Method for the Quantitative Analysis of Single Particles with the Electron Probe. Scanning Electron Microscopy, 1979. 2.
- 8. Gauvin, R., Quantitative X-ray microanalysis of heterogeneous materials using Monte Carlo simulations. Microchimica Acta, 2006. 155(1): p. 75-81.
- 9. Gauvin, R., P. Hovington, and D. Drouin, Quantification of spherical inclusions in the scanning electron microscope using Monte Carlo simulations. Scanning, 1995. 17(4): p. 202-219.
- 10. Gauvin, R. and E. Lifshin, Simulation of X-Ray Emission from Rough Surfaces. Microchimica Acta, 2000. 132(2): p. 201-204.
- 11. Gauvin, R. and E. Lifshin, X-ray microanalysis of real materials using Monte Carlo simulations. Microchimica Acta, 2004. 145(1): p. 41-47.
- 12. Reimer, L. Monte Carlo Simulation Techniques for Quantitative X-Ray Microanalysis. in Microbeam and Nanobeam Analysis. 1996. Vienna: Springer Vienna.
- 13. Ro, C.-U., et al., A Monte Carlo program for quantitative electron-induced X-ray analysis of individual particles. Analytical Chemistry, 2003. 75(4): p. 851-859.
- 14. Tylko, G., et al., Monte Carlo simulation for an assessment of standard validity and quantitative X-ray microanalysis in plants. IOP Conference Series: Materials Science and Engineering, 2010. 7: p. 012028.
- 15. Gauvin, R. and P. Michaud, MC X-Ray, a New Monte Carlo Program for Quantitative X-Ray Microanalysis of Real Materials. Microscopy and Microanalysis, 2009. 15(S2): p. 488-489.

- 16. Hovington, P., D. Drouin, and R. Gauvin, CASINO: A new monte carlo code in C language for electron beam interaction —part I: Description of the program. Scanning, 1997. 19(1): p. 1-14.
- 17. Alföldy, B., et al., Characterization of atmospheric particles by electron probe X-ray microanalysis. Scanning, 2002. 24(6): p. 297-300.
- 18. Huang, L. and L. Wang, Accelerated Monte Carlo simulations with restricted Boltzmann machines. Physical Review B, 2017. 95(3): p. 035105.
- Zhao, S. Advanced Monte Carlo Simulation and Machine Learning for Frequency Domain Optical Coherence Tomography. 2016.
- 20. Gauvin, R., et al., Win X-ray, the Monte Carlo program for X-ray microanalysis in the scanning electron microscope. Microscopy and Microanalysis, 2003. 9(S02): p. 32-33.
- 21. Castaing, R., Early Times of Electron Microprobe Analysis, in Electron Probe Quantitation, K.F.J. Heinrich and D.E. Newbury, Editors. 1991, Springer US: Boston, MA. p. 1-7.
- 22. Castaing, R., [Research under the electron microscope on precipitation in aluminum alloys]. C R Hebd Seances Acad Sci, 1949. 228(16): p. 1341-3.
- 23. Philibert, J., A Method for Calculating the Absorption Correction in Electron-Probe Microanalysis, in X-ray Optics and X-ray Microanalysis, H.H. Pattee, V.E. Cosslett, and A. EngstrÖM, Editors. 1963, Academic Press. p. 379-392.
- 24. Horny, P., et al., Development of a New Quantitative X-Ray Microanalysis Method for Electron Microscopy. Microscopy and Microanalysis, 2010. 16(6): p. 821-830.
- 25. Gauvin, R., A universal equation for the emission range of x rays from bulk specimens. Microsc Microanal, 2007. 13(5): p. 354-7.

Chapter 6. Using 3D Reconstruction Technique along with Monte Carlo Modelling for Quantitative Characterizations of Fracture Surface of Monel Alloy

In Chapter 5, the introduction of the universal equation for geometrical correction factor opened a new door for quantitative microanalysis of particles. Now we can focus on the quantitative microanalysis of real fracture surfaces. In this chapter, by integrating the MC X-Ray into Dragonfly software a new method was proposed to do microanalysis for real fracture surfaces. This chapter has been published as a short abstract in M&M 2022; however, we will provide more results in this chapter as a non-published report.

• This chapter has been published as a *short abstract*: S. M. Bayazid*, R. Gauvin, Using 3D Reconstruction Technique along with Monte Carlo Modelling for Quantitative Characterizations of Fracture Surface of Monel Alloy, Microscopy and Microanalysis 2022, (2022).

6. 1. Introduction

Quantitative microanalysis of non-flat surface is difficult in the scanning electron microscope. Although X-Ray microanalysis can be a useful tool for preliminary characterization, it is not quantitative because the complicated geometry of the non-flat surface introduces problems that are not present in the current models of quantitative microanalysis of a flat sample. The problem with the quantitative microanalysis of non-flat surfaces is that electrons can be scattered from all sides due to different slopes on the surface, so the generated x-rays depend on the non-flat. Moreover, the orientation of slopes makes it difficult to correctly consider the path of characteristic x-rays between their generation locations and the surface [1, 2] making difficult to compute an absorption correction. Therefore, the geometry of the non-flat surface impacts the measured x-ray intensities and thereby the quantitative analysis of the sample. We propose to measure the geometrical information of the non-flat surface in the electron microscope and to compute X-Ray detection from the measured non-flat surface with Monte Carlo simulation to overcome this problem.

In this work, we present preliminary results using a fracture surface of a Monel alloy (NiCu) (Give the exact composition). The 3D reconstruction of the non-flat surface was obtained using backscattered electron (BSE) images via the 4-Quadrant backscatter detector. The existing Monte Carlo software MC X-ray [3] was incorporated into the image processing software Dragonfly developed by Object Research Systems (ORS) Inc [4]. The incorporation of the MC X-ray in Dragonfly allows users to do Monte Carlo simulation for any complicated geometry.

6. 2. Materials and Method

BSE images (gathered via 4Q-BSE) were used for 3D reconstruction data via Mountains Map software. The Monte Carlo simulations were performed on the 3D fracture surface of Monel alloy using MC X-Ray as a plunge-in in Dragonfly. The beam diameter was equal to 10 nm and 10000 electrons were used to simulate electron trajectories in order to compute X-ray emission for the fracture surface. To compare simulation data with experimental data, the Energy Dispersive Spectroscopy (EDS) analysis was performed on the same fracture surface using a SU-3500 [High-Tech Canada, Rexdale, ON, Canada] at E0 = 20 keV. For comparison purposes, the net X-Ray intensity of the EDS maps was computed for experimental analysis and simulation data.

6.3. Results and discussion

Figure 6.1 and Figure 6.2 show BSE image and EDS map of Ni Kα and Cu Kα of the fracture surface (Monel alloy) acquired with the Hitachi SU-3500 Electron Microscope equipped with an Oxford X-MAX SDD EDS detector. As it can be seen, the fracture surface (for example the shadowing parts in the EDS maps for Ni and Cu) does not allow some X-Ray signals to reach the EDS detector, and this matter makes problems in quantitative characterization of fracture surfaces. Figure 6.3 and Figure 6.4 displays simulation data of the same surface used in Figures 6.1 and 6.2. There is an excellent qualitative agreement between experimental data and Monte Carlo simulation. As it can be seen, the EDS maps for simulations are even better than experimental data in terms of X-ray signals (compare Figure 6.2 with Figure 6.4).

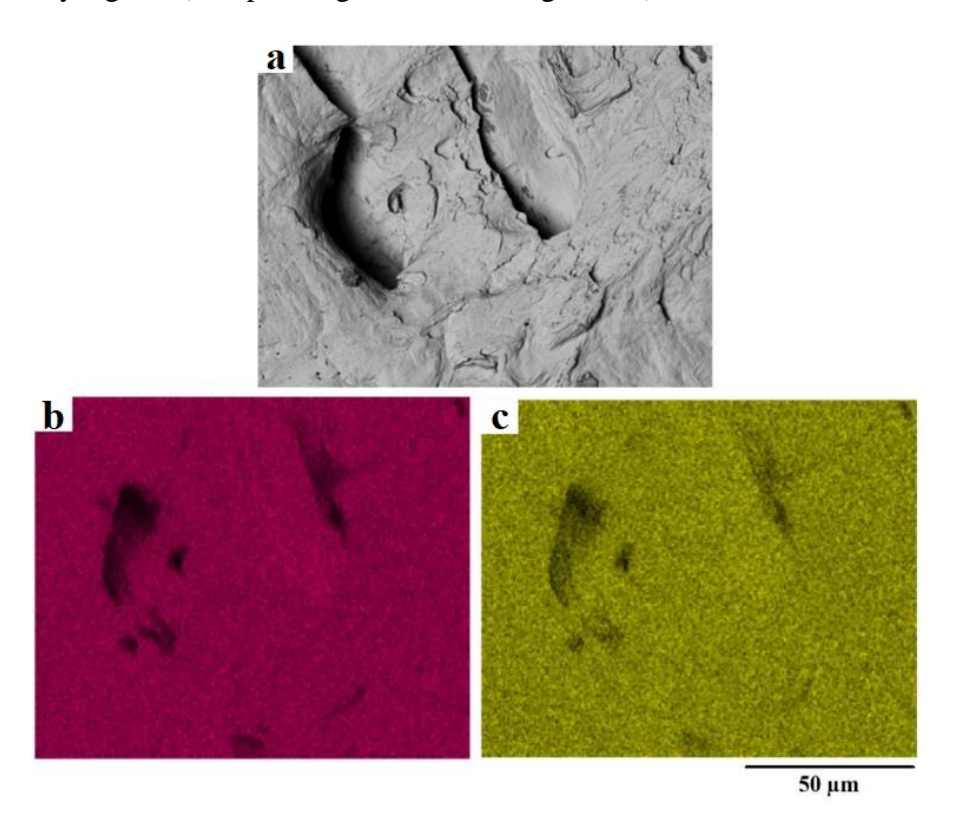


Figure 6-1 BSE images, and EDS maps for the fracture surface of Monel alloy, a) BSE, b) EDS map Ni K α , and c) EDS map Cu K α .

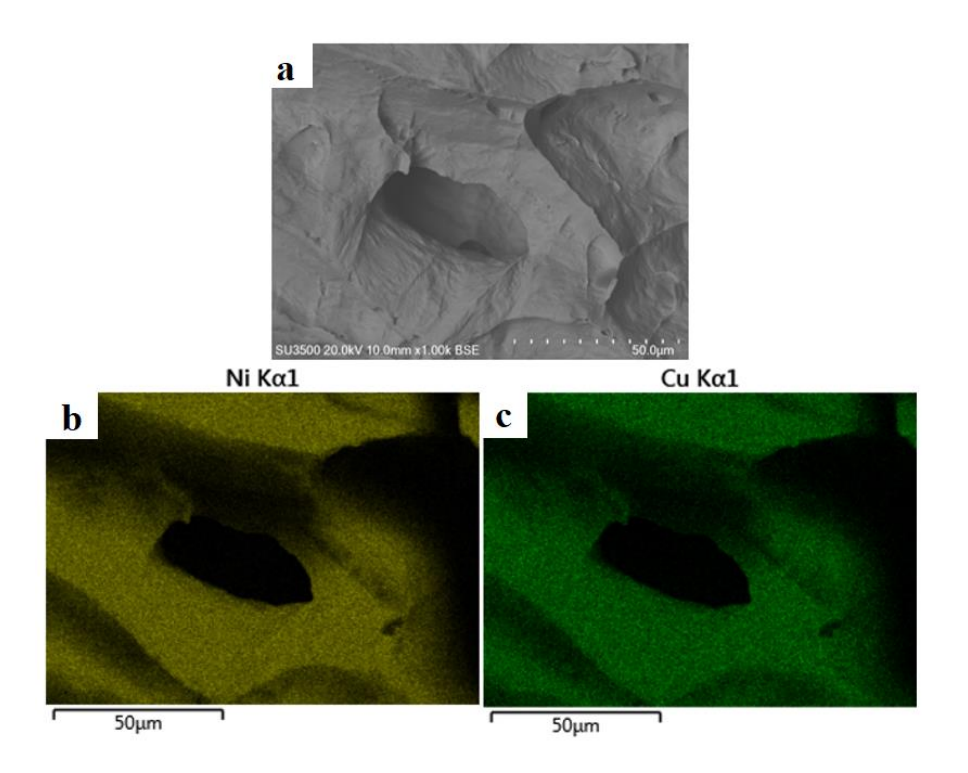


Figure 6-2 BSE images, and EDS maps for the fracture surface of Monel alloy, a) SE, b) EDS map Ni K α , and d) EDS map Cu K α .

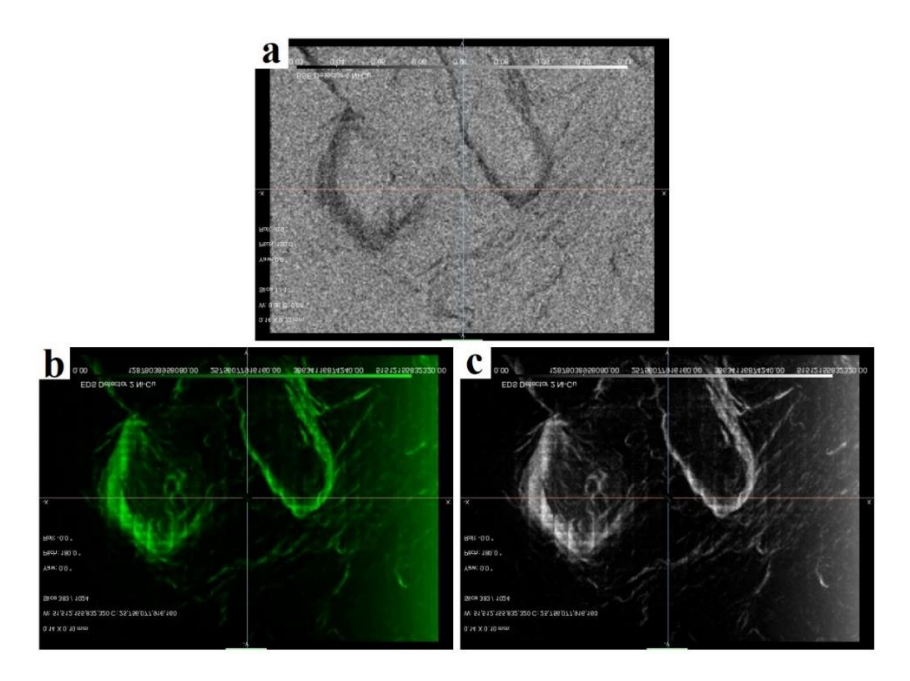


Figure 6-3 Simulation data for the same surface used in Figure 6-1, a) BSE image, b) EDS map Ni K α , and c) EDS map Cu K α .

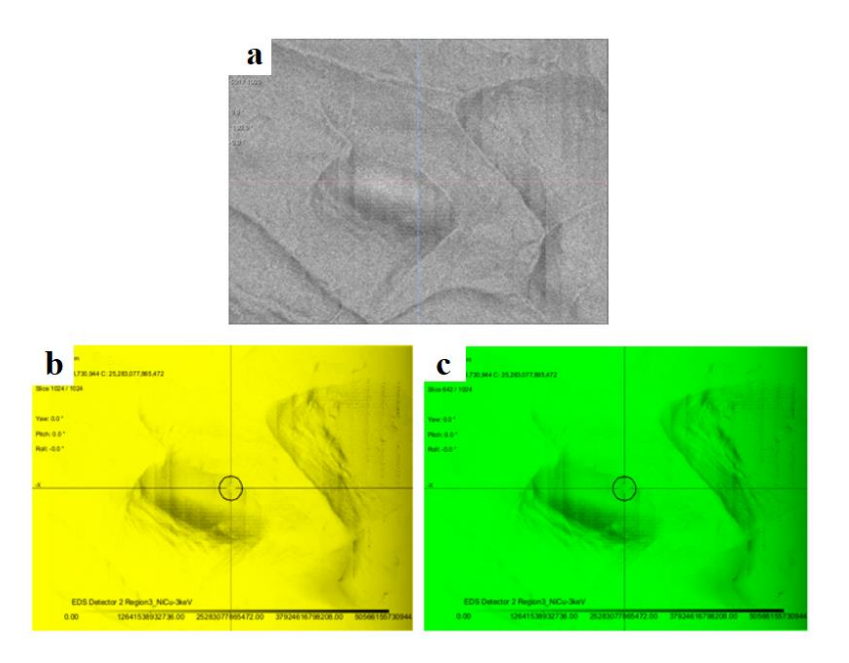


Figure 6-4 Simulation data for the same surface used in Figure 6-2, a) BSE image, b) EDS map Ni K α , and c) EDS map Cu K α .

Table 6-1 lists the ratio of net X-Ray intensity ($\frac{I_{fracture \, surface}}{I_{flat \, surface}}$) for Ni measured with experimental analysis and the Monte Carlo simulation separately. The net intensities were computed based on the sum EDS maps. Results showed that the ratio of net X-Ray intensity for experimental analysis ($\frac{I_{fracture \, surface-exp}}{I_{flat \, surface-exp}}$) and simulation ($\frac{I_{fracture \, surface-sim}}{I_{flat \, surface-sim}}$) were 0.409 and 0.419, respectively. A good agreement is observed with data obtained from the simulation. The amount of error that was observed was 2.21%.

Table 6-1 Comparison of the ratio of the net X-Ray intensity $(\frac{I_{\text{fracture surface}}}{I_{\text{flat surface}}})$ for experimental EDS map and Monte Carlo Simulation.

Net X-Ray Intensity Ratio				
$\frac{I_{\text{fracture surface}}}{I_{\text{flat surface}}}$				
0.409				
0.419				

Figure 6-5 shows an extra simulation of the fracture surface of Monel alloy via MC X-Ray and Dragonfly software. It shows the effect of beam energy on the EDS map. Using MC X-ray as one of the plunge-ins in Dragonfly gives us the opportunity to do multiple actions such as changing beam energy, tilt angle, take-off angle, and many other kinds of stuff that are either impossible in the SEM or take time and, for sure, cost to do that.

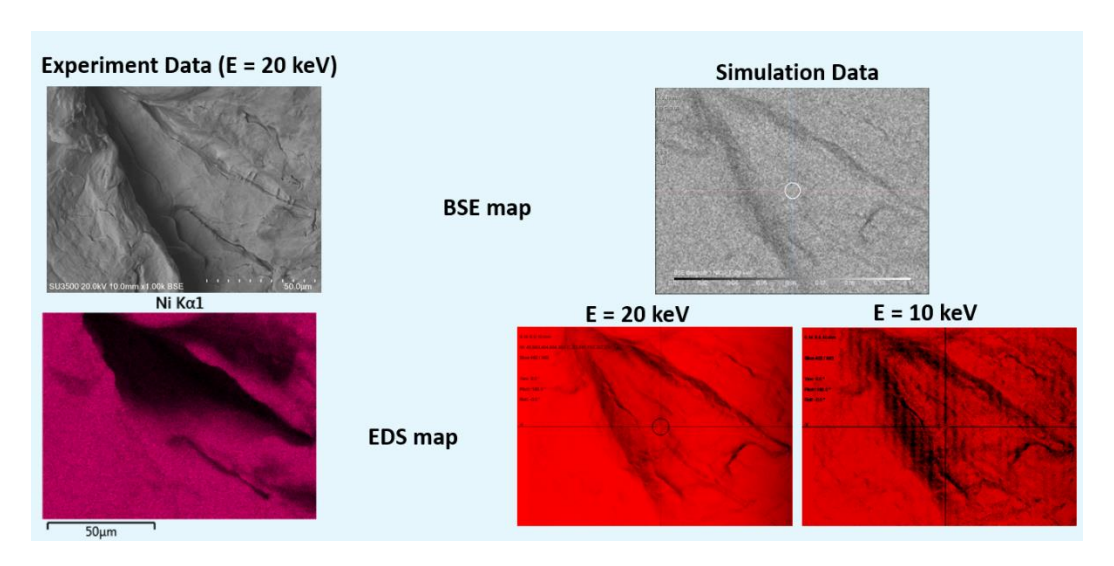


Figure 6-5 The effect of beam energy on EDS map, left-side) Experimental data at E = 20 keV, right-side) Simulation data for the same surface at E = 10 keV and E = 20 keV.

6. 4. References

- 1. Goldstein, J.I., et al., Scanning electron microscopy and X-ray microanalysis. 2017: Springer.
- 2. Statham, P. and J. Pawley, New method for particle X-ray Micro-analysis based on peak to background measurements, in Scanning electron microscopy/1978. Vol. I. 1978.
- 3. Gauvin, R. and P. Michaud, MC X-ray, a new Monte Carlo program for quantitative X-ray microanalysis of real materials. Microscopy and Microanalysis, 2009. 15(S2): p. 488-489.
- 4. Rudinsky, S., et al., libMCXray: A Monte Carlo Simulator for Signal Analysis inside Dragonfly Software. Microscopy Today, 2020. 28(5): p. 40-44.

Chapter 7. Concluding remarks

7. 1. Conclusion

The main purpose of this PhD study is to find a model for quantitative X-Ray microanalysis of non-flat surfaces via SEM. A 3D digital reconstruction technique was developed to convert 2D SEM images into a 3D solid in Chapter 3. The effect of SEM parameters on the P/B method were investigated in Chapter 4 to see the capability of this model for quantitative X-Ray microanalysis of non-flat surface. We introduced our new model (ZAFG) for quantitative X-Ray microanalysis of particle in Chapter 5; and finally, using 3D digital reconstruction data, we present preliminary results of our model for real fracture surface. The conclusions are summarized as follows:

- 1. The effect of SEM parameters such as Acceleration voltage, Magnification, and Working distance on the 3D digital reconstruction technique were studied. To observe the accuracy of the 3D digital reconstruction method, a standard sample was used. Both SE and BSE images were used as input of the model. SE images gives more topographical details than BSE signals; however, utilizing of SE image is very time consuming because the object in the SEM chamber needs a lot of rotation and tilting. However, the 3D digital reconstruction technique which utilize BSE can be done via single scan. It was observed that the working distance is a significant influential parameter in the digital 3D rebuilding method via SEM images. The best condition was obtained when the working distance was between 9 to 10 mm. It was found that by increasing the magnification to 1000X, the quality of 2D images which is important for 3D digital reconstruction, improved.
- 2. The efficiency of the P/B method as one of the candidates for microanalysis of non-flat surfaces then was investigated via MC X-Ray software. The P/B was evaluated while beam energy, tilt angle, take-off angle, and particle size were changing. Data showed the P/B highly depends on beam energy, the size of particles, and substrates. The dependency of the P/B to these parameters showed that the P/B is not constant, and it depends on geometry of particles. Therefore, it cannot be a good method for neither microanalysis of particle nor fracture surfaces.
- 3. Following the efficiency of the P/B method, a novel universal equation was introduced to compute the geometrical correction factor (G) for quantitative microanalysis of particles.

Results show that the G factor highly depends on $\frac{D}{X_e}$, where D is the particles size, and X_e is the range of emitted x-rays in a bulk sample. Chemical composition computed using the universal equation agrees with data obtained from experimental work. Using the G factor will assist us to do microanalysis for fracture surfaces. By having a G factor, there is an opportunity to back-calculate the Z&A factors from conventional ZAF method and then get chemical composition of non-flat surfaces.

4. Finally using the developed model, and the Monte Carlo software MC X-ray, which was incorporated into the image processing software Dragonfly, quantitative microanalysis of a real fracture surface was done. An excellent agreement was observed between experimental data and Monte Carlo simulation. Results showed our model could give us a highly valuable quantitative microanalysis for fracture surfaces.

7. 2. Contributions to original knowledge

Some contributions to original knowledge are intended to be offered with this PhD project:

- 1. For the first time, in this Ph.D. study, a quantitative method was developed to reconstruct 3D digital images of fracture surfaces using BSE images.
- 2. In this study, for the first time, the effect of SEM parameters such as Magnification, Accelerating Voltage, and Working Distance on the 3D digital rebuilding technique was investigated.
- 3. For the first time, this study introduced a geometrical correction factor for quantitative microanalysis of particles.
- 4. This study, will help us to describe fracture behaviors that create due to chemical composition problems.
- 5. Eventually, this is the first study that established a method for quantitative characterization of fracture surfaces via scanning electron microscopy.